AN X-RAY SURVEY OF THE SKY FROM BALLOON ALTITUDES

GÜNTER R. RIEGLER

JANUARY 1969

GSFC
GODDARD SPACE FLIGHT CENTER
GREENBELT, MARYLAND

AN X-RAY SURVEY OF THE SKY FROM BALLOON ALTITUDES*

by
Günter Rudolf Riegler

January 1969

Dissertation submitted to the Faculty of the Graduate School
of the University of Maryland in partial fulfillment
of the requirements for the degree of
Doctor of Philosophy
1969

*This research was supported by the National Aeronautics and Space Administration Grant NGL-21-002-033.

ABSTRACT

Title of Thesis: An X-Ray Survey of the Sky From Balloon Altitudes

Günter R. Riegler, Doctor of Philosophy, 1969

Thesis directed by: Frank B. McDonald, Visiting Professor

A series of balloon-borne X-ray experiments was carried out between December 1965 and July 1967. X-radiation in the energy band from 12 to 60 keV was detected with a combination of proportional and scintillation counters.

A clear relation between the background counting rate at a residual atmospheric depth of 3 g/cm^2 and the geomagnetic latitude was found. The secondary atmospheric X-ray background is assumed to be a component of atmospheric electromagnetic cascades which originate in the collisions of high-energy cosmic-ray particles with atmospheric nuclei; other X-ray production processes near the top of the atmosphere are shown to be insufficient to explain the observed secondary background. The correct prediction of the geomagnetic-latitude effect is shown to constitute a stringent test for models of atmospheric X-ray production.

Two observations of the Crab Nebula (Tau XR-1) resulted in net source spectra which can be described by a power-law photon spectrum with a spectral index of $n = 1.93 \, ^{+0.13}_{-0.09}$. A comparison with the results of measurements by other experimenters at lower and higher energies indicates that the X-ray spectrum of Tau XR-1 is a power-law of index $n \approx 2.0$ at energies between 2 and 400 keV.

A measurement of Tau XR-1 with good statistical accuracy was used to demonstrate two distinctly different methods of data analysis. Although the spectral parameters remained stable, the statistical uncertainty in the indices showed some dependence on the analysis method.

Three observations were made of the source Cyg XR-1, which has been reported by other observers to have variable intensity. The measurement with the highest statistical significance yields a spectrum similar to that obtained from Tau XR-1 and a flux level that is consistent with the results of an observation by another group of experimenters, conducted three weeks prior to the measurement reported here.

An experiment on 15 December 1966 showed that the spectrum of Sco X-1 between 15 and 35 keV is consistent with thin-source bremsstrahlung from a plasma at a temperature of approximately $5 \cdot 10^7$ °K. However, the photon flux at energies between 35 and 60 keV was found to be distinctly above the extrapolation of the lower-energy spectrum and was significantly higher than that observed a few months later by other groups. Similar high-energy deviations from a simple exponential spectrum have been observed by other experimental groups on two occasions. The existence of this high-energy feature and the variability of the X-ray spectrum are discussed in terms of two models for Sco X-1 which have been proposed recently.

An observation of the vicinity of the galactic center on 18 December 1966 detected a significant flux of hard X-radiation. Subsequent experiments by other groups have confirmed this finding, but to date a clear identification of the source or sources of this hard X-radiation has not been given.

Three observations of the vicinity of the north galactic pole brought contradictory results. An increase in the counting rate during the first experiment on 5 December 1965 was interpreted as the X-ray flux from a source in the direction of the Coma cluster of galaxies, which is near the direction of the north galactic pole. Subsequent observations failed to detect a similar feature and set upper limits to the photon flux from sources in the vicinity of the north galactic pole.

ACKNOWLEDGMENTS

I am grateful to the many people who have generously contributed to the success of this project. I am indebted most of all to Dr. Elihu Boldt for his guidance, assistance, and the many valuable discussions which took place during the course of my research. I also wish to express my deep gratitude to Dr. Frank B. McDonald who made my work at the High Energy Astrophysics Branch of the Goddard Space Flight Center possible and provided invaluable advice and encouragement during my graduate studies and in the course of the thesis research. The interest and encouragement displayed during the past years by Dr. Howard Laster, Chairman of the Department of Physics and Astronomy of the University of Maryland, is especially appreciated.

I further wish to acknowledge the interesting discussions with Dr. P. Serlemitsos and the valuable comments of Drs. T. Cline, S. Holt, D. Kniffen, J. Ormes, R. Ramaty, E. Roelof, B. Teegarden, and G. Simnet. It is a pleasure to thank Dr. V. K. Balasubrahmanyan for suggesting the comparison flight made from Texas. I wish to thank Drs. D. Fischel and T. Stecher for giving me access to their work prior to publication, for a computer program, and for their several interesting discussions and suggestions.

For engineering and technical support during all phases of the detector development and in the field, I am grateful to Messrs. D. Clark, F. Clese, H. Doong, R. Greer, J. Hodge, W. Nagel, M. Noordzy, M. Powers and A. Thompson. For their help in the data reduction and analysis I would like

to thank Mrs. G. Pearson and Messrs. P. Bracken, L. Foster, J. Kinsey, C. Kittel, and R. Silverberg.

For balloon flight support I am indebted to the Office of Naval Research and the Atomic Energy Commission as well as to the balloon launch team of the Air Force Cambridge Research Laboratory at the Holloman Air Force Base in New Mexico, the balloon launch team of the Australian Department of Supply in Mildura, Australia, and the Balloon launch team of the National Center for Atmospheric Research at Palestine, Texas. I also wish to acknowledge the financial support of this research through the National Aeronautics and Space Administration Grant NGL-21-002-033.

Most of all I am grateful to my wife, Sandra, who has given me so much help and moral support throughout my graduate studies.

TABLE OF CONTENTS

LIST OF TABLES

FIGURE CAPTIONS

Figure

Figure | Page

CHAPTER I

INTRODUCTION

Within the past 6 years, X-rays have become an important new tool for the astronomer. X- and gamma-radiation have extended the observed energy range of electromagnetic radiation from discrete celestial objects to encompass more than 12 orders of magnitude. Observations of the diffuse cosmic photon background have been carried out over a total energy interval of 15 orders of magnitude.

The experimental methods of X-ray astronomy are characteristic of both cosmic-ray measurements and optical and radio astronomy. On one hand, X-rays are treated like corpuscular particles which are counted and energy-analyzed; however, unlike charged particles, X-rays traverse magnetic fields without deflection so that the source position may be deduced from the direction of their arrival at the earth.

X-ray astronomy is expected to furnish new information for our understanding of high-energy processes in stellar atmospheres as well as in interstellar space. We will briefly review some processes which are involved in the production of photons in stellar atmospheres. The following mechanisms are of greatest interest:

(a) atomic and molecular processes

(b) Coulomb scattering

(c) interaction between a charged particle and the magnetic field

(d) collisions between photons and electrons

(e) nuclear reactions

(a) Atomic and molecular processes result in the absorption and emission of both lines and the continuum. Line spectra, which have been studied most thoroughly at optical wavelengths, are generated in stellar atmospheres and provide information on ion abundances, temperature, velocity, and the atmospheric pressure. For example, the observed optical lines may be members of the Balmer series for hydrogen and, similarly, of differing series for other atoms, molecules, and ions. Recent refinements in radio engineering techniques have made it possible to observe recombination lines from atomic levels with very high total quantum numbers, e.g., H 109α, H 158α, and He 158α. A hyperfine transition in the ground level of neutral hydrogen gives rise to the 21 cm line. Radio observations of this line allow the determination of the spin temperature and the integral number of neutral hydrogen atoms along the line of sight. Emission lines in the low-energy X-ray region of the spectrum are expected to be generated in hot plasmas at temperatures of more than 10^7°K. The most prominent X-ray lines from a Maxwellian gas with cosmic abundance distribution at a temperature of approximately 10^7°K are emitted at energies up to 7.15 keV (line emission of Fe^{+25}). However, detection of such lines in the X-ray spectrum has not been successful to date.

Edges in the continuum spectrum are caused by photoelectric absorption and by radiative recombination. They are produced in the source of electromagnetic radiation or in the medium between the source and the observer. The

emission spectrum of a Maxwellian gas of the type described above has recombination edges at energies up to 9.1 keV (the ionization energy of Fe^{+25}).

(b) Coulomb scattering of one charge in the field of another charge with accompanying emission or absorption of photons is called bremsstrahlung or free-free emission, respectively. Although the terms are sometimes interchanged, these processes are the inverse of each other and their cross-sections are related. Electron bremsstrahlung is an important emission mechanism for hot ionized gases. The shape of the spectrum depends on the optical depth, the temperature, the elemental abundance distribution, and the degree of ionization of the emitting plasma. Thermal bremsstrahlung emission has been detected from a variety of sources and over the full range of the observable photon spectrum, for example from interstellar HII regions at radio frequencies and from some sources of low-energy X-radiation. If the plasma is at a uniform temperature, then this temperature can be derived from the form of the observed spectrum. The amplitude can be related to the product of the electron and ion densities multiplied by the source volume.

The collision of a non-relativistic proton with a low-energy electron can also give rise to bremsstrahlung at X-ray energies. A simple transformation converts this process to the more familiar case of electron scattering in the field of a stationary proton. If the electron is initially bound, then one speaks of "internal bremsstrahlung."

(c) Interaction between a charged particle and the magnetic field. Magnetic bremsstrahlung is caused by the interaction of charged particles with

magnetic fields. At a given velocity, the emitted power is inversely proportional to the square of the mass of the particle so that emission by electrons is much more important than emission by protons.

Synchrotron radiation is generated by relativistic particles and is assumed to be the source of non-thermal optical and radio emission from the Crab Nebula. This hypothesis is supported by the detection of polarization which is a necessary feature of synchrotron radiation from ordered magnetic fields. Non-relativistic magnetic bremsstrahlung from electrons, called cyclotron radiation, has been observed at radio frequencies from Jupiter and the sun.

(d) Collisions between photons and electrons. Elastic collisions between photons and free electrons are called Compton collisions. When an energetic electron transfers some of its energy to a photon, then one speaks of the "inverse Compton effect."

The single observation that is perhaps most intimately correlated with the study of galactic and extragalactic cosmic rays is an observation of the diffuse cosmic X- and gamma-ray background. Recent measurements have indicated that this background is approximately isotropic. It has been suggested (Hoyle, 1965; Gould, 1965a; Felten and Morrison, 1966a) that this diffuse X-ray flux is generated by inverse Compton scattering of electrons by the universal 3 °K black-body spectrum. If the Compton effect is assumed to dominate, the appropriate part of the electron spectrum can be deduced from the spectra of the low- and high-energy photon distributions. However, the real situation is considerably more complicated because other energy loss mechanisms influence the equilibrium electron spectrum. Felten and Morrison (1966a) have proposed

the existence of an extragalactic electron component in addition to the more intense galactic component. At present there is no consistent theoretical model which also agrees with the results of measurements on high-energy electrons.

(e) Nuclear reactions generate gamma radiation either directly, or indirectly through positron and neutron formation. Among the more important reactions that produce line emission are the neutron capture by H^1, deuteron production in proton-proton collisions with subsequent pair annihilation, and tritium production. Of course, the positron in the pair-annihilation reaction above can also be supplied by many other reactions.

Proton-proton collisions produce high-energy gamma rays via pair annihilation or π^o-decay. The subsequent electromagnetic cascade involves pair-production and -annihilation, bremsstrahlung, and Compton scattering and will produce a substantial flux of lower-energy gamma radiation.

The r-process of nuclear synthesis (Burbidge et al., 1957) produces several heavy radioactive isotopes. The lowest-energy emission line with high intensity is generated at 60 keV by Am-241 (Jacobson, 1968). Decay via internal conversion gives rise to the emission of characteristic K-shell radiation from various heavy isotopes at energies between 100 and 130 keV.

It is apparent that the observation of high-energy photons provides valuable information about the astrophysical processes and the energy balance in the source. For example, the total luminosity in the X-ray region is larger than that in the optical region by a factor of about 3 for a power-law energy spectrum of index 1. A spectrum of this form is assumed to [illegible]rn the optical

and X-ray emission of the Crab Nebula. On the other hand, a thin-source thermal spectrum at a temperature of $5 \cdot 10^7$ °K can explain some of the observations of Sco X-1 (see Chodil et al., 1968). In this case the luminosity ratio becomes approximately 10^2.

The attenuation length in air for photons of 30 keV energy is 3 g/cm^2, which makes it necessary to conduct measurements of cosmic X-radiation near the top of the atmosphere. At 3 keV the attenuation length is reduced to 0.005 g/cm^2 so that cosmic X-rays of this energy cannot be measured at balloon altitudes. The first evidence for the arrival of X-radiation from beyond the solar system was obtained in June 1962 (Giacconi et al., 1962), with a set of rocket-borne uncollimated Geiger counters which were sensitive to X-rays from 2 to 8 A. The experimental objective was the detection of fluorescence radiation produced on the surface of the moon by solar X-radiation; instead, radiation from a direction near the galactic center was observed. The existence of this source in the constellation Scorpius was later verified (Gursky et al., 1963; Bowyer et al., 1964a). In addition, these later flight records indicated the arrival of X-rays from the constellations Cygnus and Taurus.

In July 1964 a rocket measurement was performed at the moment when the moon occulted the central region of the Crab Nebula (Bowyer et al., 1964b). This experiment demonstrated that the Crab Nebula was the source of the X-radiation from Taurus. The angular width of the X-ray source was determined to be about 1 minute of arc. The finite angular extent provided a strong argument against the neutron-star hypothesis for the source Tau XR-1. Another

result of these rocket experiments was the evidence for the existence of a diffuse cosmic X-ray background. This cosmic background flux is roughly isotropic (Grader et al., 1966), and has been measured at energies up to approximately 1 MeV (Metzger et al., 1964).

The first X-ray astronomy experiments used small-area detectors with poor angular resolution. In subsequent observations the effective detector area was increased and the angular resolution and rocket pointing accuracy were improved. It became possible to resolve the X-radiation from the constellations Cygnus, Sagittarius, and Scorpius into discrete X-ray sources. Early in 1967, a list of 30 cosmic X-ray sources was published by Friedman et al. (1967b), but the typical uncertainty in the source position was still of the order of a few degrees. Independent surveys by other groups (Gursky et al., 1967; Fisher et al., 1968; Bradt et al., 1968a) showed only partial agreement with the source locations given by Friedman et al. (1967b). At present 22 cosmic X-ray sources (Webber, 1968) have been confirmed by various rocket experiments.

Very few of these 22 sources of X-radiation have been identified with celestial objects. Almost 2 years after the identification of Tau XR-1, an ingenious collimator made it possible to measure the location of Sco X-1 to within 30 seconds of arc (Gursky et al., 1966). The search for the corresponding optical object was guided by an extrapolation of the observed X-ray spectrum into the optical region. Sco X-1 was then identified with a flickering blue object of magnitude V = 12.6 (Sandage et al., 1966). Similar methods were applied to

sources in the constellation Cygnus. The X-ray source Cyg X-2 was tentatively identified with a starlike object (Giacconi et al., 1967b), which was later shown to be a binary system (Kraft and Demoulin, 1967). Cyg XR-1 could not be identified with an optical object because of the heavy obscuration in the direction of that particular region of the galaxy (Giacconi et al., 1967b).

Low-energy X-ray measurements from rockets are restricted by the absorption of X-radiation in interstellar hydrogen. The lower energy limit for rocket observations of nearby galactic X-ray sources is at approximately 0.2 keV. The upper limit is imposed by the short exposure time in rocket experiments since the statistical significance of the observed high-energy photon flux is reduced for a steep photon spectrum. Consequently, measurements from rockets are usually carried out in the energy interval from approximately 1 to 20 keV.

The attenuation of X-radiation in air restricts experiments at balloon altitudes to energies above approximately 15 keV. In addition to the attenuated cosmic diffuse background, there is a diffuse background of atmospheric X-radiation at all altitudes. This background and the attenuation of X-radiation in the residual atmosphere limit the photon flux from cosmic sources that can be measured at a given altitude. Practical detectors also have a certain counting-rate background that is internally generated and further restricts the smallest photon flux that can be measured with a given field of view. The great advantage of balloon observations lies in the possibility of long exposure times to cosmic X-ray sources. Exposure times of a few hours are feasible, in contrast to rocket experiments which have durations of a few minutes.

Balloon observations of cosmic X-ray sources began in 1964, 2 years after the first rocket measurements. Clark (1965) observed X-radiation from Tau XR-1 up to energies of 62 keV. This result furnished new evidence against the hypothesis that X-radiation from the Crab Nebula is produced by black-body emission from the surface of a neutron star. Subsequent experiments from balloon altitudes, for example by Peterson et al. (1968), resulted in refined measurements of the emission spectra of Tau XR-1 and of other X-ray sources. Long exposure times made it possible to extend the observed spectrum up to energies of a few hundred keV. Together with the results of rocket measurements, the X-ray spectrum for certain sources has been determined over more than two decades in energy.

The present series of experiments sought to study cosmic X-radiation at balloon altitudes. Detectors were designed for photon measurements at energies between 10 and approximately 100 keV. The two-fold purpose of the survey was to find sources of hard X-radiation and to measure their spectra. This aim dictated the choice of the angular resolution and the number of channels for the pulse-height analysis.

Various sectors of the northern and southern sky were scanned in a series of balloon flights. Some regions were selected because they were already known to contain sources of hard X-radiation. The vicinity of the galactic center was studied because the detection of soft X-rays from several sources suggested that a flux of high-energy radiation might be observable. In the absence of discrete sources, anisotrophy of the diffuse radiation in the direction of the galactic center seemed to be physically possible.

Some of the more prominent production mechanisms for X-radiation will be reviewed in the following chapter. Chapter 3, "Detectors," contains a description of the proportional and scintillation detectors as well as the properties of the shield and the methods of data handling. In chapter IV, "Summary of Experiments," we discuss relevant information for all balloon experiments and the detector orientation systems which were used in the observations. The numerical and statistical handling of the data is described in the chapter on the "Methods of Data Analysis." The chapter entitled "Results" contains details of the various X-ray source observations, the results of the final data analysis and a discussion of each source or source region.

A review of topics related to the production of X-radiation at balloon altitudes is given in appendix B.

CHAPTER II

X-RAY PRODUCTION MECHANISMS

Several reviews of cosmic X-ray production mechanisms have been written (Morrison, 1958; Hayakawa et al., 1964a; Hayakawa and Matsuoka, 1964b; Ginzburg and Syrovatskii, 1965; Oda, 1965; Hayakawa et al., 1966; Gould and Burbidge, 1967b; and Gould, 1967a). The basic processes are well understood and can be grouped into two classes: electron-photon processes (synchrotron radiation, bremsstrahlung, and Compton scattering) and nuclear and atomic processes (gamma-ray line emission by radioactive or fissionable isotopes produced in r-process synthesis, internal conversion radiation from excited nuclei following radioactive decay, atomic recombination lines, etc.).

Line emission will not be discussed here because the energy resolution of the present series of experiments is insufficient to detect any of the lines that might be expected. Also, we do not expect emission lines of high intensity within the energy region that we are considering (sections III B and III C). For example, lines from hot plasmas with universal abundance occur at energies below 10 keV (Tucker, 1967). The most important lines from the decay of radioactive isotopes which were synthesized in the r-process have photon energies above 60 keV (Jacobson, 1968).

The identification of a source spectrum as an exponential or power-law function of energy does not unambiguously define the source mechanism. Just as in the case of the optical continuum spectra, which are not well described by a

simple black-body function but, rather, by solutions of the radiative transfer equation, an interpretation of X-ray spectra is not straightforward. Sartori and Morrison (1967a) have proposed a model where a non-thermal radio source emits thermal bremsstrahlung from plasmas at two different temperatures. Klimas (1968, private communication) has studied the emission spectra of plasmas with given distributions of temperature and electron density. The type of spectrum emitted from such sources was found to depend strongly on the spatial distribution of temperature and density. Manley (1966) has shown that the synchrotron emission spectrum of electrons with a flat energy distribution is nearly exponential.

With these considerations in mind, we will proceed to review the basic X-ray production mechanisms.

A. Synchrotron Radiation

The synchrotron process appears to be the principal mechanism for photon production in some radio sources. For example, the polarization of the radio and optical radiation from the Crab Nebula can best be explained as due to the synchrotron mechanism. An electron of energy $E_e = \gamma m c^2$, moving in a magnetic field H emits a synchrotron emission spectrum which has a maximum at

$$E_m = 1.16 \cdot 10^{-8} H_\perp \gamma^2 = 4.47 \cdot 10^{-20} H_\perp E_e^2 \quad , \qquad (1)$$

where the electron and photon energies are measured in eV, H is measured in Gauss, and $H_\perp = H \cos\theta$ is the strength of the magnetic field perpendicular to the electron orbit (Hayakawa et al., 1964a).

The synchrotron spectrum is usually approximated by a delta function spectrum at E_m. The power radiated by an electron of energy E_e is

$$P(E, E_e) = 0.98 \cdot 10^{-3} H_\perp^2 (E_e / mc^2)^2 \delta(E - E_m) , \quad (2)$$

where P is in units of eV/sec. If the electron spectrum can be described by a power-law of the form

$$N(E_e)\, dE_e = K E_e^{-\Gamma} \, dE_e , \quad (3)$$

then the observed synchrotron spectrum in the case of a homogeneous magnetic field becomes

$$I_s(E) = \frac{1}{4\pi} \iint P(E, E_e)\, N(E_e)\, dE_e\, d\Omega = A \cdot K_1(\Gamma)\, E^{-\frac{\Gamma-1}{2}} H_\perp^{\frac{\Gamma+1}{2}} , \quad (4)$$

where A is a constant and K_1 is a function of the spectral index Γ. The emitted photon spectrum is a power-law in energy with an index that is related to the index of the electron spectrum.

In the presence of a random magnetic field, equation 4 is still applicable, provided $K_1(\Gamma)$ is replaced by a slightly different function of Γ, and $H_\perp$ is replaced by $|H|$ (Ginzburg and Syrovatskii, 1964).

For an electron which loses its energy E only by the synchrotron process, we can define a lifetime T such that the rate of energy loss is equal to E/T. The lifetime is then equal to

$$T = 0.513 \cdot 10^{9} \frac{mc^2}{E_e H_\perp^2} \text{ (sec)} \quad (5)$$

(Hayakawa et al., 1964a). For example, an electron of energy $E_e = 2.7 \cdot 10^{13}$ eV will originally produce radiation at $E_m = 30$ keV in a field of $H_\perp = 3 \cdot 10^{-4}$ Gauss. Such an electron has a lifetime of 10^8 sec $\approx$ 3 years.

A magnetic field of the order of 10^{-4} Gauss is assumed to be present in the Crab Nebula. If high-energy electrons have been generated in the original supernova explosion with a spectrum which produces the observed radio emission, then they cannot generate the measured X-ray spectrum because of the high rate of synchrotron loss (Tucker, 1967). If the X-ray flux is produced by synchrotron emission, then it must be assumed that continuous production of high-energy electrons takes place in the Crab Nebula. The detection of polarization of X-ray emission would support the synchrotron hypothesis.

B. Inverse Compton Scattering

We consider an electron of total energy $E_e = \gamma m c^2$, in the rest frame S of the observer (Felten and Morrison, 1966a). The electron collides with a photon of energy E which is incident at an angle α. It is easiest to perform the calculations in the rest frame S' of the electron, where the outgoing photon angle is α' and the electron scattering angle is θ'. In this rest frame the interaction is just the standard Compton scattering. After transformation back to the frame S, one obtains the energy E_1 of the scattered photon (Felten and Morrison, 1966a)

$$E_1 = \frac{\gamma^2 E (1 + \beta \cos \alpha) (1 - \beta \cos \alpha')}{1 + (\gamma E/mc^2) (1 + \beta \cos \alpha) (1 - \cos \theta')} \quad (6)$$

As long as the photon energy is small, $\gamma E \ll m c^2$, in the rest frame of the electron, equation 6 can be approximated by

$$E_1 \approx \gamma^2 E \quad . \quad (7)$$

In this case classical Thomson scattering prevails in the electron rest frame.

The power scattered by one electron moving through a photon distribution of energy density ρ (in eV/cm^3) is

$$P_c(\gamma, \rho) = E_1 \frac{\sigma_{Thomson}\, c\rho}{E} = 2.10^{-14}\, \gamma^2 \rho \ , \tag{8}$$

where P_c is measured in eV/sec. For an isotropic distribution of photons, equation 8 can be integrated over all angles; this results in an additional factor of 4/3 for the scattered power.

As in the discussion of synchrotron radiation, it is customary to approximate the spectral power $dP_c/dE\ (E,\ \gamma,\ \rho)$ by a delta function at a characteristi energy E_c

$$\frac{dP_c}{dE}(E,\ \gamma,\ \rho) \approx P_c(\gamma, \rho)\ \ \delta(E-E_c) \ . \tag{9}$$

The average energy of a black-body distribution of photons is

$$\langle E \rangle = \alpha\, K\, T \ , \tag{10}$$

where $\alpha \approx 2.7$. The characteristic energy of the emitted photons becomes

$$E_c \approx \frac{4}{3}\gamma^2\, \alpha\, kT \tag{11}$$

(Ginzburg and Syrovatskii, 1964). With a power-law energy spectrum for the electron,

$$N(E_e)\, dE_e = K_o\, E_e^{-\Gamma}\, dE_e \ , \tag{12}$$

we obtain the power scattered per unit energy in the electron source volume in the presence of an ambient black-body distribution of photons at temperature T:

$$I_c(E) = \int_o^\infty \frac{dP}{dE}(E,\ E_e,\ \rho)\ N(E_e)\, dE_e = \frac{P_c(\gamma_E,\ \rho)\ N(E_E)}{2 \cdot \frac{4}{3} \cdot \gamma_E\, \alpha\, kT} \ , \tag{13}$$

where γ_E is given by (equation 11)

$$\gamma_E = \sqrt{\frac{3}{4}\ \frac{E_c}{\alpha kT}} \tag{14}$$

We finally have a power-law photon spectrum with the same index as the synchrotron spectrum

$$I_c(E) = 10^{-4}\,\rho N_o \left(\frac{3}{4a}\right)^{\frac{3-\Gamma}{2}} T^{\frac{\Gamma-3}{2}} E^{-\frac{\Gamma+1}{2}} \qquad (15)$$

The Compton-synchrotron process. A magnetic field and high-energy electrons in the presence of photons having, for example, a black-body distribution, give rise to both inverse Compton and synchrotron emission. The peak in the synchrotron photon spectrum, E_m is related to that of the Compton-process photon spectrum, E_c. When equations 1 and 11 are solved for γ, we obtain

$$E_c = 1.15 \cdot 10^{8}\,\alpha\,\frac{kT}{H}\,E_m\ , \qquad (16)$$

where E_c, E_m, and kT are measured in units of eV, H is in Gauss, and $\alpha = 2.7$. For most astrophysical applications, the ratio E_c/E_m is very large compared to one. If a power-law spectrum of electrons is assumed as before (equation 3) then the ratio of the emitted intensities for the synchrotron and Compton processes is

$$\frac{I_s}{I_c} \approx \frac{3}{2}\,\frac{H^2}{8\pi\rho}\left(\frac{1.8 \cdot 10^{4}\,T}{H}\right)^{\frac{3-\Gamma}{2}}\ , \qquad (17)$$

where ρ is again the photon energy density, T is in °K, and H is in Gauss.

Felten and Morrison (1963) have suggested that a power-law energy distribution of electrons in the galactic halo produces both the synchrotron-radiation background observed at radio wavelengths and the X- and gamma-ray background via the Compton process. However, detailed calculations (Felten and Morrison, 1966a) show that the predicted Compton spectrum in the presence

of a cosmic 3 °K black-body distribution of photons (Dicke et al., 1965; Penzias and Wilson, 1966) falls short of explaining the observed cosmic X-ray background spectrum by about two orders of magnitude. The spectral shape of the predicted X-radiation background is compatible with the observed one. An extragalactic electron component would be required to match the observed X- and gamma-ray spectrum.

Similar models have been forwarded for discrete sources. Gould (1965b) attempted to explain the Crab Nebula X-radiation by a Compton spectrum caused by the electron distribution that produced the observed radio spectrum via the synchrotron process. A discrepancy of approximately five orders of magnitude between the observed and the calculated X-ray intensities was obtained.

C. Bremsstrahlung

We assume that electrons of density n_e have a Maxwellian energy distribution around an energy kT and interact with ions of charge Z and density n_i. The equation for the bremsstrahlung spectrum as given by Allen (1963) can be modified to give the number of photons emitted per unit time, volume, and frequency:

$$\frac{dN}{d\nu} = 4\pi \frac{16}{3}\sqrt{\frac{\pi}{6}}\frac{e^6 Z^2}{c^3 m}\sqrt{\frac{m}{kT}}\, n_e n_i\, g(h\nu,\ kT)\ \exp\left(\frac{-h\nu}{kT}\right)\frac{1}{h\nu}\quad , \tag{18}$$

where $dN/d\nu$ is measured in units of photons/cm^3-sec-Hz, and the Gaunt factor $g(h\nu,\ kT)$ will be defined below. In an exact treatment one must fold a Maxwellian electron distribution with the bremsstrahlung formula in the

nonrelativistic Born approximation including the Sommerfeld factor. The Sommerfeld factor can be set equal to 1 if

$$\frac{2\pi Z}{137\beta} \ll 1 \quad \text{and} \quad \frac{2\pi Z}{137\beta'} \ll 1 \ , \tag{19}$$

where β and β' are equal to v/c for the initial and final electrons, respectively. This is a reasonable approximation for electron energies above 100 keV and for $Z = 1$.

A comparison of the final result (Wharton, 1961) with equation 18 yields the Gaunt factor for any value of $h\nu/kT$:

$$g(h\nu, kT) = \frac{\sqrt{3}}{\pi} K_o \left(\frac{h\nu}{2kT}\right) \exp\left(\frac{h\nu}{2kT}\right) , \tag{20}$$

where $K_o(x)$ is the zero-order modified Bessel function of the second kind. With the asymptotic expansions of K_o (Abramowitz and Stegun, 1964), we obtain

$$g(h\nu, kT) = \begin{cases} \frac{\sqrt{3}}{\pi}\left[\ln\left(\frac{4kT}{h\nu}\right) - 0.577\right] \exp\left(\frac{h\nu}{2kT}\right) \text{ for } h\nu \ll kT, \\ \frac{\sqrt{3}}{\pi}\sqrt{\frac{\pi}{2}\frac{2kT}{h\nu}} = 0.9772\sqrt{\frac{kT}{h\nu}} \quad \text{for } h\nu \gg kT. \end{cases} \tag{21}$$

Equation 21 shows that the limiting value of the Gaunt factor for $Z = 1$ and for large photon energies is not equal to one, but is approximately equal to $\sqrt{kT/h\nu}$.

The observed spectra of several X-ray sources can be interpreted as due to bremsstrahlung of electrons with a Maxwellian distribution at a temperature between 10^7 and 10^8 °K. If the electron gas contains a wide range of kinetic temperatures, then the main contribution to the overall spectrum of the bremsstrahlung curve for a temperature T comes from energies around kT. Both arguments show that the full Gaunt factor must be used in the formula for the bremsstrahlung spectrum.

For photon energies above 10 keV which are comparable to or greater than kT, the contribution from electron-electron bremsstrahlung becomes significant. Electron-ion (Z = 1) bremsstrahlung is dipole in nature while electron-electron bremsstrahlung is quadrupole in nature; one expects their ratios to be mc^2/kT. Maxon and Corman (1967) have calculated electron-electron bremsstrahlung from a Maxwellian hydrogen plasma in the non-relativistic Born approximation. The ratio of quadrupole to dipole emission at a particular photon energy, B ($h\nu/kT$), can be approximated by

$$B\left(\frac{h\nu}{kT}\right) = \left(2 + 0.64\,\frac{h\nu}{kT}\right)\,\frac{kT}{mc^2}\quad,\quad \text{for } h\nu \gtrsim kT \approx 10 \text{ keV}. \tag{22}$$

For example, in a hot Z = 1 gas at kT = 10 keV, the electron-electron contribution is 7% of the electron-ion emission at a photon energy of $h\nu$ = 25 keV. The differential bremsstrahlung spectrum for Z = 1 is therefore best represented in the energy region considered here by a function of the form

$$P(h\nu,\ kT) = A\,\frac{1}{\sqrt{kT}}\,\exp\left(-\frac{h\nu}{2kT}\right)K_o\left(\frac{h\nu}{2kT}\right)\cdot \left[1 + \left(2 + 0.64\,\frac{h\nu}{kT}\right)\frac{kT}{mc^2}\right]\,\frac{1}{h\nu}\quad. \tag{23}$$

This equation will be used later in the data analysis.

CHAPTER III

THE DETECTORS

A. Introduction

The X-ray sensing equipment consists of three elements: a gas proportional counter, an alkali-halide scintillation crystal, and a combination of active and passive shields which also acts as a collimator. X-radiation from a well-defined aperture is detected by this counter arrangement, so that we may speak of it as an X-ray telescope.

Figure 1 shows a schematic diagram of the X-ray telescope. A krypton gas proportional counter is located in front of a CsI(Tl) scintillation crystal, and both are located inside a plastic scintillator cup. The light output pulses of the CsI crystal and the plastic guard counter are distinguished by their rise times. The proportional counter is also connected in anticoincidence with the scintillators. The plastic cup is the innermost part of a three-element graded shield which consists of tin on the outside and copper in the middle.

B. The Proportional Counter

The X-ray transmission of a layer of air with $d = \rho x = 3$ g/cm^2 exceeds 0.01 at 15 keV and exceeds 0.1 at 20 keV. Krypton gas at 1 atm. pressure was selected for a proportional counter of 5.08 cm depth so that the absorption of this gas exceeds 0.5 at all photon energies between the K absorption edge at 14.323 keV and approximately 24 keV. The absorption curve of 0.0188 g/cm^2 krypton as a function of photon energy is drawn in Figure 2 as a solid line.

The broken line shows the product of this absorption function times the transmission functions of a film of aluminized mylar (0.00254 cm polyester, 0.00381 cm Al), of the beryllium plate at the top of the pressurized detector housing (0.3175 cm Be), and of the beryllium entrance window of the proportional counter (0.0127 cm Be).

The proportional counter has the shape of a right cylinder, its inner dimensions being 5.08 cm diam. × 5.08 cm length. The original version had a button-type anode; the supporting grids for the entrance and exit beryllium windows (0.0127 cm Be) and the side walls were made of Monel. Later counters had a wire electrode, and the wall material was aluminum. The full-width at half maximum (FWHM) of the response to a 25 keV line (main peak of the response to Sn-119 m, see below) was 20% for the earlier counters and 32.5% for the later models.

The energies of emission lines from some radioactive sources which were used in the energy calibration of the proportional and scintillation counters are listed in Table I. The relative line intensities have been adopted from the measurements of Holt (1967a). The "effective energy" is the peak energy for the superposition of several Gaussian response curves with intensities and mean energies as given in the table. The widths of the Gaussian curves were adjusted to correspond to the energy resolution of the proportional counter and the scintillation crystal, respectively. Also shown in Table I is the line broadening due to the composition of each calibration line.

A typical energy calibration curve of the proportional counter is shown in Figure 3. The solid line connects the effective line energies of radioactive

sources plotted as a function of the channel number. The curve is not linear, but it never deviates more than 1 keV from the linear approximation (broken line). This nonlinearity is caused by the detector itself; independent tests with calibrated pulses of the same shape as the signals from the proportional counter showed that the pulse-height analyzer was linear. The highest energy calibration point shown in Figure 3 (31.5 keV, channel 54) would be expected to fall into channel 59, but the upper cutoff at channel 56 distorts the line response so that it appears to be peaked at a lower channel number.

With the known energy calibration, one can convert the observed response to radioactive calibration sources into an energy spectrum. This is done in Figure 4 for Sn-119 m, using the nonlinear (solid line) and the linear (broken line) energy calibration curves. The half-width energy intervals at half maximum for the main and the escape peak are 4.3 and 3.63 keV, respectively.

It is apparent from Figure 4 that the escape peak is not symmetrical; this fact is only partially explained by the influence of the lower threshold. As will be discussed in more detail later, escaping characteristic krypton K radiation can be absorbed in the CsI crystal. The K-line energy (12.6 keV) is below the threshold of the crystal, but a voltage equivalent to two channels is added to the combined proportional counter/scintillator output which therefore shifts the simultaneous escape signal for the proportional counter. According to the krypton counter calibration, this channel increment corresponds to approximately 1 keV. Including the line broadening, we finally arrive at a relative resolution of 32.5% FWHM at 25 keV and 54% FWHM at 12 keV. The full-width

energy resolution at half maximum can be represented by

$$\Delta E = \sqrt{19 + 1 \cdot 9E}\ , \tag{24}$$

where energies are measured in keV.

In an ideal proportional counter, a finite resolution is due to: (a) the number of ion pairs formed by an incident photon, and (b) the subsequent multiplication process, both of which are subject to statistics on finite numbers. The multiplication factor of our counters is of the order of 10^4 for 2000 V operating potential at the proportional counter anode. Depending on the choice of the Fano function (Fano, 1947; Curran and Wilson, 1965; Aitken, 1968), one arrives at a theoretical resolution of typically 8% at 25 keV. The main contribution is caused by fluctuations in the number of ion pairs formed so that the variance is proportional to the energy. In other words, the full width at half maximum is proportional to the square root of the energy.

The strong energy-independent contribution in addition to the linear term under the square root in equation 24, indicates that the second step (b), above, is responsible for the large energy dispersion. Since the electrode and detector configurations are unfavorable, charge amplification, charge collection, and dead regions introduce a constant term into the variance of the energy dispersion.

When a photon of energy E is absorbed in a given material, fluorescence X-radiation from K, L, and other shells can be emitted by the material, provided that E is above the absorption edge for these shells (Appendix A). The escape factor, $\eta(E)$, is defined as the probability of emission of a fluorescence X-ray for every photon that has been absorbed in the detector. There is no

simple analytical way of calculating η for the proportional counter because the calculation would have to take full account of the detector configuration. We can estimate the value of the escape factor in the following manner. The K-shell fluorescence yield for krypton is $\beta_K = 0.66$ (Bergström and Nordling, 1965; Fink et al., 1966). The probability of creating a K-shell vacancy is taken to be (Grodstein, 1957)

$$\alpha_K = \frac{1}{1 + (\frac{1}{2})^3 + (\frac{1}{3})^3} = 0.86 . \tag{25}$$

The product $\alpha_K \beta_K$ must be multiplied by the average attenuation of the K-shell fluorescence photons. If the average path length of these photons is assumed to be about 1/3 of the characteristic detector length, s = 5.08 cm, one arrives at an escape factor

$$\eta \approx 0.48. \tag{26}$$

The escape factor was also determined experimentally by a comparison of the source-response curves with calculated response curves. The energy resolution as a function of energy must be accurately known in order to obtain reasonable precision in the determination of η. Observations of the primary and escape peaks in the response to Sn-119 m in different proportional counters resulted in escape factors of

$$\eta = 0.50 - 0.52. \tag{27}$$

C. The CsI(Tl) Scintillation Crystal

When the present series of experiments began, two alkali halide scintillators were in general use: NaI(Tl) and CsI(Tl). CsI(Tl) has an efficiency for

the conversion of absorbed energy into light equal to approximately 30% of that of NaI(Tl) (Aitken, 1968), and a rise time of 1.8 μsec compared with approximately 1 μsec for NaI(Tl). CsI(Tl) is therefore more useful for the Phoswitch technique of pulse-shape discrimination; in addition, the mechanical properties of the CsI crystal are more favorable, allowing easier handling of the crystal.

The scintillation crystal has the shape of a right cylinder, 0.2 cm in height and 5.08 cm in diameter. The counter is optically thick in the energy region from 20 to approximately 100 keV.

The "effective" line energies for groups of closely spaced lines from radioactive sources have been computed with a reasonable estimate for the scintillator resolution. They are listed in Table I under the heading "Effective Energy, CsI." A typical energy calibration curve is drawn in Figure 5. The lowest-energy points (Sn-119 m at 24.7 keV and Cd-109 at 22.5 keV) do not fall on the calibration curve since the lower cutoff distorts the source-response curve and effectively shifts the observed peaks.

With the known energy calibration, we can measure the energy resolution of the scintillation counter with all processing electronics in operation. The half-width at half maximum for the 86.5 keV line of Eu-155 is 14.5 keV; the upper half of the response is distorted by the high-energy cutoff. This value corresponds to a relative FWHM of 33.5%. The effective line energy of Ba-133 is 31.5 keV, a spreading of 0.6 keV is caused by the line composition (Table I). At this energy the resolution is 5 keV HWHM, corresponding to a value of 29% FWHM.

The Phoswitch rejection efficiency was reduced at energies above approximately 60 keV. We have therefore restricted the data analysis to energies below 60 keV.

The calculation of the escape factor η is discussed in appendix A. A graphical representation of η as a function of energy is given in Figure 6.

D. The Electronic Circuitry

In this section we summarize the detector pulse-selection criteria and the method of data recording (Doong and Noordzy, 1966). For simplicity we introduce the following labels for pulses from the three detectors: "A" events occur in the proportional counter; "B" events are pulses originating in the CsI scintillation crystal; and "C" events originate in the plastic scintillator cup. A block diagram of the pulse logical analysis is given in Figure 7.

1. Proportional counter events (A counts). When an X-ray photon interacts in the krypton proportional counter, a charge Q, proportional to the amount of energy deposited in the detector, is produced. This charge is converted into a voltage signal by a charge-sensitive amplifier. If this signal corresponds to an energy between 10 and 30 keV, then it is analyzed and recorded as a mode 1 event, provided all other requirements (Table II) are met and the system is not busy. Whether the system is busy processing some other event or not, the event is stored as an A count in the prescaled A accumulator. This bit-rate signal is read out every 5 seconds (mode 2, see Table II).

2. CsI scintillation crystal events (B counts). Signals from either or both the CsI crystal and the plastic scintillator can be received in the

photomultiplier. The procedure by which a signal from the plastic scintillator is identified as a C event will be discussed below. At present we assume that B signals have been extracted. They are first amplified and shaped. A valid B signal must fulfill a pulse-height criterion equivalent to 20 keV $\leq$ E $\leq$ 100 keV. The subsequent analysis and recording as a mode 0 event proceeds like that for an A event, provided the other requirements (Table II) are met and the system is not busy. All B events are stored in a prescaled accumulator. The B bit rate is read out together with the A bit rate every 5 sec (mode 2).

During the 100 msec period immediately preceding the mode 3 command pulse, B events with E > 100 keV are accepted and stored in a B overload accumulator. This information is read out during the mode 3 readout sequence.

3. Plastic scintillator events (C counts). C events are distinguished from B events by their shorter rise time. The signal from the preamplifier is simultaneously applied to a 40 nsec shaper with a threshold detector (equivalent to E > 10 keV) and to a peaking circuit. Plastic events of typically 30 nsec rise-time and E > 10 keV will cause the two outputs to coincide and are accepted as valid C pulses. A stop gate is then activated which prevents the preamplifier signal from being processed in the pulse-height analyzer and which blocks the B bit-rate accumulator.

CsI events with a rise-time between 0.5 and 1.8 μsec will be analyzed in both the B and the C systems. These B pulses are analyzed by four C threshold detectors which are set at 10, 20, 40, and 100 keV. An indication of the number of C threshold detectors that have fired is recorded along with the pulse-height analysis information for every B event (mode 0). B events with

simultaneous indications that one or more C threshold detectors have fired were not used in the subsequent data analysis. Valid C events with E > 100 keV are counted during a 100 msec interval preceding a mode 3 command pulse and recorded in the C overload accumulator. Both the B and C overload rates are read out every minute (mode 3).

4. Mode 2. As previously mentioned, the A and B bit rates are recorded every 5 seconds. The rate was first scaled by a factor of 12 (Experiments 1 - 5), and later by a factor of 8 (Experiments 6 - 11). In the latter case, a maximum recording capacity of 64 × 8 = 512 counts per 5 sec in each of the A and B channels was available. The mode 2 information serves as a check on the deadtime correction.

5. Mode 3. Mode 3 occurs every 12 mode-2 readouts, i.e. every minute. For a duration of 100 msec, the number of B(E > 100 keV, $\bar{C}$ with E > 10 keV) and the number of C (E > 100 keV) events are recorded.

6. Mode 7. Mode 7 is a time mark which is recorded on tape every 12 occurrences of mode 3 (every 12 minutes). The count of the number of times mode 7 has occurred since the system was last turned on is recorded in 64 channels. After 64 × 12 = 768 minutes, this count recycles.

7. Modes 4, 5, and 6. For detector telescopes which were rotated in azimuth angle and programmed in elevation angle, magnetometer pulses were recorded on tape as housekeeping information. The data recorded in mode 4, 5, and 6 are identical to those in mode 0, 1, and 2, respectively. The only difference is an additional mark which is added in the third of the three mode-symbol tracks on the recording tape with binary values of 2^0, 2^1, and 2^2.

A signal from the magnetometer will cause addition of $2^2 = 4$ to the mode symbol of the next data record, for example mode 0, 1, or 2. The addition is maintained until the next occurrence of mode 2, after which the addition is inhibited for at least 10 sec.

E. Interaction Between the Proportional Counter and the Scintillation Crystal

Because of the proximity of the proportional counter and the CsI crystal, and the criteria for event analysis (Table II, section III D), some interaction between the counters is possible. For example, (a) K fluorescence radiation of the proportional counter can be absorbed in the crystal, and (b) K fluorescence radiation of the CsI crystal can be absorbed in the proportional counter.

(a) The K fluorescence radiation (section III B) of krypton can escape from the proportional counter and may be absorbed in the scintillator. There the event is too low in energy to be accepted as a valid CsI event; therefore, the anti-coincidence requirements are not fulfilled. It is apparent from section III D and from Figure 7 that a voltage equivalent to 12.6 keV is added to the voltage output for the escape peak in the proportional counter. Therefore, the escape peak is shifted in energy by an amount which equals two channels in the system used here, i.e., approximately 1 keV equivalent photon energy in the proportional counter.

In order to obtain an estimate of the relative probability ϵ of this interaction, we multiply the escape factor of the proportional counter by the probability of escape into the CsI crystal. The latter will be of the order of the solid

angle Ω_{CsI} of the CsI crystal seen from the center of the proportional counter, divided by 4π:

$$\epsilon = \eta_{K,\ Kr}(E) \cdot \frac{\Omega_{CsI}}{4\pi} \ . \tag{28}$$

The escape peak will be shifted by an amount of energy $\Delta E \approx 1$ keV, where ΔE is subject to resolution spreading. For E = 25 keV, the probability ϵ is

$$\epsilon = 0.52 \cdot \frac{1}{4} = 0.13 \ . \tag{29}$$

(b) The K fluorescence radiation of CsI can escape from the entrance surface (appendix A) and may be absorbed in the proportional counter. If the primary photon energy was between 35 and 50 keV, then the energy deposited in the crystal is between 5 and 20 keV, and again the pulse will not be accepted as a valid CsI crystal event. The 30 keV escape photon can be accepted as a valid event in the proportional counter even though it stems from a primary photon with an energy between 35 and 50 keV.

In order to estimate the magnitude of this effect, one must consider the response of both detectors to a common source. We assume a power-law spectrum incident at the top of the atmosphere. Then we compute the attenuation in 3 g/cm^2 of air as well as in the beryllium covers, etc., and determine the response to the remaining spectrum in the proportional and scintillation counters. The total flux of escaping photons for escape through the entrance surface of the crystal and for primary energies between 35 and 50 keV is given by

$$I_{escape} = \int_{35\ keV}^{50\ keV} \eta\ (E)\ I_{resp}\ (E) \cdot dE \ . \tag{30}$$

I_{resp} (E) is the attenuated source photon flux which is absorbed in the CsI crystal. As the next step we determine the absorption probability and the counting rate distribution in the proportional counter for the line at E = 30 keV. For exposure of both detectors to a power-law source spectrum of index 2, we find that the contribution of escape from the CsI crystal into the proportional counter amounts to 6.2 percent at 17.5 keV, 2.5 percent at 24 keV, and 8.8 percent at 30 keV. This small contribution is shifted by an amount equivalent to $0 \leq E \leq 1$ keV and is again subject to resolution spreading.

F. Geometric Factors

Figure 1 shows that the Sn - Cu - Foam - $CH_{1.2}$ shield arrangement also acts as the collimator for the proportional and scintillation counters. The geometric factor for the scintillation crystal is defined as

$$GF = \langle A\Omega \rangle = 2\pi \int_0^{\theta_o} A_o(\theta)\, \alpha(\theta) \sin\theta \, d\theta \quad , \tag{31}$$

where $A(\theta)$ is the detector area for a parallel beam of photons incident on the detector without modulation. The cut-off angle θ_o is defined by the collimator geometry. The factor $\alpha(\theta)$ accounts for other modulation effects, notably the ring and disk placed in front of the X-ray telescope.

Figure 8 shows the effective exposure area $A(\theta)$ of the scintillation crystal as a function of the angle θ from the detector axis. This quantity was found experimentally by placing a point X-ray source at a large distance compared to the detector and collimator dimensions and at various angles θ. The

observed counting rate was multiplied by a normalization factor to give the calculated value at zero angle

$$A\ (\theta = 0°) = \pi r_o^2 = 20\ cm^2. \qquad (32)$$

The solid line in Figure 8 represents the effective exposure area for the unobstructed detector. It is very close to the calculated curve for the same detector geometry. The broken line shows A (θ) for the detector with modulation ring and disk.

A characteristic of the response curve is the angle at which the effective area drops to half its maximum value. The FWHM angle is given in Table III. The geometric factor is then simply calculated by evaluating the integral

$$GF = 2\pi \int_0^\pi A\ (\theta)\ \sin\theta\ d\theta\ . \qquad (33)$$

The curves in Figure 8 were obtained with an emitter of X-rays at an energy of E $\approx$ 25 keV (Sn-119 m). The effective exposure area for high photon energies is larger than that for lower energies since the collimator is less effective in the former case. Edge effects and an increased contribution from Compton scattering off the inside walls increase the effective exposure area. A summary of geometric factors at 25 keV and at approximately 75 keV (Bi-109) is presented in Table III for the proportional and scintillation counters with and without modulation. The value for the scintillation crystal response at 75 keV in the presence of the modulation assembly has been inferred from the other three distributions for this detector. The appropriate exposure factor is therefore shown in parentheses.

The definition of the geometric factor for the proportional counter is analogous to that of the scintillation crystal, but now the detector is not thin compared to the collimator length. One has to consider several thin layers each with a different absorption probability for incoming X-rays, and then evaluate the geometric factor of each layer of krypton gas. The variation in the charge-collection efficiency at different points in the counter also plays a role.

The effective area as a function of angle θ from the detector axis has been evaluated experimentally. The resulting curves are similar to those for the scintillation detector. The full-width angle at half-maximum effective area is 27.6°. The geometric factors for the unmodulated and modulated counters are given in Table III.

G. Response of the X-Ray Telescope to Gamma Radiation

The telescope shield consists of one active layer and several passive layers. The active part of the shield is a plastic scintillator cup (Pilot B, equivalent chemical formula $CH_{1.2}$) which is a part of a graded shield consisting of tin on the outside, copper, Ecco Foam, plastic, and aluminum on the inside.

This shield loses some of its effectiveness at higher energies; it is therefore necessary to investigate the quality of the shield for electromagnetic radiation of energy within the range of interest (10 - 100 keV) and above. A suitable parameter is the transfer function $T(\Sigma, E_1, E_2)$ for the CsI crystal. It is defined as the effective geometric factor of the CsI crystal (with

dimensions cm^2 ster) for photons of energy $E \geq E_2$ which deposit an energy E' in the crystal, provided that E' lies between E_1 and E_2. In other words, we consider the X-ray telescope immersed in an isotropic flux of photons of energy E greater than E_2 and define the transfer function TF (E, E_1, E_2) as the effective geometry factor for photon measurements at energies between E_1 and E_2. The quantity consists of two components: a contribution from photons E which enter through the aperture, TF_{Ap}, and one due to photons which first traverse the shield before interacting in the crystal, TF_s:

$$TF_{ap}(E, E_1, E_2) = \iint_{\text{Aperture}} F(\alpha, E, E_1, E_2)\, d\Omega, \tag{34}$$

$$TF_s(E, E_1, E_2) = \int_{\text{Shield}} F(\alpha, E, E_1, E_2) \exp\left[-(\Sigma x_i \mu_i(E)/\sin\alpha\right] \cdot 2\pi d(\cos\alpha). \tag{35}$$

The definition of F (α, E, E_1, E_2) is similar to the definition of TF (E, E_1, E_2), except that it refers to photons which are incident at an angle α from the detector axis. The depth of the i-th layer of the shield is x_i, and μ_i (E) is the total absorption coefficient of this layer material.

We will now consider the experimental evaluation of the transfer function TF. For this purpose we cannot make use of equations 34 and 35 in their present form. We define η_{ap} (E, E_1, E_2) as the probability that a photon of energy E, which interacts in the crystal after entering through the aperture, deposits an amount of energy E' between E_1 and E_2. The definition of η_s is similar: a photon of energy E, that would interact in the crystal in the

absence of a shield, must traverse the shield and deposit energy between E_1 and E_2 in the crystal.

η_{ap} and η_s can be found experimentally. We first determine the total counting rate at all energies for the bare crystal caused by a source of photons of energy E. Then, with the same relative source-detector configuration plus the shield in the case of η_s, we measure the counting rate at energies between E_1 and E_2. The ratio of the latter to the former rate is η_{ap} and η_s in absence or presence of the shield, respectively. The transfer functions are given by

$$TF_{ap}(E, E_1, E_2) = \eta_{ap}(E, E_1, E_2) \; \langle F\Omega \rangle_{ap} \; \left[1 - \exp(-\mu(E)\, x_o)\right] \quad (36)$$

and $$TF_s(E, E_1, E_2) = \eta_s(E, E_1, E_2) \; \langle F\Omega \rangle_s \; \left[1 - \exp(-\mu(E) \langle x \rangle_s)\right] \quad (37)$$

where x_o is the crystal thickness and $\langle F\Omega \rangle_{ap} = 3\ cm^2 ster$ (section III F). For an isotropic photon distribution we have

$$\langle F\Omega \rangle = \int_{-1}^{1} F_o \cos\alpha \cdot 2\pi \, d\cos\alpha = 2\pi F_o \approx \langle F\Omega \rangle_s \quad (38)$$

and $$\langle x \rangle = \frac{\int_{-1}^{1} A \cos\alpha \, \frac{x_o}{\cos\alpha} \, 2\pi \, d\cos\alpha}{\int_{-1}^{1} A \cos\alpha \cdot 2\pi \, d\cos\alpha} = 2 x_o \approx \langle x \rangle_s . \quad (39)$$

Experiments verified that $\eta_s(E, E_1, E_2)$ is a weak function in α, and η_s was therefore assumed to be constant.

Figure 9 shows the total transfer function TF

$$TF(E, E_1, E_2) = TF_{ap}(E, E_1, E_2) + TF_s(E, E_1, E_2) , \quad (40)$$

for E_1 = 20 keV and E_2 = 60 keV. Four values of the energy E were used in the experiments: 122 keV (Co-57), 357 keV (Ba-133), 622 keV (Cs-137), and 1.3 MeV (1.17 and 1.33 MeV of Co-60).

We can use the transfer function TF and the geometric factor GF (previous section) to estimate the counting rate due to the atmospheric background flux at balloon altitudes. We assume the atmospheric X- and gamma-ray flux to be isotropic and use the spectrum measured by Peterson et al. (1967a) at d = 3.5 g/cm^2 and at a local vertical cutoff rigidity R = 5.1 GV. The transfer function and the geometric factor as a function of energy are then folded with the atmospheric photon spectrum, and the resulting counting rate is adjusted to a residual atmospheric depth of d = 3.0 g/cm^2. The counting rate at this depth caused by the atmospheric and detector-generated background is shown in Figure 10 (section III J). For the CsI crystal of an X-ray telescope without modulation ring and disk, we find the following counting rates:

1.8 counts/sec is the total counting rate caused by the atmospheric and the detector-generated background (the contribution from the cosmic X-ray background, approximately 0.8 counts/sec, is not included). Of this rate:

1.1 counts/sec are caused by the atmospheric background photons with energies between 22 and 60 keV, and

0.5 counts/sec are caused by the atmospheric background gamma rays with energies above 60 keV. Therefore, the remainder,

0.2 counts/sec, are generated in the telescope by other effects, e.g., by charged particles because of incomplete rejection by the Phoswitch.

It is difficult to estimate the possible error in each of the numbers quoted above. Therefore, a large error may be attached to the last-mentioned counting rate which cannot be accounted for. Nevertheless, these numbers show that a reduction of the solid angle of the field of view would lower the counting rate produced by atmospheric and cosmic X-rays and would therefore reduce the total counting rate. These considerations also show that it is not useful to reduce the aperture angle below a certain value without simultaneously reducing the counting rate background due to gamma rays and other effects.

H. The Atmospheric Transition Curve

Figure 11 shows typical atmospheric transition profiles for the scintillation and proportional counters. The CsI crystal data in the 22 - 60 keV interval are shown as double bars, and the krypton proportional counter data between 12 and 28 keV are represented by single bars. The measurements were taken by detector E during Experiment 10 (chapter IV).

In order to find the contribution of the attenuated cosmic diffuse X-ray background to the counting rate at ceiling altitude, it is necessary to extrapolate the transition curve to that altitude. Such an extrapolation predicts the dependence of the sum of the detector-generated and the true atmospheric backgrounds. We will study the atmospheric transition profile for altitudes above those corresponding to the maximum in the counting rate. This maximum is the equivalent to the "Pfotzer maximum" and will be referred to as the "peak" in the transition curve. Several analytical functions have been employed to approximate this section of the atmospheric transition curve, for example

$$I(p) = a - b \exp(-p/c) \tag{41}$$

(Anderson, 1961; Brini et al., 1965a),

$$I(p) = a + b\,p \tag{42}$$

(Peterson, 1967b), and

$$I(p) = a\,p^{b} \tag{43}$$

(Bleeker et al., 1968).

The sum of the primary and secondary cosmic-ray intensities as a function of pressure can be described in lowest-order approximation by a function of the type

$$I(p) = a \exp(-p/b) - c \exp(-p/d), \tag{44}$$

(Ghielmetti et al., 1964b),

where b represents the absorption length, of the order of 160 g/cm^2, and d is the mean interaction length, of the order of 86 g/cm^2. The observed atmospheric transition curves for X-radiation can be fitted by functions of the same type. By means of computer calculations, least-square fits for the parameters a, b, c, and d were found for the transition curves of the various data sets. For example, the (6.7 - 68.0) g/cm^2 section of the proportional counter data of Experiment 10, detector E, can be best described by

$$I(p) \propto 3976 \exp(-p/143) - 3617 \exp(-p/75)\ . \tag{45}$$

The appropriate curve is given in Figure 11 as a solid line.

It is apparent that the calculated lines present a good fit to the atmospheric transition profiles, but it is not suggested that the observed counting rate is simply due to the primary and secondary atmospheric cosmic ray intensity. A brief discussion will illuminate this point.

(a) Atmospheric X-radiation at high altitudes is assumed to be primarily caused by the soft component of secondary cosmic radiation in the atmosphere. Some contributions to the atmospheric production of X-radiation and their relation to the cosmic-ray flux will be discussed in appendix B.

(b) A study of the Phoswitch properties showed that the rejection threshold shifts at high counting rates, so that an increased number of plastic pulses are accepted as valid CsI crystal events. If we define a peak-to-ceiling ratio (PCR) as the ratio of counting rates at the peak of the atmospheric transition curve, e.g., at 90 g/cm^2, to that extrapolated to ceiling altitude, e.g., at 3 g/cm^2, then the effect just described will increase the PCR for the scintillation crystal. The PCR for the proportional counter will, of course, not be affected.

(c) Observations have shown that the PCR increases between 20 and approximately 180 keV, and then gradually decreases again up to a few MeV (Peterson et al., 1966a; Peterson et al., 1967a; Peterson, 1967b). If this trend can be extrapolated to lower energies, a lower PCR will be expected for the proportional counter data than for the scintillator data.

(d) Some CsI crystal events are due to higher-energy photons that have undergone Compton scattering (see section III G). The considerations of (c) apply in this case.

We can now extrapolate the atmospheric transition curves to ceiling altitude and then use the calculated contribution of the diffuse cosmic X-ray background to infer the expected counting rate at ceiling altitude. Considering the effects discussed above, no great emphasis should be placed on the extrapolation or on the results derived from this procedure.

Table IV lists the extrapolated and the observed counting rates at ceiling altitude (in counts/sec-cm^2-ster) for various detectors and several experiments. For each case, Table IV also shows the calculated contribution from the diffuse cosmic X-ray background. According to a summary given by Gould (1967), an average of several observations was used to define a two-component photon spectrum of the diffuse cosmic X-ray background:

$$J(E) = 10\,E^{-1.5} \quad \text{for } E < 23 \text{ keV}$$
$$\text{and} \quad J(E) = 100\,E^{-2.23} \quad \text{for } E \geq 23 \text{ keV} \,, \tag{46}$$

where J is the photon flux in units of photons/cm^2-sec-ster-keV and E is measured in keV. Appropriate adjustments for absorption above the detector as well as the detector efficiency and the geometry factor have been included.

The counting rate at ceiling altitude is approximately 10% higher than the rate predicted from the extrapolation plus the computed contribution from the cosmic diffuse X-ray background. This difference can be understood as caused by the shape of the atmospheric transition curve. The "peak" section is too high compared with the higher-altitude section, thereby producing an extrapolated ceiling rate which is too low.

J. Latitude Dependence of the Detector-Generated and the Atmospheric X-ray Backgrounds

The following procedure was carried out for several experiments: The contribution of the diffuse cosmic X-ray background R_d was subtracted from the counting rate at ceiling which was observed when no discrete cosmic X-ray sources were within the field of view. The resulting net counting rate was

adjusted to a common atmospheric depth of 3.0 g/cm^2 and was divided by the geometry factor GF (section III F). Figure 10 shows the net adjusted event rates (in counts/cm^2-sec-ster) for the scintillation crystal,

$$r = (R_{obs} - R_d) \;/\; GF = a + D/GF \quad , \tag{47}$$

caused by the atmospheric (a) and the detector background (D/GF), as a function of the local vertical cutoff rigidity (in GF). Data from several experiments (Experiments 4, 9, 10 and 11) and several detectors (A, E, G and W) have been used. The points 4 A, 10 G, 4 A, 11 G, and 11 G define a curve of decreasing rate r with increasing local cutoff rigidity. The points 4 W, 9 E, 10 E, 4 W, 11 E, and 11 E show more scattering around another curve, not shown in Figure 10, which is roughly equidistant from the first one. The detectors E and W were partially occulted by a modulation disk and ring, while A and G were not so occulted. The geometry factors GF (section III F) were applied to the net event rate $r \cdot GF = R_{obs} - R_d$, which is derived from the true atmospheric ($a \cdot GF$) and detector-produced events (D) (a and D can be assumed to be independent of the geometric factor of the detector). The net rate r is therefore larger for the occulted detectors which have a smaller geometry factor. This explains the shift between the two sets of data points shown in Figure 10 and the resulting background-versus-rigidity curves.

The corresponding curve for the proportional counter could not be derived because some of the data points contradict each other. In general, the curve of proportional counter event rate versus rigidity is expected to reflect only the change of the atmospheric X-ray background with rigidity.

The shape of the curve of background versus rigidity shown in Figure 10 can be expected for any observation which is related to the charged-particle flux in the earth's magnetic field. A comparison of the latitude dependence of the X-ray flux at ceiling altitude with the latitude dependences of other particle fluxes might give a clue as to the production mechanisms for the observed flux. Clearly, a much wider range in latitude would be required to make any definitive statements. Some aspects of this problem are discussed in appendix B.

CHAPTER IV

SUMMARY OF THE BALLOON FLIGHTS

A. Summary of Flight Data

Between December 1965 and July 1967, 11 balloon-borne X-ray experiments were conducted. The flights have been labelled in chronological order.

Table V lists the relevant information for eight of the flights. Launch data and the times for beginning and end of ceiling coverage are given, as well as the range of residual atmospheric depths and the range in local vertical cutoff rigidities that were encountered during the main portion of each experiment. The K_p indices are also presented to indicate geomagnetic activity during the period of ceiling coverage. The names of the detectors that were flown in each experiment together with the scanning method that was used for each detector are also listed. The following rows in Table V summarize information on celestial objects that are relevant to each experiment. Solar flare information is given in the first row: the universal time of the maximum phase and the importance of each flare are quoted (ESSA, 1966, 1967). Finally, the names of known X-ray sources or of prominent directions in the celestial sphere are stated along with the times of their meridian transits. All abbreviations used are explained at the bottom of Table V.

B. The Balloon Gondola

Three scanning mechanisms were used in the present series of experiments: the vertical, the oriented, and the rotating schemes (Table V).

A vertical detector experiment, with or without modulation assembly (see section III F), performs a simple meridian-transit observation of an X-ray source. A necessary restriction is that the source must be within a band of width $\approx 25^\circ$ centered at the declination of the detector axis. A misalignment of the detector axis or of the modulation assembly is averaged out for free-rotating gondolas or for gondolas rotating with constant azimuthal velocity.

Optical observations during Experiment 1 showed that a free balloon gondola rotates with changing direction and angular velocities of between 0.06 and 0.2 rpm. The upper limit to the pendulum motion of a free balloon gondola was found to be approximately 0.5°.

The oriented detection scheme changes the effective latitude of the detector by tilting it to a certain fixed zenith angle. A band of the sky can be scanned by the meridian transit method; this band is then centered at the declination given by the new direction of the detector axis. Of course, the azimuth angle must be kept constant. We have aligned the detector axis in the plane of the meridian and have used the local direction of the magnetic field as a reference direction. Upon a deviation from the correct alignment with respect to the magnetic field, a magnetometer generated an error signal which controlled the release of an appropriate amount of gas through a jet nozzle and the resulting torque brought the gondola back to its proper azimuthal attitude. The correct

alignment of the detector axis and the modulation assembly is very important in this detection scheme.

The rotating scanning method uses the magnetic field as a reference to adjust the otherwise continuous rate of change of the azimuth angle. The gondola rotates through 360° over a period of 10 minutes; a reaction wheel serves as a reservoir of angular momentum. A signal is recorded on magnetic tape (section III D) whenever the magnetometer senses the direction of magnetic east or magnetic west; another pulse is generated when the detector points toward north. These three marks provide the directional information necessary for the data analysis.

In addition to the rotational motion, the zenith angle of the detector can be programmed so that the axis scans through a celestial point or tangentially along a celestial curve once during every rotation. Thus the projection of the detector axis executes a spiralling motion on the celestial sphere. Inaccurate alignment of the detector axis is not critical with this scanning method.

CHAPTER V

METHODS OF DATA ANALYSIS

Two different procedures have been used in the analysis of the data and the extraction of the most probable source spectra. Procedure 1 was used when a channel-by-channel analysis of the data was warranted. Procedure 2 was used for all observations of cosmic X-ray sources.

A. Data Analysis Procedure 1

In each of the present series of measurements, an observed spectrum is divided into a number of discrete energy intervals of finite width, corresponding to the 64 channels of the pulse-height analyzer. The number of counts observed in each channel versus the energy-equivalent of the channel number may be represented by a vector V^O. The source function can be approximated by a similar vector V^S. Various media and devices act as operators on the source function. In our representation we can describe these operators by matrices M.

The matrix which describes the influence of a layer of air of thickness d above the detector is simply given by

$$M_{ii}^{air} = \exp\left[-\mu_{air}(E_i) \cdot d\right] \qquad (48)$$

and $M_{ij}^{air} = 0 \qquad \text{if } i \neq j \ ,$

where μ_{air} is the scattering coefficient of air without coherent scattering (Grodstein, 1957). Similar matrices describe the attenuation in the various layers of aluminized mylar, beryllium, etc., and in the krypton proportional counter gas in the case of the CsI crystal data analysis. All matrices are symmetric and the off-diagonal elements are equal to zero.

The matrix M^{Esc} describes the escape effect in the proportional counter and in the scintillation crystal. M^{Esc} has the same shape in each case, but the numerical values are different. The probability of escape is assumed to be described by $\eta(E)$ (sections III B and III C and appendix A). For simplicity we combine all the characteristic line energies into one line energy E_K, i.e., $E_K = 12.6$ keV for the proportional counter and $E_K = 30.0$ keV for the CsI crystal. If the subscript i denotes the rows of a matrix and j denotes the columns, then M^{Esc} is described by

$$M_{ii}^{Esc} = 1 - \eta(E_i),$$

$$M_{ij}^{Esc} = \eta(E_j) \quad \text{if } E_j = (E_i + E_k), \tag{49}$$

and $$M_{ij}^{Esc} = 0 \quad \text{if } E_j \neq (E_i + E_k).$$

The resolution matrix M^{Res} is not symmetric, but each row is symmetric with respect to the element of this row which lies along the diagonal of the matrix. The resolution is assumed to follow a Gaussian distribution with standard deviation $\sigma(E)$. The matrix M^{Res} is defined as

$$M_{ij}^{Res} = \frac{1}{\sqrt{2\pi}} \exp\left[-1/2\left(\frac{E_i - E_j}{\sigma(E_j)}\right)^2\right] \frac{1}{\sigma(E_j)}. \tag{50}$$

The detector efficiency is described by a diagonal matrix M^{Eff}

$$M_{ii}^{Eff} = 1 - \exp[-0.0188\,\mu_{Kr}(E_i)]$$

and $$M_{ij}^{Eff} = 0 \quad \text{if } i \neq j, \tag{51}$$

for the proportional counter, and by

$$M_{ii}^{Eff} = \epsilon\,(E_i)$$

and $$M_{ij}^{Eff} = 0 \quad \text{if } i \neq j\,, \tag{52}$$

for the scintillation counter. Tests on some scintillation detectors showed that the efficiency was equal to $\epsilon = 0.7$ and was independent of energy.

The relation between the source vector and that for the expected counting-rate spectral function V^E is

$$V^E = M^{Eff}\ M^{Res}\ M^{Esc}\ (M^{Kr})\ M^{Be} \ldots .\ M^{Air} \cdot V^S = M^{total} \cdot V^S\,. \tag{53}$$

For an assumed source spectral function V^S, we compute the expected counting-rate distribution as a function of the channel number i:

$$V_i^E = \begin{bmatrix} V_1^E \\ V_2^E \\ \vdots \\ V_n^E \end{bmatrix} = \begin{bmatrix} V^E(E_1) \\ V_E(E_2) \\ \vdots \\ V^E(E_n) \end{bmatrix} \tag{54}$$

This spectrum is now compared with the experimentally observed spectrum V^O which is the distribution of observed counting rate versus the channel number i:

$$V^O = \begin{bmatrix} V_1^O \\ V_2^O \\ \vdots \\ V_n^O \end{bmatrix} = \begin{bmatrix} V^O(E_1) \\ V^O(E_2) \\ \vdots \\ V^O(E_n) \end{bmatrix} \tag{55}$$

We might also take a different approach and invert the matrices M^{Eff}, M^{Res}, etc., in order to find an expected source vector. A numerical

application of this method was investigated with the help of fast, large-core computers, but the results were disappointing, and the method was dropped. The main reason for this failure seems to be that a larger interval in energy is required for the matrix-inversion analysis. In this study, only 0.5 decade of energy for the scintillation crystal and 0.37 decade for the proportional counter were used.

In order to compare the sets of numbers V^E and V^O, a meaningful quantity must be introduced as a figure of merit. Following Pearson's suggestion (1900), this quantity is defined as the sum of the squares of the differences between the observed set and the expected set of numbers, weighted by the inverse variance of the expected set of numbers,

$$f' = \Sigma_i \frac{\left[V_i^O - V_i^E\right]^2}{< V_i^E >} \quad . \tag{56}$$

In our experiments, the observed spectrum V^O is always found by subtracting a background spectrum S^B from another spectrum S^{B+S}, which is assumed to be the sum of the background spectrum plus that of the X-ray source. The variance of the net observed counting rate in a particular channel i is

$$< V_i^O > = S_i^B + S_i^{B+S} \quad . \tag{57}$$

The "expected" variance $< V_i^E >$ in equation 56 must be derived by a similar procedure in order to be applicable in our data analysis. It is therefore a reasonable approximation to replace $< V_i^E >$ in 56 by $< V_i^O >$, giving

$$f = \Sigma_i \frac{\left[V_i^O - V_i^E\right]^2}{< V_i^O >} . \tag{58}$$

As a next step we determine the probability P that, upon repetition of the experiment, a larger value of f would be encountered. For this purpose one uses a probability distribution function for the number of degrees of freedom N which exists in the problem considered. In particular, for $N \lesssim 30$ the "chi-square distribution" is used:

$$\frac{dP}{dt}(N) = \frac{e^{\frac{t}{2}} \, t^{\frac{N}{2}-1}}{2^{\frac{N}{2}} \, \Gamma\left(\frac{N}{2}\right)} \quad . \tag{59}$$

Pearson's chi-square test then consists of evaluating a normalized least-squares sum according to equation 58 and of computing the probability Q of exceeding this value upon repetition of the experiment:

$$Q(f|N) = \int_f^\infty \frac{dP}{dt}(N)\, dt, \tag{60}$$

where N is again the number of degrees of freedom. This function Q has been extensively tabulated (Abramowitz and Stegun, 1964). An approximation is available as a subroutine in the IBM system/360 Scientific Subroutine Package.

In the practical analysis a given set of data V^O was compared with several "expected" data sets V^E. Each set V^E, for a given spectral function and a particular set of two parameters, was obtained in the manner described above. One parameter, A, described the amplitude; the other, n, stood for the spectral index. The index n could be the exponent in a power-law spectrum or the value of kT for a thermal spectrum. Both parameters were varied until the corresponding value of f (eq. 58) reached an absolute minimum f_0. The corresponding probability Q therefore has the maximum possible value for the

given data set and the functional form fitted to it. The appropriate parameters will be called A_0 and n_0. From the computation of f for varying A and n we obtain two functions,

$$A = A(f,n) \qquad (61)$$

and $n = n(f,A)$.

We must now define the statistical errors of the "best" parameters A_0 and n_0. The mean value of a variable t which follows the chi-square distribution (59) is $t_m = N$. The variance for this distribution is equal to 2N (Abramowitz and Stegun, 1964, see below). We adopt

$$\sigma = \sqrt{2N} \qquad (62)$$

as the "standard deviation" of a chi-square distribution with N degrees of freedom. The equivalent standard deviation in the parameters A and n is then the variation in these parameters that is generated when f_0 is varied by $\sigma = \sqrt{2N}$. This is in contrast with the definition of Gorenstein et al. (1968) in which f_0 is varied by 1, independent of the number of degrees of freedom. In general, the variation will not be symmetric so that two values, e.g., σ_{n1} and σ_{n2}, must be stated. For example, for a fixed $A = A_0$, we have

$$n_0 = n\ (f_0,\ A_0)\ , \qquad (63)$$

and the two values of σ_n are obtained from

$$n_0 + \sigma_n = n\ (f_0 + \sigma\ ,\ A_0)\ . \qquad (64)$$

The function $n(f, A_0)$ is double-valued for $f > f_0$ and single-valued for $f = f_0$. The analogous equations apply to the calculation of σ_A for a fixed $n = n_0$.

This procedure for the determination of σ_A and σ_n is lent support by a comparison with the more familiar situation in which a variable follows a

normal distribution. If the variable of the chi-square distribution is $\sqrt{2t}$ rather than t, then the mean of the distribution is (Abramowitz and Stegun, 1964)

$$\sqrt{2\,N-1}\cdot\left[1+\frac{1}{16\,N\,(N-1)}\right]+\quad O\,(N^{-7/2})\,, \tag{65}$$

and the variance becomes

$$1-\frac{1}{4N}-\frac{1}{8N^2}+O\,(N^{-3})\,. \tag{66}$$

The following table summarizes the mean and variance of the chi-square distributions for two variables.

Variable	Mean	Variance
t	N	2N
$\sqrt{2t}$	$\sqrt{2\,N-1}\left[1+\frac{1}{16N\,(N-1)}\right]+\ldots\ldots$	$1-\frac{1}{4N}-\frac{1}{8N^2}+\ldots\ldots$

For $N \gtrsim 30$ the chi-square distribution as a function of $\sqrt{2\,t}$ resembles a normal distribution of a variable $s=\sqrt{2\,t}$, with unit variance and a mean $s_m=\sqrt{2N-1}$. In particular, for large N we can approximate the integral $Q(t|N)$ under the chi-square distribution by the integral under a unit normal distribution of the variable

$$s'=\sqrt{2\,t}-\sqrt{2\,N-1}\,. \tag{67}$$

Indeed, one-half of the distance in t-space between the points which correspond to $s'=+1$ and $s'=-1$ is equal to $\sqrt{2\,N-1}$, in close agreement with the value $\sigma=\sqrt{2\,N}$, used above.

The reproductive law of the chi-square distribution (Alexander, 1961) states that if x and y are independent values from the chi-square distributions for M and N degrees of freedom, then x + y is distributed according to the

chi-square distribution for M + N degrees of freedom. This theorem can be used to combine independent sets of f-values for certain parameter combinations. For example, the f-values for the proportional and scintillation counter exposure to a source were added for identical parameter sets and compared with the chi-square distribution for the total number of degrees of freedom.

B. Data Analysis Procedure 2

In this section we describe the method of data analysis which was used for all cosmic X-ray source observations.

The observed counting-rate distribution as a function of channel number was grouped into a small number of bins j; for example, 2 bins for the proportional counter and 3 or 4 bins for the scintillation crystal. Each bin combined m channels. With a reasonable first assumption of the source spectrum V^S, we computed V_i^E (equation 54) by the procedure described in section A. Then a reduced vector V_j^E was found by averaging V_i^E over all m channels which make up the larger bin j. Thus the extrapolation factors:

$$F_j = \frac{V_j^S}{V_j^E}, \tag{68}$$

account for the influence of the atmosphere and other absorbing materials and the physical processes within the detector. The factors F_j were used to convert the observed counting rate in the bin j to a photon-flux spectrum at the top of the atmosphere. With a method to be described below, a best fit to these "extrapolated" data points was determined. As has been pointed out by other observers (Stein and Lewin, 1967), the extrapolation factors F_j are relatively

insensitive to the detailed form of the input spectrum because of the approximations made in their calculation.

The result of this procedure was a set of photon-flux values $y'(E_j)$ with their statistical uncertainties $\delta y'(E_j)$. The flux values are averages over energy intervals ΔE_j, centered at E_j. Although the width of the energy intervals was not small in this analysis, its effect on the best-fit spectrum has nevertheless been ignored.

A transformation was applied to the data points in order to be able to fit a straight line to the transformed points $[\,(y_j + \delta y_j),\ x_j\,]$. For a power-law spectrum;

$$\begin{aligned} y_j &= \ln\,[\,y'(E_j)\,]\,, \\ x_j &= \ln\,(E_j)\,, \\ \text{and}\quad \delta y_j &= \frac{\partial y_j}{\partial y'(E_j)}\,\delta y'(E_j) = \frac{\delta y'(E_j)}{y'(E_j)}\,, \end{aligned} \tag{69}$$

where δy_j denotes the statistical error of the transformed photon flux y_j. For a thin-source thermal spectrum;

$$\begin{aligned} y_j &= \ln\,[\,E_j \cdot y'(E_j)\,]\,, \\ x_j &= E_j\,, \\ \text{and}\quad \delta y_j &= \frac{\delta y'(E_j)}{y'(E_j)} \end{aligned} \tag{70}$$

The parameters a and b for the best straight line $y = a + bx$ were calculated by means of a weighted least-squares method discussed by Beacon (1953). The relative weights have been defined with respect to the uncertainty δy_1 in the first point of the spectrum:

$$\sigma^2 = (\delta y_1)^2 = w_2(\delta y_2)^2 = w_3(\delta y_3)^2 = \ldots\ldots = w_m(\delta y_m)^2. \tag{71}$$

The average $\bar{x}$ is equal to

$$\bar{x} = \frac{\Sigma x}{\Sigma w} \quad , \tag{72}$$

where the summation indices have been suppressed for the sake of brevity.

The values a and b for the best straight lines are then given by

$$a = \frac{\Sigma wy \ \Sigma wx^2 - \Sigma wx \ \Sigma wxy}{\Sigma w \ \Sigma w \ (x - \bar{x})^2} \tag{73}$$

and $$b = \frac{\Sigma w \ \Sigma wxy - \Sigma wx \ \Sigma wy}{\Sigma w \ \Sigma w \ (x - \bar{x})^2} \quad .$$

The variances of a and b are

$$(\delta_a)^2 = \frac{\Sigma wx^2 \ \sigma^2}{\Sigma w \Sigma w \ (x - \bar{x})^2} \tag{74}$$

and $$(\delta_b)^2 = \frac{\sigma^2}{\Sigma w \ (x - \bar{x})^2} \quad .$$

CHAPTER VI

RESULTS OF THE OBSERVATIONS

During the present series of eight balloon flights, four of the five cosmic X-ray sources which have been unambiguously measured by other workers at energies above approximately 15 keV have been observed. The fifth source, Cen XR-2, is located in a region of the celestial sphere which was not surveyed in this study.

Two sources, the Crab Nebula (Tau XR-1) and Cyg XR-1, have been observed in this series as well as by several other experimenters. The Crab Nebula has become a calibration standard for X-ray experiments, while the absolute intensity of Cyg XR-1 was reported to be varying in time. Sco X-1 was also observed during one of our experiments, and in a small number of balloon observations by other experimenters; again, the absolute intensity as well as the spectral shape of this source appears to change with time.

We have detected hard X-radiation from a source or source distribution in the vicinity of the galactic center. Two other balloon observations have confirmed these findings, but this source region is not yet clearly resolved at high X-ray energies. Finally, we have conducted three observations of the region near the north galactic pole. The detector response during the first of these observations can be interpreted as being due to a source near the direction of the north galactic pole, but subsequent measurements have failed to detect a significant flux of hard X-radiation from this region of the celestial sphere.

A. The Crab Nebula

1. Experiment 4. Two vertical detectors, designated W and A, were used in Experiment 4 on 27 April 1966. A modulation disk and ring were mounted in front of telescope W; the detector A was not modulated.

Figure 12 shows the counting-rate profile for the scintillation crystal (22 - 60 keV) of detector W. The modulated exposure curves to Cyg XR-1 and to the Crab Nebula are shown in the lower part of the figure. It is evident that the CsI crystal counting rate increased prior to the exposure to the Crab Nebula. Between 1420 UT and 2020 UT, no known X-ray source was within the field of view, and the available information indicates that the floating altitude remained constant at 2.8 g/cm^2, to within 0.2 g/cm^2. Between 1630 UT and 2230 UT, the balloon drifted in geomagnetic latitude from a local vertical cutoff rigidity of about 4.7 GV (Shea et al., 1968) to a rigidity of 3.3 GV. We interpret the change in the background counting rate in the CsI crystal as a geomagnetic latitude effect. Data points for 4.7 and 4.0 GV, together with data points from other experiments at 4.3, 4.8, and 5.3 GV (Figure 10), were used to find a curve of CsI crystal background rate versus the cutoff rigidity (section III J). In the absence of a proven model, a simple straight line through the low-rigidity data points was used to extrapolate the background flux to lower values of the cutoff rigidity. The background flux during the time of exposure to the Crab Nebula was inferred from this extrapolation. The source contribution was obtained as the difference between the observed counting rate and the computed background rate. The resulting net spectrum for exposure of the detector A to the Crab Nebula is shown in Figure 13

together with the best-fitting lines to the data of Peterson et al. (1968), and the summary given by Gould (1967). Although the statistical accuracy of the scintillation crystal points of Figure 13 is relatively poor, the results demonstrate that the background-determination method is, in principle, correct.

The geomagnetic latitude effect for the proportional counter is small and somewhat uncertain over the rigidity range considered here. Without any correction for this effect, a net spectrum was obtained which is also shown in Figure 13.

2. Experiment 11. Experiment 11 had a three-fold purpose: First, a measurement of the Crab Nebula with higher total exposure than in Experiment 4 was desired; second, a calibration of the detectors and the modulation mechanisms was needed in view of the new results concerning hard X-radiation from the vicinity of the galactic center (section VI D, Exp. 10); and finally, upper limits to the X-ray flux from the sun were sought in order to strengthen arguments against the sun as the source of the observed X-radiation in Experiment 10.

Two detectors were flown in Experiment 11 on 15 July 1967. The detector E was vertical at all times and had a modulation ring and disk mounted in front of the telescope. The balloon gondola rotated continuously at the rate of one revolution per 10 minutes. The zenith angle of detector G was programmed so that the telescope axis traversed the Crab Nebula once in every rotation. In an effort to calibrate our Scorpius and Sagittarius measurements on a well-known source, the detectors G and E were flown without any changes in the pulse-height analyzer or the data recording subsystem.

The detector E performed a meridian transit of the Crab Nebula with additional modulation during this experiment. A clear signal was observed by the CsI scintillation crystal (Figure 14), while the observation by the proportional counter had a lower statistical significance. A plot of the observed counting rate in the crystal over the energy interval from 22 to 60 keV followed the predicted exposure curve (center curve in Figure 14) quite well.

The occultation disk and ring of detector E were designed to provide a structured response pattern in the observation of discrete sources. The accuracy with which a source position may be determined by this procedure was tested with the data from this experiment.

During the meridian-transit of a source, the occultation disk and ring produce a certain counting-rate curve, the shape of which depends on the difference in latitude (declination) of the telescope axis and the source. The position of the pattern is determined by the right ascension of the source and the instantaneous longitude of the detector. The observed counting rate $dN/dt(t)$ of the proportional counter, can be folded with the response function $F(t,\alpha,\delta)$ of the detector. The function F at any time t is equal to the effective exposure area of the counter to a source at right ascension α and declination δ. We must now construct a correlation function $R(\alpha, t)$, which has a maximum for the counting-rate profile $dN/dt(t)$ caused by a source at (α,δ), if this profile is identical to that expected from a source at (α,δ). A suitable normalized folded counting rate is

$$R(\alpha,\delta) = \frac{\int_{t_o}^{t_o+\Delta t} \frac{dN}{dt}(t)\ F(t,\alpha,\delta)\ dt}{\int_{t_o}^{t_o+\Delta t} F(t,\alpha,\delta)\ dt} - \frac{\int_{t_o}^{t_o+\Delta t} \frac{dN}{dt}(t)\ dt}{\Delta t} \qquad (75)$$

Using data from the present observation, we scan in declination for sources at a fixed right ascension $\alpha = 5^h31^m$. The folded rate, shown in the upper part of Figure 15, is necessarily symmetrical about the declination of the detector axis (approximately 31°). Two maxima of the curve are seen at declinations $\delta \approx 21.5°$ and $\delta \approx 40.5°$, but because of the known positions of cosmic X-ray sources in this region of the sky, the second peak may be ignored. As a test of the method, an artificial counting-rate pattern for a point source at the position of Tau XR-1 was generated, and the above-mentioned procedure was then applied to this idealized pattern. The resultant curve is shown in the lower part of Figure 15 and indicates close agreement with the correlation function of the observed pattern.

Errors in the determination of the detector exposure area as a function of the zenith angle and the geographical position of the balloon gondola limit the accuracy of this method to approximately ±2° in declination and right ascension. Errors caused by a possible misalignment of the detector axis and the modulation gear are not important in this experiment because of the continuous rotation of the gondola.

The net counting rate due to the Crab Nebula was analyzed with the help of procedures 1 and 2 (chapter V). The results of an extrapolation according to the second method are shown in Figure 16. Diamonds represent the proportional counter data, and double-bar crosses show the scintillation crystal data of

detector E. Single-bar crosses represent the scintillation crystal data of detector G.

The scanning method of the detector G was described in chapter IV. Because of some minor difficulties in the data handling for certain rotations, only 21 rotations with unambiguous azimuth information were used for the analysis. The zenith angle during each of these 21 rotations was such that the detector alternatingly viewed the Crab Nebula and regions of the sky which are void of any known emitters of X-radiation. During certain periods the sun was within the field of view. However, sun exposure and exposure to the Crab Nebula were clearly separated in azimuth angle and were therefore easily distinguished in viewing time.

The data from each rotation were grouped into 10 1-minute bins, each corresponding to an azimuth angle interval of 36°, and superposed so that bins from successive rotations with maximum exposure to the Crab Nebula were added. Then the bins with 18°-54° azimuth angle with respect to the Crab Nebula were added, then the 54°-90° bins, etc. The resulting curves of observed counting rate versus azimuth angle with respect to the X-ray source are given in Figure 17 for the scintillation crystal and in Figure 18 for the proportional counter. In each figure the top two curves (A and B) refer to Experiment 10, and the next 4 curves (C, D, E, and F) are relevant to the Crab Nebula observations of Experiment 11. The exposure to the source was calculated from the instantaneous detector positions; the resulting curves (B, D, and F) are drawn below the counting-rate superpositions (A, C, and E). Crab Nebula data from a group of seven rotations (C) are shown for this experiment in order to allow a

comparison with the seven-rotation exposure to the vicinity of the galactic center (Experiment 10). The full Crab Nebula data set for 21 rotations is represented by curves E in Figures 17 and 18.

The proportional counter results indicate that, although the background level was higher, there was a clear signal in Experiment 10 (curve A in Figure 18) and no significant signal in the present experiment (curves C and E in Figure 18). The absence of a signal is statistically significant, i.e., the observed number of counts in seven rotations within 54° azimuth angle from the direction to the Crab Nebula is approximately 4σ below the value which is expected from an extrapolation of the CsI scintillation crystal spectrum.

Data from the scintillation crystal of detector G were again analyzed according to both procedures 1 and 2. The extrapolated spectrum at the top of the atmosphere is given in Figure 16, together with the results from detector E.

The observed counting-rate distribution is due to one specific source spectrum. However, different methods of data analysis result in different numerical values for the spectral parameters, for the statistical uncertainty, and for the relative probability of a particular spectral shape (chapter II). An intrinsic property of the analysis procedure 2 (section V B) is that the statistical significance is lower than in procedure 1 because of the smaller number of degrees of freedom. Analytic methods of procedure 2 can be used for power-law and exponential fits to the data, in contrast to those of procedure 1, where a figure of merit is used to determine the best fit. On the other hand, the tatistical error for transformed straight-line fits is calculable with standard

procedures, and in the absence of a known method for the determination of the statistical error for chi-square tests, we have used the method described in section V A.

We have analyzed data from three independent detectors: the proportional counter in E and the scintillation crystals in E and G. The f-values for the same parameter combination were added according to the reproductive law of the chi-square distribution. The parameters of the best fits, their statistical uncertainties and relative probabilities (where applicable), are summarized in Table VI. Whenever procedure 1 resulted in equally high values of Q for several combinations of the parameters A and n, then a value of A close to the "best" value for the amplitude A from procedure 2 was adopted. We have tabulated the results for one data set, from the CsI crystal of detector G, and the results for the sum of all three data sets. The table illustrates that the resulting parameters and their statistical uncertainties are relatively stable when two distinctly different analysis procedures are applied.

None of the three model spectra can be recognized as the correct one on the basis of this analysis alone. However, a thermal spectrum with the Gaunt factor for hydrogen-like atoms and with a correction for electron-electron collisions (chapter II), seems to be favored by a few percentage points. The same observation was made by Jacobson (1968) in his analysis of a high-energy measurement of the Crab Nebula. We have come to a similar conclusion in the analysis of our observations of the vicinity of the galactic center (section VI D).

The present measurements and observations by other experimenters at energies between 1 and approximately 500 keV indicate that the spectrum can be

explained by a single power-law with an index $n \approx 2.0$. In particular, a recent rocket observation of the spectrum of the Crab Nebula between 2 and 20 keV by Boldt et al. (1968b) resulted in a spectral index $n = 1.93 \pm 0.05$. The fact that the Crab Nebula spectrum between 2 and 60 keV is consistent with a power-law of index $n = 1.93$ appears to rule out a two-component thermal model as proposed by Sartori and Morrison (1967a). In a recent study (Holt et al., 1968), it has been shown that the expected line emission from such a thermal source should be evident. Data from the above-mentioned rocket experiment were used to exhibit that, at a statistical level exceeding 1σ, there is no evidence of such line emission for any relevant model of elemental abundances. The sum of all available information on X-radiation from the Crab Nebula indicates that the observed power-law spectrum is caused by synchrotron radiation.

B. Cyg XR-1

1. Experiment 3. Experiment 3 was launched on 13 Jan. 1966. One X-ray telescope with modulation gear was suspended vertically so that it executed a meridian-transit scan of Cyg XR-1. The observed counting-rate distribution has been folded with the pattern expected from a source at the position of Cyg XR-1 (compare section VI A). The results showed that the most probable source location of the observed X-radiation is indeed consistent with the reported position of Cyg XR-1 (Bowyer et al., 1965; Giacconi et al., 1967a).

The net spectrum of Cyg XR-1 was determined from the proportional and scintillation counter data. The net flux at 25 keV, where the spectra of the two

detectors overlap, was extrapolated to the top of the atmosphere. The resulting primary photon flux is $J(E = 25\ keV) \approx 0.01$ photons/cm^2-sec-keV.

2. Experiment 4. Altitude information was not available during the exposure to Cyg XR-1 in Experiment 4, but the pressure profile prior to 12:30 UT, indicates that floating altitude was reached near the beginning of this period.

The response of the scintillation detector of the modulated telescope W to Cyg XR-1 is shown in Figure 12. The observed counting-rate pattern (upper curve) follows the predicted response (lower curve) quite well. The decrease in the background rate between the end of the exposure to Cyg XR-1 and approximately 1630 UT cannot be accounted for. A reduction of the event rate would be expected to be caused by the change in the geomagnetic latitude which occurred during that period, but the observed decrease is too strong to be explained in this way. Altitude changes may have caused the observed pattern; however, the lack of altitude information precludes confirmation of any explanation of this type.

Data analysis procedure 2 was employed for the evaluation of the Cyg XR-1 data. Because of the lower exposure factor of detector W for the Cygnus observation, the results from this detector have a lower statistical significance. The extrapolated spectrum from detector A is shown in Figure 19. It is apparent that the proportional counter information below 20 keV is not consistent with the remaining points of the extrapolated spectrum, and it has therefore been omitted in the following analysis.

A weighted least-squares fit of a power-law spectrum,

$$J(E) = A \cdot E^{-n} \quad , \tag{76}$$

(J in photons/cm^2-sec-keV, E in keV) yields A = 7.47 and n = 2.0 ± 0.3. The best fit of an exponential spectrum,

$$J(E) = A' \cdot \exp(-E/kT) / E \quad , \tag{77}$$

was obtained for A' = 0.53 and kT = $34.2^{+12.4}_{-7.2}$ keV.

These parameters may be compared with the results of other observers: for example A = 3.58, n = 1.93 ± 0.20 (Peterson et al., 1968, experiment on 13 Sept. 1966); A = 16, n = 2.2 ± 0.8, kT = 35 (Bleeker et al., 1967, experiment on 5 April 1966); n = 1.6 ± 0.2, kT = 60 ± 20 (Clark et al., 1968, experiment on 19 July 1966); and A = 3.4, n = 1.8, kT = 94 (Haymes et al., 1968, experiment on 29 Aug. 1967). Haymes et al. (1968) have observed a steepening of the spectrum of Cyg XR-1 above 140 keV; below this energy a power-law spectrum is consistent with the available observations. Thus, the X-ray source Cyg XR-1 may be of the same type as Tau XR-1.

The intensity of Cyg XR-1 is reported to vary in time (Overbeck and Tananbaum, 1968). While the statistical accuracy of our first observations of Cyg XR-1 is insufficient to make a clear comparison, we can say that the intensity at 30 keV observed in the present experiment (27, April 1966) is consistent with the spectrum measured by Bleeker et al. (1967) on 5 April 1966.

C. Sco X-1

1. Experiment 9. The purpose of Experiment 9 was to measure X-radiation from Sco X-1. The experiment was co[illegible]cted over Mildura,

Australia, on 15 Dec. 1966. The detector E, with modulation disk and ring, was mounted on the balloon gondola so that the telescope axis formed an angle Θ of 20° with the vertical. The gas-jet orientation system was used to align and maintain the horizontal projection of the detector axis at a fixed angle β with respect to the local direction of the horizontal projection of the geomagnetic field lines. According to the information given on aeronautical maps of the region, the angle β was set at +8.7°, i.e., the local magnetic field line is shifted by β with respect to the meridian line, and magnetic north appears to be 8.7° east of geographical north. Subsequent studies of satellite data indicated that β is actually equal to +7.6°, thus producing an error, $\Delta\beta' = 1.1°$, in the magnetometer setting. However, the effective error $\Delta\beta$ at zenith angle Θ is considerably smaller than $\Delta\beta'$:

$$\cos \Delta\beta = \cos^2 \Theta + \sin^2 \Theta \cos \Delta\beta'. \qquad (78)$$

A small compass, which was photographed together with the barograph at intervals of 2.5 minutes during the flight, indicated that the gondola was oriented properly throughout the experiment.

This particular balloon flight had an unusually slow ascent rate with the result that floating altitude was reached after the meridian transit of Sco X-1, and the changing altitude during the exposure to the source consequently made the background subtraction more uncertain than in other experiments. We have used the altitude profiles of other experiments to infer the background counting rate during the last part of the balloon ascent.

Figure 20 shows the difference between the observed counting rate and the assumed background. The histograms represent the net rate for

10-minute intervals without any adjustment for the varying altitude. The relation between the residual atmospheric depth and Universal Time is shown on the scale at the bottom of Figure 20. Data from the CsI crystal (22 - 60 keV) are shown by the top curve, and data from the proportional counter are represented by the second curve. The statistical uncertainty for each 10-minute interval is typically 55 counts/10 min for the CsI crystal data and 30 counts/10 min for the proportional counter data. The continuous line (third curve) represents the exposure area (cm^2) for Sco X-1. It was derived from the instantaneous detector-source configuration under the assumption that the detector axis was in the plane of the meridian under a zenith angle of 20°. This curve is valid for the proportional counter at 25 keV, and the appropriate curves for the scintillation crystal at other energies are similar.

There is apparently a shift of about 15 minutes between the predicted profile and the observed histograms. This difference must be interpreted as an error of approximately 4° in the detector alignment with respect to the magnetometer axis. With this interpretation we can now shift the curve of exposure area by the proper amount and compute the net source spectrum from Sco X-1. Data analysis procedure 2 was used to correct the net counting rate for the detector efficiency, and to extrapolate it to the top of the atmosphere. The correction factors (chapter V) were determined under the assumption of thermal emission from an optically thin gas at $T = 5 \cdot 10^{7}$° K. the resulting energy spectrum is plotted in Figure 21. The proportional counter results are represented by diamonds, and the CsI crystal data are drawn as crosses. It must again be pointed out that the absolute values of the spectrum points

in Figure 21 are somewhat uncertain because of the uncertainty in the instantaneous background flux during the exposure to Sco X-1. The shape of the resulting spectrum, however, as well as the relative positions of proportional and scintillation counter results in the spectrum are more positive.

The broken line in Figure 21 represents the energy flux due to thin-source bremsstrahlung of a gas at $T = 5 \cdot 10^7$ °K. Thermal spectra of this type can explain several of the lower-energy observations of Sco X-1 (Chodil et al., 1965; Grader et al., 1966; Gorenstein et al., 1967; Chodil et al., 1968; and Gorenstein et al., 1968). Figure 21 shows that our measurement is also consistent with a thermal spectrum at energies below approximately 35 keV. At higher energies, the observed flux is definitely above the extrapolation of the low-energy spectrum.

A similar high-energy feature was measured by Peterson and Jacobson (1966b) in a balloon experiment on 18 June 1965. The reported spectrum is drawn schematically in Figure 21. From 20 to approximately 35 keV, the data fit an exponential law corresponding to $T = 5 \cdot 10^7$ °K. Above 35 keV, in particular around 45 keV, the energy flux appears to be significantly higher than the extrapolation of the thermal spectrum would indicate. Our results are in substantial agreement with the observations of Peterson and Jacobson (1966b). Whether this feature is a flat high-energy tail or a single line at approximately 45 keV cannot be decided upon from these two observations. Both spectra are, however, not consistent with power-law spectra, so that we can rule out synchrotron emission from Sco X-1. This statement is supported by the fact

that the optical polarization of Sco X-1 (Hiltner et al., 1967) can be explained as due to the interstellar material alone.

Experimenters at the University of Adelaide also have observed an apparent high-energy tail in the Scorpius spectrum during an experiment which was conducted on 29 Feb. 1968 (Buselli et al., 1968). The best fit to their data is provided by the power-law spectrum:

$$I(E) = 925 \cdot E^{-2.79} , \qquad (79)$$

where I is the energy flux in keV/cm^2-sec-keV and E is measured in keV. This function is drawn in Figure 21 as a dashed-dotted line. The data may also be fitted to a thermal spectrum for $T \approx 1.7 \cdot 10^8$ °K. In either case, the observed high-energy flux is definitely above that corresponding to the $5 \cdot 10^7$ °K thermal spectrum which can be inferred from measurements at lower energies (between 1 and 30 keV). In fact, the average energy fluxes (in keV/cm^2-sec-keV) in the energy interval between 40 and 50 keV were 0.06 as observed by Peterson and Jacobson (1966b); 0.07 in the present experiment; and 0.03 as observed by Buselli et al. (1968). In contrast, the measurement by Lewin et al. (1967) on 13 Feb. 1967 yielded a 1σ-upper limit of 0.011, while the observation by Overbeck and Tananbaum (1968) yielded an upper limit of 0.008 keV/cm^2-sec-keV. The upper limit to the energy flux prior to the X-ray flare on 15 Oct. 1967 was given by Lewin et al. (1968c) as approximately 0.01 keV/cm^2-sec-keV.

2. The stellar accretion model for Sco X-1. Several authors (Shklovsky, 1967; Cameron and Mock, 1967; Prendergast and Burbidge, 1968; and Westphal et al., 1968) have built models for the optical and X-ray emission from Sco X-1.

From energy-balance arguments they show that energy must be supplied continuously, for example by infalling matter through a conversion of gravitational potential energy into kinetic energy.

Shklovsky (1967) has proposed a model for Sco X-1 in which gas streams from the secondary component of a close binary system toward a compact (primary) star. The latter might be a neutron star, a white dwarf, or any other massive star with suitable parameters (Cameron and Mock, 1967; Prendergast and Burbidge, 1968). During the mass accretion of the primary star, gravitational potential energy of the incoming matter is released and converted into kinetic energy. The coronal plasma is thus heated to a high temperature, and thin-source bremsstrahlung can occur. Some of the resultant X-ray emission can leave without significant absorption (the overlaying material is optically thin) while another part may be absorbed in the photosphere and reradiated in a black-body spectrum corresponding to a lower temperature.

In Shklovsky's model, a high-energy tail in the Sco X-1 spectrum, as observed by Peterson and Jacobson (1966b) and in the present experiment, may be explained readily as the thermal emission of a still hotter plasma, e.g., at a temperature of the order of $5 \cdot 10^8$ °K.

The maximum coronal temperature that can be reached through the release of gravitational energy by the infalling gas is given by

$$3/2\ N\,k\,T = G\,M\,\mu/\,R\ , \qquad (80)$$

where the mean molecular weight is $\mu = 2/3$. With the stellar mass M and the radius R measured in solar units, we obtain

$$T = 1.02 \cdot 10^{7} \frac{M}{R} \left(\frac{R_\odot}{M_\odot}\right) \qquad (81)$$

As Cameron and Mock (1967) and Prendergast and Burbidge (1968) have pointed out, temperatures of $T \approx 10^{7} - 10^{8}$ °K will be obtained from binary systems where the normalized value of M/R is between 1 and 10, such as in white dwarfs. For a neutron star, however, $M/R \ (R_\odot/M_\odot) \approx 10^{4}$, and T can be as high as 10^{11} °K. The observation of temperatures of the order of $5 \cdot 10^{8}$ °K would then extend the range of possible values for the normalized ratio M/R of the accreting star.

As we have stated above, no high-energy tail was observed on 13 Feb. 1967 by Lewin et al. (1967). If all the observations are correct, then we must assume that the influx of mass to the primary star decreased between the time of our measurement, 15 Dec. 1966, and the next observation, 13 Feb. 1967. This change over a period of two months must have been sufficient to decrease the flux of high-energy X-radiation by a factor of 6 or more. Between 15 Oct. 1967 and 29 Feb. 1968, the high-energy X-ray flux apparently increased again by a factor of 3 or more. In this connection, it may be interesting to note that the energy flux at 25 keV on 13 Feb. 1967 (Lewin et al., 1967) was approximately one-half of the flux that was measured on 18 June 1965 by Peterson and Jacobson (1966b).

Such fluctuations in the observed spectrum of Sco X-1 are not surprising in view of the fact that an intensity change by a factor of 2 over a period of one month was measured by Overbeck and Tananbaum (1968). Changes in the absolute flux level of low-energy X-radiation as well as in the spectral shape have been reported by other observers (Chodil et al., 1968; Gorenstein et al.,

1968; and Hill et al., 1968). Several observations of fluctuations in the optical spectrum of Sco X-1 have also been reported (Chodil et al., 1968).

3. Bremsstrahlung from an isovelocity plasma. Bless et al. (1968) and Wallerstein (1968) have suggested that Wolf-Rayet and Of stars may be sources of X-radiation.

Wolf-Rayet stars are an interesting type of objects whose line-emission spectra show some features which are also observed in O stars. However, they deviate markedly from typical O spectra in that the He lines are stronger. Some objects, called "WC stars," show C, O and strong He lines, while the "WN stars" show strong N and He lines and weak C and O lines.

UV observations of Wolf-Rayet and Of stars have shown that these objects lose mass with velocities up to 2000 km/sec. Although it is not clear whether these velocities are associated with gas streams in a binary system or with the symmetrical expansion of a hot corona; coronal temperatures of the order of a few $\cdot 10^7$ °K have been inferred. The high temperatures may also be generated through interaction between the outflowing gas and the interstellar medium.

It has been attempted to compare the distribution of X-ray sources with that of associations (O'Dell, 1967), but such a correlation does not account for the absence of X-ray sources in the region $l^{II} = 120° - 260°$ (we exclude the Crab Nebula in this argument). Wolf-Rayet stars show a better correlation since they are very scarce in the above-mentioned interval of galactic longitude; however, a detailed statistical analysis has not been carried out.

Two X-ray sources have been tentatively correlated with Wolf-Rayet stars. The optical spectrum of GX 3+1 (see section VI D 3) is similar to that

of a WC star, while the Wolf-Rayet star γ^2 Vel was recently observed in soft X-radiation (Grader et al. 1968).

Fischel and Stecher (1968) have suggested that the observed X-radiation may be due to bremsstrahlung from an isovelocity plasma which interacts with a stationary medium. The heavier ions have greater kinetic energy and therefore produce more energetic photons during their thermalization. In such a model, the abundance distribution as well as the degree of ionization play a crucial role. For any reasonable abundance model, helium is the main contributor to the spectrum at typically 3 keV while heavier ions at velocities of a few hundred km/sec produce the bulk of the observed radiation at energies around 50 keV.

The mathematical formalism of Fischel and Stecher (1968) was used to find the total X-ray flux emitted during the thermalization of an isovelocity plasma with a universal abundance distribution (Aller, 1961) for the 10 most abundant elements up to iron. Fischel and Stecher (1968) found that this plasma, with degrees of ionization as derived from optical and UV observations of hot stars, provides the best agreement with the spectral shape of Sco X-1 as determined by Grader et al. (1968), and by Buselli et al. (1968), for a velocity of 380 km/sec. On the other hand, we find that an isovelocity plasma at v = 200 km/sec provides good agreement with the data of Gorenstein et al. (1968), Chodil et al. (1968), and the results of the present experiment (Figure 21a). Sample calculations for other model plasmas, for example with enhanced helium and heavier-element abundances, result in spectral shapes which are not consistent with the experimental spectrum shown in Figure 21a.

We have attempted to understand the observed fluctuation in the optical and X-ray spectrum of Sco X-1 within the framework of this model. An increase in the available energy may increase the degree of ionization and therefore increase the intensity of high-energy bremsstrahlung by shifting the spectral contribution of each element to higher energies. Calculations for the model plasma which was discussed above (curve 3 in Figure 21a) show that upon an increase of 2 in the degree of ionization for the more abundant elements from magnesium to iron, the photon flux at 3 keV increases by 14% while the flux at 50 keV increases by a factor of 2.25 (curve 4 in Figure 21a). Such a difference in the photon flux at high X-ray energies is apparent from a comparison of the results of the present experiment with the data of Lewin et al. (1967). We are not aware of any low-energy X-ray measurements which were taken during the times when the two sets of high-energy X-ray observations were carried out. We have, however, plotted in Figure 21a the results of observations made on 11 Oct. 1966 (Gorenstein et al., 1968, curve 2), and on 29 Sept. 1967 (Chodil et al., 1968, curve 1).

The photon flux at optical wavelengths is not affected by the partial change of the state of ionization in the particular model plasma used here, but may increase somewhat if the relative abundances of helium and the heavier elements is increased.

It is apparent that the presently available data are not sufficiently accurate to confirm or rule out the validity of the present model. Complete spectra in the optical, low- and high-energy X-ray region are needed in order to build consistent models for the chemical composition, the state of ionization and the velocity of the streaming plasma.

D. The Vicinity of the Galactic Center

1. Experiment 10. The purpose of Experiment 10 was to scan the vicinity of the galactic center in hard X-radiation. This region of the sky was chosen for balloon observations because several sources of low-energy X-radiation had previously been detected there in rocket experiments.

The experiment was conducted over Australia on 18 Dec. 1966. The orientation system for the detector G, and the modulation disk and ring for detector E were described in the discussion of Experiment 11 (section VI A). The zenith angle of detector G was programmed so that the detector axis passed approximately tangentially through the galactic plane once upon each rotation of the balloon gondola.

Six passes from galactic north as well as a group of six passes from galactic south are drawn schematically in Figure 22. A few relevant sources of low-energy X-radiation are also given there. In the manner described in section VI A 2, the raw counting rate was grouped and superposed into 10 bins of equal azimuth angle with respect to a fixed point in the celestial sphere. This point was assumed to be the X-ray source Sgr XR-1, which was detected by Friedman et al. (1967) ($\alpha = 17^h55^m$, $\delta = -29.2°$). The results of the superpositions for two groups of 6 rotations are shown in Figure 23. Both the passes from the galactic north and south exhibit a minimum in the counting rate for azimuthal angles near 180°. The dominant feature of the superposition of passes from the galactic north was the signal detected from Sco X-1 by the krypton proportional counter. In contrast, the dominant feature of the super-

position of passes from the galactic south was the signal from the vicinity of Sgr XR-1, detected by the scintillation crystal. This is a strong qualitative indication of the relative hardness of the two spectra. In both cases, we derived the positional information from the azimuth angles with respect to the direction to Sgr XR-1.

A total of seven passes from the galactic south was used for the evaluation of the X-ray flux from the vicinity of the source Sgr XR-1. The appropriate data superpositions and a comparison with measurements of the Crab Nebula are presented in Figures 17 and 18 (section VI A 2). Two different procedures (chapter V) were used for the data analysis. The results of procedure 2 are given in Figure 24, in which diamonds represent the proportional counter data, and crosses symbolize the scintillator crystal data. A power-law of index $n = 2.69 \pm 0.92$ (dotted line) provides the best of such a spectrum. The best fit for a bremsstrahlung spectrum from an optically thin, hot plasma is obtained for a temperature corresponding to $kT = 16.0 \, ^{+4.7}_{-3.0}$ keV (solid line in Figure 24). The numerical results of both analysis procedures are summarized in Table VII. The thermal spectrum for $Z = 1$, including electron-electron collisions (chapter II), appears to provide the best overall fit to the data from the vicinity of the galactic center.

2. The sun as source of the observed X-radiation (Experiment 10). It is apparent from Figure 22 that the sun ($\alpha = 17^h41^m$, $\delta = -23° 22'$) was within the field of view during exposure to the vicinity of the galactic center. However, it is believed that the sun's contribution to the observed counting rate was negligible. The following arguments support this belief:

(a) The response of detector E was used to determine the location of the source, or the center of the source distribution, which gave rise to the observed radiation. The shape of the modulated response depends strongly on the difference in declination between the detector axis and the X-ray source. We have therefore computed the folded rates F (α, δ) for a fixed right ascension of $\alpha = 17^h55^m$. A scan in declination with the data from this experiment is shown in the upper part of Figure 25. Counting-rate distributions were generated for hypothetical sources at the positions of Sgr XR-1 and the sun. The folded rates for the expected profiles are given in the lower part of Figure 25 for a source at the position of Sgr XR-1 (solid line), and for one at the location of the sun (broken line). The left peak of the solid line can be ignored because of the absence of reported sources in the vicinity of -39° declination and at this right ascension. Figure 25 indicates that the declination of the source or the center of the source distribution is closer to -29° than to -23°. A single source or a source distribution centered at the position of the sun seems to be ruled out.

(b) At one time during Experiment 11, the detector G had full exposure to the sun. The response in the 22 to 60 keV band deviated from background by less than 1σ during exposure to the sun. This deviation would account for

approximately 10% of the observed response from the vicinity of the galactic center over the same energy interval. Indirect evidence supporting the validity of this correlation is supplied by the fact that the daily average of the 9400 MHz solar radio emission (Nagoya University, 1967), which usually shows strong correlation with long-time changes in the soft X-ray emission, was constant to within 5% on the days on which Experiments 10 and 11 were conducted.

(c) An importance 1-flare (GRP 2160) was reported (ESSA, 1967) towards the end of the one-hour data-collection interval of Experiment 10 which was used in the analysis. No change in the counting-rate pattern followed this flare. The planetary magnetic index, K_p, was 2- during exposure to the vicinity of the galactic center. The experiment was conducted on a geomagnetically quiet day.

3. Discussion of the data from the vicinity of the galactic center. The vicinity of the galactic center has been scanned from rocket altitudes by several experimenters. The most recent publications of four research groups (Bradt et al., 1968a; Gursky et al., 1967; Fisher et al., 1968; and Friedman et al., 1967b), as well as the results of a recent balloon observation by Buselli et al. (1968) have been used in the analysis. Figure 26 shows the relevant reported positions of X-ray sources which emit at photon energies of typically 2 - 6 keV. Except for the thin-slit observations of the ASE group (Gursky et al., 1967), the uncertainty in the source position is not shown in this graph. The broken lines represent the trajectories of the axis of the detector G during the first and the last of the seven rotations which were used in this analysis.

In Figure 26, considerable confusion as to the true positions of X-ray sources exists. The situation is relatively clear, however, at galactic latitudes between $l^{II} = 0°$ and $l^{II} \approx 20°$, where we have adopted the positions of 5 sources as reported by the MIT group (Bradt et al., 1968a). For galactic longitudes between 340° and 360°, three source positions were, perhaps somewhat arbitrarily, selected so that they show maximum correlation with the reported positions. These sources lie on the "position lines" reported by the ASE group and will possibly have to be revised as more reliable observations become available. For source number 2 (Table VIII), we have adopted the coordinates of GX 354-5 (Buselli et al., 1968). Table VIII lists the eight sources thus selected. The source designations of the various experimental groups are given, along with an estimate for the source flux density, J_s^o, in photons/cm^2-sec-keV at a photon energy of $E \approx 4$ keV. For the source GX 3+1, we have adopted the position of an intense ultraviolet object of magnitude V = 13.4 (Blanco et al., 1968a, and Blanco et al., 1968b). The optical spectrum of this star is consistent with a Wolf-Rayet type spectrum (Freeman et al., 1968). (Compare section VI C 3).

We can now attempt to compare the observations reported here with the results from rocket-borne instruments. Because of the relatively large angle of view of our X-ray detectors, direct comparison of the results with the spectra or flux-values for individual sources is not possible.

Let us consider a hypothetical detector which is suitable for low-energy X-ray measurements and has the same angular response as our detector. We can compute the photon flux which this detector would have observed if it had

followed the same trajectory as our detector. Obviously, the hypothetical low-energy detector would have to be located above the atmosphere.

We compute the angles $\phi_{s,i}$ between the source s and the direction of the detector axis during the half-minute interval i for M = 8 sources and N = 56 data accumulation points. With the relative exposure factors $F(\phi_{s,i})$, we determine the flux

$$J_{s,i} = J_s^o \cdot F(\phi_{s,i}), \tag{82}$$

where the estimated source flux density at 4 keV, J_s^o, is taken from Table VIII. The net flux due to each source,

$$J_s = \frac{1}{N} \sum_{i=1}^{N} J_{s,i}, \tag{83}$$

is listed in Table VIII. The total net flux from all sources is then

$$J = \sum_{s=1}^{M} J_s = 0.78 \text{ photons/cm}^2\text{-sec-keV}. \tag{84}$$

This photon flux is shown in Figure 24, together with the results of Experiment 10. A thin-source bremsstrahlung spectrum with kT = 11 keV provides the best fit to the data measured by Lewin et al. (1968b), in a balloon-borne experiment. The appropriate curve is also shown in Figure 24 as a broken line. Experimenters at the University of Adelaide (Buselli et al., 1968) measured the spectra of GX 3+1 and GX 354-5 on 29 Feb. 1968, and their data from GX 3+1 can be fitted either to a power-law spectrum of index 2.0 (dash-dotted line in Figure 24) or to a thermal spectrum with kT = 55 keV. The photon flux of GX 3+1 is lower than that observed in this experiment, for example, by a factor of 2 at 25 keV. The spectrum of GX 354-5 is also lower than that measured here, except for a narrow interval of energy around 20 keV where the flux from GX 354-5 would be sufficient to explain the flux observed

here. Buselli et al. (1968) have not speculated on the spectrum of this source; if the 20 keV-data point is real, then the X-ray spectrum might be almost flat between 2 and 20 keV.

Comparisons between the observed spectra or their line representations in Figure 24 suggest that a solid-angle effect exists in the various measurements. Our detector telescope had the largest opening angle and observed the highest photon flux; the detector of the University of Adelaide group was most strongly collimated and thus observed single-source spectra of lower intensity; the observations of Lewin et al. (1968b) are intermediate in both respects. This seems to support the suggestion that we observed hard X-radiation from several sources in the vicinity of the galactic center having, perhaps, different degrees of spectral hardness. Of course, we cannot rule out the hypothesis that only one source with variable hard X-ray emission was observed. Freeman et al. (1968) have given evidence for the short- and long-term stability of the optical counterpart of GX 3 + 1, which was the most intense X-ray emitter during the survey of the vicinity of the galactic center by Buselli et al. (1968).

If it is assumed that the observed hard X-ray flux is due to the set of sources whose soft X-ray contribution has just been evaluated, then Figure 24 demonstrates that it is not possible to decide between synchrotron radiation and bremsstrahlung as the dominant emission process for the total source spectrum.

The ASE and Lockheed groups have reported apparent temperatures for some sources in the vicinity of the galactic center which emit bremsstrahlung

from an optically thin, hot plasma. The apparent temperatures range from kT = 2.1 keV to kT = 4.3 keV (Gursky et al., 1967) and from kT = 6.0 keV to kT = 13.8 keV (Fisher et al., 1968), for the sources 1, 5, 6, 7 and 8 (Table VIII). A wide spread of apparent temperatures can be expected when the emitting gas has a temperature distribution rather than one definite temperature.

E. The Vicinity of the North Galactic Pole

1. Experiment 1. Experiment 1 was conducted on 6 Dec. 1965 with one vertical X-ray telescope, equipped with a modulation ring and disk. The detector axis scanned a band of the celestial sphere at declinations between 31° and 28° and at right ascensions between 10^h12^m and 18^h26^m, i.e. clearly above the galactic plane. The pulse-height analysis system for the scintillation detector malfunctioned during this flight so that the analysis had to be restricted to data from the proportional counter.

An increase in the counting rate was observed between 1400 and approximately 1500 UT, corresponding to a celestial position in the vicinity of the north galactic pole. Possible altitude changes as the cause for this feature can be ruled out, since the floating altitude was stable at 2.9 g/cm^2 to within less than 0.1 g/cm^2, during the main part of the experiment.

According to radar information, the balloon drifted in a northeastern direction between 1340 and 1410 UT, corresponding to a change in the local geomagnetic rigidity cutoff from 4.95 GV to 4.5 GV (Shea et al., 1968). Before 1340 UT and after approximately 1600 UT, the local geomagnetic rigidity cutoff was approximately 4.9 GV. The shape of the observed counting rate pattern

differs from the background rate pattern as deduced from the change of the local cutoff rigidity. A definite cutoff-dependence of the atmospheric and detector background was established for the scintillation crystal from several experiments. The corresponding data for the proportional counter contradict each other somewhat, and the dependence on the rigidity cutoff is unclear (section III J).

The identification of the actual source position makes use of the particular geometrical features of the X-ray telescope and the modulation disk and ring. This method was tested in Experiment 11 and found to be quite accurate in determining the right ascension and declination of an X-ray source.

The definition of the folded rate R (α, δ) was discussed in section VI A. Figure 27 shows the functions R (α, δ) computed with the counting-rate patterns observed in Experiment 1. The upper part shows the curve R $(\alpha = 13^h 00^m, \delta)$ as a function of declination. The lower section of Figure 27 represents the curves R $(\alpha, \delta = +28°)$ (solid line) and R $(\alpha, \delta = +31°)$ (broken line) as a function of right ascension.

An intrinsic feature of this type of analysis is that the function R (α, δ) for a fixed α is symmetric in declination with respect to the declination of the detector axis. The broad structured peak in the upper part of Figure 27 indicates that the source of the observed radiation is located at a declination of either 26° or 36°. For a point source we would then expect a dip in the correlation function R at the symmetry axis, i.e. at $\delta = 31°$. However, Figure 27 indicates a broad central peak rather than a dip at $\delta = 31°$.

The scan in right ascension yields the curves shown in the lower half of Figure 27. The correlation function for $\delta = +28$ shows a broad central peak at $\alpha = 13^h00^m$. The appropriate curve for $\delta = +31^\circ$ also exhibits a narrow peak at the same right ascension, indicating that some X-radiation may come from this direction of the celestial sphere.

We have previously suggested (Boldt et al., 1966) that X-radiation was observed in Experiment 1 from an extended region centered at a right ascension of approximately 13^h00^m and a declination of approximately 28°. The Coma cluster of galaxies is an extended object at right ascension $\alpha = 12^h56^m \pm 8^m$ and at declination $\delta = +28^\circ \pm 2^\circ$ (Abell, 1965). The direction to the center of the Coma cluster of galaxies is approximately 3° away from the direction to the north galactic pole.

The positional evidence presented above and in Figure 28 allows several interpretations: (a) The observed feature in the counting-rate profile of Experiment 1 is due to an extended source of X-radiation in the vicinity of the north galactic pole. (b) We have observed radiation from a point source with varying intensity of X-ray emission. (c) The observed feature is due to a slowly varying point X-ray source together with a changing background counting rate, due to the variation in the local rigidity cutoff.

The available information is insufficient for a discussion of the third suggestion. The fact that subsequent observations (see below) failed to detect a significant flux of X-radiation from the vicinity of the north galactic pole is relevant to the first two models. It is improbable that a strong flux of X-radiation could have been generated in an extended region of the sky with

dimensions of a few degrees, over a period of time of the order of one year or less (see Table V). This argument would rule out model (a) and leave us with the second interpretation of our observations. However, a correlation of our observations with possible models for the time dependence of the X-ray emission from a point source does not seem to be warranted because of the lack of sufficient statistics for such a detailed hypothesis.

From the proportional counter data during the 30-minute period of maximum exposure to the north galactic pole we determine the net spectrum of events in several energy intervals. Figure 28 shows the observed spectrum for a total exposure of 9000 cm^2-sec; the width of each energy interval is 5.5 keV. An extrapolation to the top of the atmosphere according to the data analysis procedure 2 (chapter V) results in a net photon flux $J(E = 25\ keV) \approx 0.014$ photons/cm^2-sec-keV. This result, together with those of other experiments, will be discussed in section VI E 5.

2. Experiment 6. Experiment 6 was launched on 2 Sept. 1966. Six importance 1-flares (ESSA, 1967) occurred while the balloon floated at a residual atmospheric depth of 2.9 g/cm^2. This experiment used the "rotating" scanning method to examine the vicinity of the north galactic pole. The X-ray telescope was programmed to change its zenith angle continuously so that it scanned the north galactic pole during every rotation.

Figure 29 shows a superposition of epochs phased in azimuth angle relative to the direction to the north galactic pole. The upper curve shows a superposition of the CsI scintillation crystal data from 22 to 60 keV for 30 rotations of the gondola. The center curve represents the proportional counter

data in the energy interval from 12 to 28 keV during the same exposure. The lowest curve is proportional to the exposure to a point source along the direction of the north galactic pole.

The mean counting rate for the half rotations opposite in azimuth to the north galactic pole was used as the background level in the determination of the standard deviation σ. The 3σ level was assumed to be an indication of the limiting signal for exposure to the vicinity of the galactic pole. Figure 30 shows the results of the determination of the 3σ limiting signals for several energy bands in both counters. In each of the 7 energy intervals, the observed rate of events at azimuth angles corresponding to the vicinity of the north galactic pole deviated from the background rate by less than 2σ. The extrapolation to the top of the atmosphere yields an upper limit to the photon flux of $J(E = 25 \text{ keV}) \lesssim 0.0072$ photons/cm^2-sec-keV. This upper limit applies to point sources at celestial positions near the direction to the north galactic pole, for example, to the Coma cluster of galaxies.

3. Experiment 7. Experiment 7 was intended to duplicate Experiment 1. Due to a shift of the Phoswitch threshold an excessively high number of events were accepted as valid scintillation crystal counts. Because of this, the dead-time correction for the proportional counter amounted to 60 to 77% during this observation, in contrast to approximately 15% during most of the other experiments described here, thus reducing the statistical significance of the observations from the proportional counter. The CsI crystal data were not analyzed.

Figure 31 shows the counting-rate profile of the krypton proportional counter as a function of time, including the dead-time correction. Events in

the energy region from 12 to 28 keV are represented by the upper curve. The center curve shows events from a sub-sample of energy for the band 22-28 keV. The lower curve is proportional to the exposure to a point source at the direction of the north galactic pole.

The balloon reached ceiling altitude at approximately 1230 UT. The counting-rate profile was essentially flat from 1300 to 1900 UT. The observed rate was somewhat lower after the meridian transit of the galactic pole, but this feature can be accounted for by a loss of altitude which occurred at that time. The average background before the transit of the galactic pole was used to construct the 3σ lines shown in Figure 31. The total counting rate for the 12-28 keV band shows no statistically significant deviation from the background. The largest deviation for a sub-sample occurs in the 22-28 keV band in which one half-hour interval exhibited a deviation from the background of almost 3σ while the galactic pole was still approximately half an hour away. Since this feature was not followed by further periods of increased counting rate, it must be assumed that it was not the response to a source in the vicinity of the north galactic pole.

During the period from 1600 to 1630 UT, the counting rate could not be determined due to difficulties experienced in the retrieval of data from the magnetic recording tape.

Figure 32 shows the 3σ upper limits for three energy bands. The energy intervals were chosen to be identical to those used in the published analysis of Experiment 1 (Boldt et al., 1966). We assume that the 3σ level determines the upper limit to the photon flux from point sources in the vicinity of the north

galactic pole at the time of maximum exposure. Except for a single energy interval which is centered at 20 keV the upper limits are below the net values found in Experiment 1. The extrapolation to the top of the atmosphere results in a photon flux of $J(E = 25 \text{ keV}) \lesssim 0.005$ photons/cm^2-sec-keV.

Towards the end of this experiment the detector's field of view included the constellation Cygnus. The extraction of a net spectrum for the X-ray source Cyg XR-1 was made difficult by the large dead-time correction and by a change in the background counting rate. However, the resulting spectrum of Cyg XR-1 showed sufficient agreement with the spectra of Experiment 4 and with the results of other observers to lend support to the validity of the upper limits established in this experiment for the vicinity of the galactic pole.

4. Summary of experimental information. In addition to the results of Experiments 1, 6 and 7, upper limits to the photon flux from the vicinity of the north galactic pole have been given by other observers. During a rocket experiment on 25 Nov. 1964, Friedman and Byram (1967a) found that no signal with an intensity as great as 7.4% of that from the Crab Nebula was observed in the 1 - 10A wavelength interval from point objects near the north galactic pole, e.g. at the position of the Coma cluster of galaxies. If the spectra of the objects are assumed to follow power-laws with the same index as that of the Crab Nebula,

$$J(E) \propto E^{-2}, \tag{85}$$

then the extrapolated upper limit to the photon flux at the top of the atmosphere is $J(E = 25 \text{ keV}) \lesssim 9 \cdot 10^{-4}$ photons/cm^2-sec-keV. In an observation on 13 Feb.

1967, Lewin et al. (1968a) placed an upper limit to the flux from the same region of the celestial sphere. From the reported information we deduce that $J(E = 25\ \text{keV}) \lesssim 15 \cdot 10^{-4}$ photons/cm^2-sec-keV.

The available experimental information on the photon flux from the vicinity of the north galactic pole, for example from the direction of the Coma cluster of galaxies, is summarized in Table IX.

5. Discussion. The observation of the Coma cluster as an extended source of X-rays could be relevant to the interpretation of the measured diffuse cosmic X-ray background $dj/d\Omega$. Several models have been proposed for this background; one of them assumes that the observed flux is due to the sum of many unresolved galaxies. If $<J_g>$ is the mean emission from a galaxy, then the observed flux due to all unresolved galaxies up to a radius $R \approx R_{\text{Hubble}}$ can be estimated from

$$\frac{dj}{d\Omega} \approx \frac{n_g <J_g> R}{4\pi} , \qquad (86)$$

where n_g is the mean density of galaxies ($n_g \approx 10^{-75}$ cm^{-3}). When $<J_g>$ is set equal to the observed emission of our galaxy, then the resulting value of $dj/d\Omega$ is about two orders of magnitude lower than the measured diffuse X-ray flux (Oda, 1965; and Gould and Burbidge, 1967). However, the assumption that our galaxy is typical with respect to its X-ray emission is somewhat arbitrary. If we assume that X-radiation from the Coma cluster of galaxies was observed in experiment 1, then we obtain a better estimate for $<J_g>$ since the Coma cluster contains about 1500 galaxies at a mean distance of 90 Mpc (Abell, 1965). Felten et al. (1966b) have, however, pointed out that the resulting diffuse X-ray flux would be too high by a factor of 30 to account for the observed background spectrum.

The fact that subsequent observations failed to detect comparable X-radiation from the Coma cluster of galaxies has somewhat removed this discrepancy, but has not solved the problem. The upper limits of Friedman and Byram (1967a) and Lewin et al. (1968a) reduce the discrepancy factor from 30 to approximately 3. Considering the uncertainty in the number of galaxies in the Coma cluster, the various parameters may actually combine to yield the observed diffuse X-ray flux. In this case the "unresolved galaxies"—model for the cosmic X-ray background is not yet ruled out by the limits on the X-ray emission from galaxies of the Coma cluster. The conclusion would then be that the mean emission per galaxy is approximately two orders of magnitude higher than that of our own galaxy. In this connection it is interesting to note that, according to recent measurements (Bradt et al., 1967), the X-ray luminosity of the radio galaxy M 87 is two to three orders of magnitude higher than that of our galaxy (Friedman et al., 1967b).

In view of the fact that other experiments failed to observe a significant photon flux from the vicinity of the north galactic pole, we may tentatively attribute the observations of 6 December 1965 to a transient phenomenon associated with a discrete object.

No information from optical observations during the time of our first experiment is available. Any unusual activity in the vicinity of the north galactic pole would probably have remained undetected since this region of the celestial sphere was in a very unfavorable position for reliable optical observations.

Four flare stars were observed during 1964 and 1965 in a region in Coma Berenices, approximately 6° away from the direction of the north galactic pole (Haro, 1966). The number of flares that were observed per hour in that region was 0.05. We are not aware of flare obsérvations during the time when Experiment 1 was conducted.

Pencil-beam radio observations of the Coma cluster of galaxies (Bozyan, 1968) have recently resolved a small-diameter source, Coma A, which is centered at $\alpha = 12^h 51.8^m$, $\delta = 27^\circ 53.8'$. The energy spectrum of Coma A has an index of $\Gamma = 0.6$. An extrapolation of the power-law radio spectrum can account for the optical luminosity (Matthews and Sandage, 1963; Schmidt, 1965; Wyndham, 1966) and yields a photon flux of $2.5 \cdot 10^{-4}$ photons/cm^2-sec-keV at E = 25 keV. Table IX shows that this flux is approximately two orders of magnitude below the previously reported value (Boldt et al., 1966) and about one order of magnitude below the upper limits found in other experiments.

It is of interest to discuss the hypothesis that the observed feature in Experiment 1 was due to a supernova explosion in the Coma cluster of galaxies.

The duration of X-ray emission during a supernova outburst has not yet been established. Colgate's hydrodynamic model (Colgate, 1968) suggests a time-span for X-ray emission of the order of 10^{-3} sec. The fluorescence theory of optical emission from a supernova (Sartori and Morrison, 1967b) assumes that the explosion takes place within a few seconds. If the above hypothesis were correct, the observations on 6 Dec. 1965 would indicate a period of at least one hour. The photographic light curve for a type I supernova suggests a time-scale of about 20 days for the main phase.

The absence of a significant flux of soft X-ray emission within about 30 days after a supernova explosion (Bradt et al., 1968b) indicates that an upper limit of about 30 days can be set on the duration of X-ray emission. The nova-like behavior of the low-energy X-ray emission from the variable source Cen XR-2 (Harries et al., 1967; Cooke et al., 1967; and Chodil et al., 1967) indicates an e-folding time of about 30 days.

With the assumption that the Coma cluster contains 1500 galaxies, about 4 supernova explosions per year are expected when a rate of 1 event per 400 years per galaxy is adopted. Considering the uncertainty of the observations, this estimate is supported by the fact that 12 supernovae have been observed in the Coma cluster during a recent 10 year period (Zwicky, 1967). The probability of observing the main phase of a supernova explosion during a one-hour observation is therefore 20% if the main phase lasts 20 days, and is 0.04% if it is assumed to last 1 hour.

We can also estimate the energy output in order to evaluate the plausibility of the supernova hypothesis. We assume a power-law photon spectrum of index 2 and compute the energy flux in the X-ray interval from 1 to 100 keV. If the distance to the source is 90 Mpc, then we arrive at a total X-ray energy output of $q = 8 \cdot 10^{51}$ ergs emitted over a period of 20 days. This is not unreasonably high. In fact, the fluorescence model (Sartori and Morrison, 1967b) requires an output of 10^{52} ergs in the ultraviolet band. If the emission is assumed to last only one hour, however, then we find an output of $q = 2 \cdot 10^{49}$ ergs. The X-ray energy output increases by an order of magnitude if thin-source bremsstrahlung at $T = 5 \cdot 10^{7}$ °K is assumed.

Colgate's model (Colgate, 1968) predicts an X-ray pulse with a total energy output of only $q \approx 5 \cdot 10^{47}$ ergs within a fraction of a second and can therefore not be invoked to explain the observation of experiment 1.

CHAPTER VII

SUMMARY

A series of balloon-borne X-ray experiments was carried out between December 1965 and July 1967. The sensing elements of the X-ray telescope consisted of a Krypton proportional counter and a CsI(Tl) scintillation crystal with an effective energy range from 12 to 60 keV. The full-width angle of the detector aperture at half maximum was approximately 24°. In the course of the balloon observations, a broad band of the celestial sphere about a declination of +30°, the vicinity of the galactic center, and the Constellation Scorpius were surveyed.

A study of the data from several balloon flights showed that there exists a definite relation between the background counting rate and the geomagnetic latitude. After subtracting the contribution from the diffuse cosmic X-ray background, we are left with a counting rate which is largely caused by the atmospheric X- and gamma-ray background. It is assumed that most of this photon flux is a component of the atmospheric electromagnetic cascade and is therefore linked to the flux of charged particles incident at the top of the atmosphere; however, a complete calculation of this process has not been carried out to date. A correct prediction of the geomagnetic-latitude dependence of this flux rate constitutes a stringent test for any model of the production of atmospheric X-radiation.

Two observations of the Crab Nebula (Tau XR-1) and three observations of the X-ray source Cyg XR-1 resulted in net source spectra in substantial

agreement with the results of other experimenters. Our results and the observations of other experimenters at lower and higher energies are consistent with a power-law spectrum of index $n \approx 2.0$ for the photon flux from Tau XR-1. One exposure to Tau XR-1 with high statistical accuracy was used to demonstrate two distinctly different methods of data analysis and to show that the resulting sets of spectral parameters are mutually consistent, although one of the methods is superior because it involves fewer approximations.

The measurement of Cyg XR-1 with the highest statistical significance yields a spectrum that is similar to that of Tau XR-1 in shape and in the absolute flux level. With regard to the reported variability of Cyg XR-1, we find that our results are consistent with the spectrum derived by Bleeker et al. (1967) from an experiment that was conducted three weeks prior to the measurement reported here.

A meridian-transit scan of Sco X-1 was carried out during a balloon experiment over Australia. The data analysis for this flight was somewhat difficult because of the variation of the residual atmospheric depth during the exposure to Sco X-1. At energies between 15 and 35 keV, the resulting source spectrum was consistent with thin-source bremsstrahlung at a temperature of approximately $5 \cdot 10^7$ °K. However, the photon flux at higher energies was found to be distinctly above the extrapolation of the low-energy spectrum. A similar spectrum was observed in June 1965 by Peterson and Jacobson (1966). The comparison with the results of other balloon experiments shows that both the shape of the spectrum and the absolute flux above approximatel y 15 keV vary in

time. The high-energy feature that was observed in this experiment can be understood qualitatively in terms of both Shklovsky's (1967) stellar accretion hypothesis and the bremsstrahlung from an isovelocity plasma as suggested by Fischel and Stecher (1968). Any detailed model of Sco X-1 must take into account the existence of a variable high-energy component.

An observation of the vicinity of the galactic center detected a significant flux of hard X-radiation. The resulting spectrum appears to be somewhat softer than that of the Crab Nebula. Subsequent experiments confirmed our finding, but they cannot be directly compared with our observation because of the difference in the solid angles of the various detector apertures. We conclude from these observations and from a calculation of the expected equivalent flux for rocket-borne measurements that we have observed X-radiation from more than one source in the vicinity of the galactic center, perhaps with different degrees of spectral hardness. Further detailed balloon-borne observations will be required in order to resolve the hard X-radiation from the many sources in the vicinity of the galactic center.

Three observations of the vicinity of the north galactic pole brought contradictory results. An increase in the counting rate during the first experiment was interpreted as the X-ray flux from an extended source in the direction of the Coma cluster of galaxies, which is a few degrees away from the direction of the north galactic pole. However, subsequent observations failed to detect a similar feature and set upper limits to the photon flux from celestial objects near the direction of the north galactic pole, including the Coma cluster of galaxies.

It is concluded that if the observed response was caused by a cosmic source of X-radiation, then the source intensity must have varied in time. The hypothesis that a supernova explosion at the distance of the Coma cluster of galaxies caused the signal detected in the first experiment is shown to lead to an energy output in the X-ray region which is not excessively large for such a phenomenon.

In the present series of experiments, we have measured four of the five cosmic X-ray sources or source regions which have to date been clearly observed from balloons (the fifth source is located in Centaurus, a region which was not scanned). The detector that was used for the measurements was designed for an exploratory survey of the celestial sphere. The telescope aperture had a rather large opening angle so that a considerable counting rate was produced by the atmospheric and cosmic diffuse X-ray background. This contribution amounted to approximately two-thirds of the ceiling counting rate, so that only about one-third of this rate represented the inherent detector background. The major portion of the detector background is caused by Compton interactions of gamma radiation in the detector and the surrounding material. The remaining event rate, a small fraction of the total counting rate, is probably caused by an incomplete rejection of charged particles and other effects. Closing the detector aperture without increasing the inherent background counting rate would have reduced the total event rate at ceiling by a factor of 3 to approximately $13 \cdot 10^{-4}$ counts/cm^2-sec-keV. This is in contrast to the best presently available scintillation crystal detector telescope which has an inherent detector background level of $3 \cdot 10^{-4}$ counts/cm^2-sec-keV (Peterson et al., 1968a) at a

residual atmospheric depth of 3.4 g/cm^2 and a geomagnetic latitude of 40°. The gamma-ray induced inherent background can be reduced by a factor of 2 to 3 if the experiment is conducted near the geomagnetic equator.

It appears to be feasible to build a proportional chamber with the same background event rate ($3 \cdot 10^{-4}$ counts/cm^2-sec-keV), an efficiency of typically 60 percent, and an exposure area of the order of 1000 cm^2. With net exposure times during balloon experiments of approximately 3 hours, it will then be possible to detect hard X-radiation from several other sources which have been observed in rocket-borne experiments, provided the low-energy spectra can be extrapolated to higher energies. The available pointing accuracy for balloon-borne experiments is already sufficient to allow the reduction of the field of view to a value where the resulting counting rate caused by the diffuse atmospheric and cosmic background is comparable to the lowest attainable inherent detector background. The inherent and diffuse-background counting rates of the above-mentioned scintillation detector are equal for a solid angle of the field of view of approximately $2 \cdot 10^{-2}$ ster, which corresponds to a circular aperture with 6° full width opening angle at half maximum. This demonstrates that the total counting rate cannot be significantly reduced by making the aperture angle smaller than about 4°.

It is expected that X-ray astronomy measurements will evolve along two somewhat overlapping lines of development. In the first, one will try to obtain information on the spatial distribution and the types of continuum spectra of X-ray sources and their correlation with optical and radio objects. Surveys of

the celestial sphere with improved sensitivity and precise position determinations are best carried out at low X-ray energies at the top of the atmosphere. Balloon or higher-energy satellite observations with high angular resolution and good pointing accuracy during extended exposure times can then be used to determine the high-energy continuum spectra of these X-ray sources.

In a second line of development, one may attempt to resolve lines in the X-ray spectrum. The most prominent low-energy lines are generated in stellar atmospheres and may expand our knowledge of the physical processes occurring there. However, a unique aspect of X-ray astronomy lies in the fact that some intense emission lines in this energy range can be produced in nuclear processes and could provide first-hand information on energy-releasing mechanisms. For example, the 60 keV line of Am 241 is expected to be generated during the decay of isotopes that were produced via the r-process in supernova explosions. The intensity of this line has been estimated for the case of the Crab Nebula (Jacobson, 1968). The above-mentioned proportional chamber could detect a 3σ-line signal above the continuum in a 5 keV-bin if its energy resolution is 10 percent at 60 keV, and if we assume a 30-hour exposure to the Crab Nebula from the top of the atmosphere. This would require that satellites be pointed accurately for extended periods of time instead of used for sky patrols at X-ray energies. Such a shift in the mode of operation of X-ray satellite experiments would aid both wide-band continuum and line measurements.

Balloon-borne experiments will continue to play an important role in the field of X-ray astronomy. While rocket-borne experiments are restricted both

in exposure time and maximum available detector area, and satellite experiments are limited in weight and availability, balloon observations are more favorable in all of these respects.

The continuing development of new detectors is expected to reduce the inherent detector background and improve the energy resolution. However, for a given detector system, optimum results can be obtained through a detailed study of the behavior of the detector in the radiation environment near the top of the atmosphere. Knowledge of the detector event rate as a function of atmospheric depth, geomagnetic latitude, and energy will reduce systematic errors in the extraction of net source counting rates, particularly for exposures to variable sources. It will also make it possible to use a large fraction of the flight time at ceiling for the exposure to a source or source region.

Variable sources require simultaneous observations over a large energy region. As the recent studies of Sco X-1 have indicated, programs for optical, ultraviolet, and low- and high-energy X-ray measurements must be set up with the emphasis on both line and continuum observations. It is hoped that the resulting data will supply the information necessary for the construction of consistent models for discrete X-ray sources.

APPENDIX A

THE ESCAPE FACTOR

A photon of energy E incident on a detector material can be absorbed through the photoelectric effect. The emitted electron will come from the K shell with probability α_K, from the L shell with probability α_L, etc. If the relative probabilities for K, L_1, M_1, etc. shells or subshells are related to the azimuthal quantum numbers l as $1/l^3$, i.e. (1, $1/2^3$, $1/3^3$, etc.), then

$$\alpha_K = 0.86, \quad \alpha_{L_1} = 0.106, \quad \alpha_{M_1} = 0.031 \text{ , etc.}$$

(Grodstein, 1957; Lay, 1934). The remaining atom can be de-excited via the Auger effect or by fluorescence. The latter occurs with probability $\beta(Z)$ which is a strong function of Z. The fluorescence radiation (in practice only the characteristic K-, L-, etc. radiations with energies E_K, E_L, etc. need to be considered) can escape from the detector; in this case the amount of energy deposited in the detector is equal to $E - E_{K,\ (L\ldots)_i}$ and forms the "escape peak."

The escape factor $\eta(E)$ is defined as the fraction of the absorbed number of photons which escapes in the form of fluorescence photons. For an infinite plane-parallel slab of thickness x_o, and escape of characteristic radiation E_c from both surfaces, we have

$$\eta\,(E,\,x_o) = \frac{\int_o^{x_o} \exp(-\mu(E)x)\,\mu(E)\,\alpha\,\beta}{4\pi \int_o^{x_o} \exp(-\mu(E)x)\,\mu\,(E)\,dx} \cdot \frac{\int_o^{2\pi}\int_o^{1}\left[\exp\left(-\frac{\mu(E)x}{\cos\,\theta}\right) + \exp\left(-\frac{(E_K)(x_o-x)}{\cos\,\theta}\right)\right] d\,\cos\,\theta\; d\,\varphi\; dx}{4\pi \int_o^{x_o} \exp(-\mu(E)x)\,\mu\,(E)\,dx}\,, \tag{87}$$

where we have assumed that the incident photon arrives normal to the entrance surface.

With the definition for the exponential integral (Abramowitz and Stegun, 1964)

$$E_1(y) = \int_1^{\infty} \frac{\exp(-yz)}{z^2}\; dz\,, \tag{88}$$

the escape factor can be re-written as

$$\eta\,(E,\,x_o) = 1/2\,\alpha\beta\,\frac{\int_o^{x_o} \exp(-\mu(E)x)\,[\,E_1(\mu(E_c)x) + E_1(\mu(E_c)(x_o-x)\,]\,dx}{1 - \exp\,(-\mu(E)x_o)}. \tag{89}$$

The equation for escape from the <u>entrance surface only</u> is

$$\eta\,(E,\,x_o) = 1/2\,\alpha\beta\,\frac{\int_o^{x_o} \exp(-\mu(E)x)\;E_1(\mu(E_c)x)\,dx}{1 - \exp(-\mu(E)x_o)}\,. \tag{90}$$

Both equations require numerical evaluation. For a semi-infinite medium, $x_o \to \infty$, equation 87 can be integrated directly:

$$\eta\;(E,\infty) = 1/2\,\alpha\beta\;\left[\,1-\frac{\mu(E_c)}{\mu(E)}\;\ln\,\left(1 + \frac{\mu(E)}{\mu(E_c)}\right)\,\right]\,. \tag{91}$$

We apply these equations to the case of CsI(Tl). Table X shows the characteristic line energies (Blokhin, 1957) and relative intensities

(interpolated and extrapolated from data given by Williams, 1933) for Cs, I, and Kr. Only the K shell is considered in table X.

In order to simplify the calculations, the CsI(Tl) crystal is assumed to emit only one fluorescence line at $E_K = 30$ keV; the mean line energy, weighted with the relative intensities, is 30.5 keV. The K-fluorescence yield is taken to be $\beta_K = 0.88$ (Bergström and Nordling, 1965; Fink et al., 1966). The probability of creating an L-shell vacancy and the fluorescence yield for the L shell ($\beta_L = 0.1$) are considerably smaller than those for the K shell ($\frac{\alpha_L \beta_L}{\alpha_K \beta_K} = 0.014$); this justifies the neglect of L shell fluorescence.

Figure 6 shows $\eta(E, x_o)$ as a function of E for $x_o = 0.1$ g/cm^2, $x_o = 0.4$ g/cm^2 and $x_o \to \infty$. The escape factors for both surfaces are drawn as solid lines (compare Stein and Lewin (1967) for NaI). A broken line represents the function $\eta(E)$ for escape from the entrance surface only for a crystal of thickness $x_o = 0.1$ g/cm^2. The latter type of function for a crystal depth of $x_o = 0.4$ g/cm^2 is almost identical with η for the semi-infinite detector, where both cases obviously result in the same escape factor. Escape from the entrance surface is important since the principle K X-radiation of Cs and I can contribute to the energy region of interest in the proportional counter (section III E).

The curves for escape through one or both surfaces of the CsI crystals which were used in our experiments (2 mm CsI or 0.92 g/cm^2 CsI) are practically identical to the curve for a semi-infinite medium ($x_o \to \infty$). The correction for the finite lateral extent of the crystals is negligible.

APPENDIX B

PRODUCTION OF X-RADIATION NEAR THE TOP OF THE ATMOSPHERE

Figure 10 shows the sum of the detector-generated, plus the atmospheric, X-ray background as a function of the local vertical cutoff rigidity. Most of the events shown here are due to the atmospheric X- and gamma radiation; a small fraction is due to corpuscular radiation and other effects (section III G).

It is tempting to draw a curve showing the "pure atmospheric X-ray background" versus the cutoff rigidity, and to compare it with other particle intensity curves, for example, for the proton, neutral pion and neutron fluxes. However, in the rigidity interval from 4 GV to approximately 5.3 GV the slopes of the appropriate curves for energetic neutrons, protons, and pions are roughly equal to each other and to such a "background X-radiation" curve, so that no definite statement as to the origin of atmospheric X-radiation could be made on the basis of such a correlation alone.

We will now present a short discussion of some mechanisms for the production of atmospheric X-radiation. It is assumed that the bulk of the observed photon flux is caused by the electromagnetic cascade in the atmosphere. Other mechanisms, discussed below, can perhaps account for as much as 20% of the observed X-ray flux at balloon altitudes and at $\Lambda \approx 40^{\circ}$. Gamma-ray emission from thermal-neutron capture in O^{16} and N^{14} is assumed to make a negligible contribution to the atmospheric X-, and gamma-ray flux (Peterson, 1963). Bremsstrahlung from re-entrant electrons has not been considered here because of the lack of relevant experimental information.

Internal or "inverse" bremsstrahlung (Hayakawa and Matsuoka, 1964b; Boldt and Serlemitsos, 1968a), during collisions of primary and secondary cosmic rays with atomic electrons, makes a small contribution to the atmospheric X-radiation. At approximately 30 keV the inverse bremsstrahlung flux at balloon altitudes, $\Lambda \approx 40^{\circ}$, is less than $5 \cdot 10^{-4}$ of the observed atmospheric X-ray flux (Peterson et al., 1967a).

Unless otherwise stated, the spectral flux J will, in this appendix, be measured in particles/m^2-sec-MeV; the differential flux per unit solid angle,

$$N = \frac{dJ}{d\Omega} , \tag{92}$$

will be measured in particles/m^2-sec-ster-MeV, and energies are measured in MeV. The production flux

$$Q = \frac{dN}{dz} = \frac{d^2J}{dz\, d\Omega} \tag{93}$$

has the dimension particles/m^2-sec-ster-MeV-g/cm^2, unless otherwise noted.

I. Compton-Scattered Photons from Primary X-rays

The spectrum of the primary cosmic X-ray background has been measured by several observers (Klarman, 1962; Metzger et al., 1964; Garmire and Kraushaar, 1965; Brini et al., 1965b; Rothenflug et al., 1966; Köhn et al., 1966; Peterson et al., 1967a; Peterson, 1967b; Bleeker et al., 1968) in balloon, rocket, and satellite experiments. Balloon-borne observations in the 10 - 100 keV energy range must be extrapolated to the top of the atmosphere; the resulting spectra fit reasonably well with other observations at lower and higher

energies, where this extrapolation is not necessary (cf. the summary given by Gould, 1967a). Thus, we may assume the spectrum of the primary cosmic X-ray background to be known.

We are interested in the spectrum of secondary photons created through Compton scattering of the primary cosmic X-rays by atmospheric atomic electrons. If we limit ourselves to one interaction into an angle within 1 ster of the forward direction, then the differential production spectrum $Q(E_x, z)$, deriving from a primary spectrum $N(E_x, z)$ is

$$Q(E_x, z) = N_o \frac{Z}{A} \int_{E_x}^{E_{max}(E_x, \Theta_{max})} N(E_x, z) \frac{d\phi}{dE}(E, E_x) dE. \qquad (94)$$

For small-angle scattering and $E \lesssim 100$ keV, the interval $\left[E_x, E_{max}(E_x, \Theta)\right]$ becomes very small, so that we can approximate

$$\begin{aligned} Q(E_x, z) &\approx N_o \frac{Z}{A} N(E_x, z) \int_{E_x}^{E_{max}(E_x, \Theta_{max})} \frac{d\phi}{dE}(E, E_x)\, dE \\ &= N(E_x, z)\, \mu_c(E_x, \Theta_{max}) \quad . \end{aligned} \qquad (95)$$

The differential equation for the depth-dependence of the secondary radiation, s, in a one-dimensional model is

$$\frac{ds}{dz} = Q - (\mu_T - \mu_c)\, s = \mu_c N(z = 0) \exp(-\mu_T z) - (\mu_T - \mu_c)s, \qquad (96)$$

where μ_T is the total (photoelectric and Compton) absorption coefficient. The solution

$$s(z) = N(z = 0) \left[\exp(-(\mu_T - \mu_c)z) - \exp(-\mu_T z)\right] \qquad (97)$$

has a maximum at

$$z_{max} = \frac{1}{\mu_c} \ln \frac{\mu_T}{\mu_T - \mu_c} \quad . \qquad (98)$$

For example, at E = 30 keV; $z_{max} = 3.27$ g/cm^2 we obtain the maximum secondary flux

$$s(z_{max}) = 0.0013 \text{ photons/cm}^2\text{-sec-ster-keV}. \quad (99)$$

This is to be compared with an experimental observation of the atmospheric X-ray background flux at $z = 3.5$ g/cm^2, $\Lambda = 40^\circ$ (Peterson et al., 1967a):

$$N(E = 30 \text{ keV}) \approx 0.01 \text{ photons/cm}^2\text{-sec-ster-keV}. \quad (100)$$

This production mechanism is independent of latitude, provided the primary cosmic X-ray background is isotropic. An upper limit to the anisotropy of the diffuse X-ray background was set by Seward et al. (1967), at approximately 10%.

II. Bremsstrahlung from Precipitating Electrons in the Atmosphere

Energetic electrons can be trapped in the earth's magnetic field. Atmospheric absorption of electrons (Cladis and Dessler, 1961; Walt, 1964) is an important loss mechanism; we are here interested in the bremsstrahlung produced in this process.

Cladis and Dessler (1961) have evaluated the precipitation flux of electrons over the Capetown region. With an experimentally determined pitch-angle and energy distribution of radiation-belt electrons, they determined the electron flux entering the atmosphere over the Capetown anomaly, where the mirror altitude of electrons is very low. We can compute the bremsstrahlung spectrum in a production layer which is assumed to be thin compared to the atmospheric depths at which balloon-borne detectors float. The resulting photon flux which would arrive at a residual depth of 3.5 g/cm^2 over the Capetown anomaly was compared with one-half of the integral flux into 4π which was measured by

Peterson et al. (1967a) at this atmospheric depth and $\Lambda = 40^\circ$. The ratio of these values is 0.02 at 30 keV and has a maximum of 0.034 at approximately 100 keV.

During magnetic disturbances the field lines can be altered so that the mirrow points are lowered deeper into the atmosphere; an increased flux of bremsstrahlung radiation would then be expected. Ghielmetti et al. (1964a), reported the observation of an enhancement of the X-ray intensity at balloon altitudes over the South American anomaly. However, as Hudson et al. (1966), have pointed out, the X-ray intensity observed in this experiment can be explained as being due to the diffuse cosmic X-radiation. Therefore, the existence of X-radiation from precipitating trapped electrons to a degree comparable with the observed atmospheric X-radiation is not confirmed.

III. Bremsstrahlung from Electrons

The electron bremsstrahlung cross-section can be approximated by the function

$$\frac{d\phi}{dE_x}(E_e, E_x) = AE_e^a \cdot E_x^{-b}, \tag{101}$$

where E is the electron energy and E_x is the photon energy. If we assume a power-law spectrum for the electrons,

$$J_e(E_e) = B E_e^{-c}, \tag{102}$$

then the resulting photon spectrum is

$$J_x(E_x) = \int_{E_x}^{\infty} J_e(E) \frac{d\phi}{dE_x}(E, E_x)\, dE$$

$$= \int_{E_x}^{E_{1/2}} J_e(E) \frac{d\phi}{dE_x}(E, E_x)\, dE + \int_{E_{1/2}}^{\infty} J_e(E) \frac{d\phi}{dE_x}(E, E_x)\, dE , \tag{103}$$

where the energy $E_{1/2}$ will be that which makes the two integrals on the right side of the last equation equal to each other. In other words, one-half of the photon flux at a particular energy E_x is due to electrons with $E_e < E_{1/2}$, and one-half is due to electrons with $E_e > E_{1/2}$. The ratio

$$\frac{E_{1/2}}{E_x} = \exp\left(\frac{\ln 2}{c-a-1}\right) , \tag{104}$$

is then a good indication as to which part of the electron spectrum is relevant for the bremsstrahlung flux. The equation holds only for $c-a-1 > 0$.

A study of the bremsstrahlung cross-section as given by Bethe and Ashkin (1953), including screening, shows that for example, for $E_x = 0.04$ MeV and $0.16 \lesssim E_e \lesssim 40$ MeV, the exponent, a, becomes ≈ 0.2. For $c = 1.5$, $E_{1/2} / E_x = 10$, and for $c = 2.5$, $E_{1/2} / E_x = 1.7$. This demonstrates that electrons of energies below a few MeV are of greatest importance in the production of X-radiation, provided the electron spectrum is of the steepness indicated above.

There exist only a few measurements of the atmospheric electron component below 10 MeV; they are summarized in Figure 33. The data points of Brunstein (1967) and of Cline and Brunstein (1966) have been obtained at atmospheric depths of 5.5 and 4 g/cm^2, respectively. The data points of Beedle and Webber (1968) are the result of an extrapolation to 1 g/cm^2. These measurements were made at the latitudes of Minnesota and further north.

The atmospheric electron flux is related to the cosmic-ray flux, and the latitude dependence is assumed to depend roughly on the integral cosmic-ray flux. It is therefore necessary to compute the atmospheric electron spectrum at the latitudes where measurements are available, and to compare the calculations with the experimental results. The spectrum can then be extrapolated to or re-calculated for other latitudes.

The calculation can be divided into four sections:

1. The electron production spectrum
2. The electron equilibrium spectrum
3. Bremsstrahlung of electrons (with the calculated or experimental spectrum)
4. The equilibrium photon spectrum (e.g., at balloon altitudes).

1. <u>The electron production spectrum.</u> Low-energy electrons are produced in the atmosphere by several processes. We will discuss the four most important mechanisms (compare Beedle, 1966).

(a) Compton collisions of primary and secondary photons with atmospheric atomic electrons. For this and for the next two processes we need to know the spectrum of primary and secondary photons as a function of the residual atmospheric depth, d, and the geomagnetic latitude. From 0.05 MeV to approximately 10 MeV we use the measurements of Peterson, et al. (1967a) at $\Lambda = 40^{\circ}$ and a depth $d = 3.5\ g/cm^2$ to define the secondary photon spectrum

$$N(E_X) = 600\ E_X^{-1.75} \tag{105}$$

The cosmic X-ray background between 0.03 and 1 MeV at the top of the atmosphere is assumed to be represented by (Gould, 1967; Bleeker et al., 1968)

$$N(E_x) = 150\ E_x^{-2.5} \tag{106}$$

The electron production spectrum is

$$Q(E_e) = \int_{E_{min}}^{\infty} \frac{d\phi}{dE_e}(E_e, E_x)\ N(E_x)\, dE_x,$$

$$E_{min} = \frac{1}{2}\left[E_e + E_e\sqrt{1 + \frac{2m}{E_e}}\right], \tag{107}$$

where Q has the dimensions particles/m^2-sec-ster-MeV-g/cm^2, and $\frac{d\phi}{dE_e}(E_e, E_x)$ is the cross-section per g of air per unit electron energy for the production of an electron of energy between E_e and $E_e + dE_e$ by an incident photon of energy E_x. The relevant curves for electron production due to the secondary and primary photon spectra are shown in Figure 34 as curves number 2 and 3, respectively. It is apparent that the secondary photons (at 3.5 g/cm^2) are more effective than the primary photons (at 0 g/cm^2). The altitude dependence of the photon spectra and the resulting electron spectra is rather complicated; however, we can make the qualitative statement that the relative contributions of the two components remain the same over the first few g/cm^2 near the top of the atmosphere.

(b) Production of photoelectrons due to the primary and secondary photon spectrum in air. The cross-section for the production of electrons via the photoelectric effect has been given by Evans (1955). We adopt the approximation

$$\begin{aligned} \phi(E_e, E_x) &= 1.9 \cdot 10^{-6}\ E_x^{-3}\ (cm^2/g) \qquad E_x < 0.7\ MeV \\ &= 3.3 \cdot 10^{-6}\ E_x^{-1.5}\ (cm^2/g) \qquad E_x > 0.7\ MeV \end{aligned} \tag{108}$$

With the approximation that a photon of energy E_x produces an electron of energy $E_e = E_x$ we obtain the production spectrum

$$Q(E_e) = \phi\ (E_e,\ E_x)\ N\ (E_x)\ . \tag{109}$$

The results are shown in Figure 34 as curves 6 and 7.

(c) Pair production of electrons and positrons in air. The cross-section for pair production was adopted from Evans (1955)

$$\frac{d\phi}{dE_e}\ (E_e,\ E_x) = 0.0012 \cdot \frac{0.53\ E_x - 0.6}{E_x - 2\ m} \qquad 1.5 \lesssim E_x < 5\ \text{MeV}$$

$$= 0.0012 \quad \frac{\sqrt{E_x}}{E_x - 2\ m} \qquad E_x > 5\ \text{MeV} \tag{110}$$

The resulting electron production spectrum is

$$Q(E_e) = \int_{E_e + 2m}^{\infty} \frac{d\phi}{dE_e}\ (E_e,\ E_x)\ N\ (E_x)\ dE_x \tag{111}$$

The production spectra due to the primary and secondary photon flux are drawn schematically in Figure 34 as the curves 5 and 4, respectively.

(d) Production of electrons by collisions of primary and secondary cosmic rays with atmospheric atoms.

The primary cosmic-ray spectrum was assumed to follow the analytical expression given by Balasubrahmanyan et al., (1967), adjusted to fit the summary spectrum given by Gloeckler and Jokipii, (1967), for measurements near the solar minimum in 1965:

$$N(E_p) = 2 \cdot 10^8\ E_p^{1.5}\ (E_p + 500)^{-4} \tag{112}$$

(N in particles/m -sec-ster-MeV, E_p in MeV).

Measurements of the secondary cosmic ray spectrum have been carried out by Ormes (1967; at 3 g/cm^2, Ft. Churchill, 1965) and by Teegarden (1967; at 4 g/cm^2, Sioux Falls, S. Dak., 1961 and Fairibault, Minn., 1964). In order to simplify the calculation we have approximated the secondary cosmic-ray spectrum with the following function:

$$\begin{aligned} N(E_p) &= 0.65 && E_p < 80 \text{ MeV} \\ N(E_p) &= 52/E_p && 80 \text{ MeV} \leq E_p < 200 \text{ MeV} \\ N(E_p) &= 10400/E_p && 200 \text{ MeV} \leq E_p. \end{aligned} \tag{113}$$

At the geomagnetic latitudes of Palestine, Texas the secondary cosmic ray spectrum was assumed to be half as intense as at the latitudes of Sioux Falls and further north (Teegarden, 1967). The dependence of the secondary proton intensity on atmospheric depth was taken from the measurements of Teegarden (1967).

The proton-electron knock-on cross-section is well known (Evans, 1955; Rossi, 1952):

$$\frac{d\phi_{col}}{dE_e}(E_e, E_p) = 2\pi N \frac{Z}{A} r_e^2 m \frac{1}{E_e^2} \frac{1}{1 - \frac{M}{(E_p + M)^2}} \cdot \tag{114}$$

$$\left[1 - \left\{1 - \left(\frac{M}{E_p + M}\right)^2\right\} \frac{E_e\{2m E_p + (M+m)^2\}}{2m E_p (E_p + 2M)} + \frac{E_e^2}{2(E_p + M)^2}\right]$$

where M is the proton mass and m represents the electron mass. Kinetical considerations show that a minimum proton energy $E_{p,\,min}(E_e)$ is required

to produce an electron of energy E_e:

$$E_{p,\ min}(E_e) = \frac{1}{2} E_e - M + \sqrt{M^2 + \frac{1}{2} E_e m + \frac{1}{4} E_e^2 + \frac{1}{2} E_e \frac{M^2}{m}} \approx \frac{M}{4m} E_e \qquad (115)$$

The production spectra of electrons at different geomagnetic latitudes Λ and atmospheric depths d are obtained from

$$Q(E_e, \Lambda, d) = \frac{\Omega_p}{\Omega_e} \int_{E_1}^{\infty} \frac{d\phi}{dE_e}^{col} (E_e, E_p)\, N(E_p, \Lambda, d)\, dE_p \ , \qquad (116)$$

where Ω_p denotes the effective solid angle of the primary and secondary cosmic rays and Ω_e represents the solid angle into which knock-on electrons are emitted. We have assumed a sharp geomagnetic cutoff at $E_c(\Lambda)$; E_1 is the larger of the two energies $E_c(\Lambda)$ and $E_{p,\ min}(E_e)$. Primary particles heavier than protons were included under the usual assumption (Abraham et al., 1966) that these nuclei behave like "A" nucleons in an interaction, where A is the number of nucleons in the primary particle.

At this point, some comments are in place regarding the relative contribution of secondary cosmic rays and the effect of multiple collisions.

A study of equation 114 shows that the knock-on cross-section for fixed electron energies of typically 0.1 - 1 MeV does not vary significantly between $E_{p,\ min}$ and proton energies of a few GeV. This means that primary cosmic rays are the dominant producers of knock-on electrons. The primary cosmic-ray spectrum is not attenuated significantly within the first 10 g/cm^2 near the top of the atmosphere (the collision length for protons in air is 86 g/cm^2), so that the total production flux of electrons near the top of the atmosphere is, to a first approximation, independent of the atmospheric depth.

The effect of multiple collisions can be evaluated by considering the next step, electron-electron collisions. An estimate of the production spectrum Q' due to electron-electron collisions showed that $Q' \approx 0.4\ Q$ at $E_e = 0.1$ MeV and is less at higher energies.

The east-west effect has not been evaluated, but it is not assumed to change the results significantly.

In Figure 34 we show the calculated production spectrum (curve 1) at an atmospheric depth $d = 1\ g/cm^2$ for a proton kinetic-energy cutoff $E_c = 3600$ MeV, corresponding to the geomagnetic latitude of Palestine, Texas. It is apparent that the cosmic-ray collisions provide the largest contribution to the electron flux at energies below a few MeV. In Figure 34 we have also plotted (curve 8) the electron spectrum which is produced by pion decay at $d = 1\ g/cm^2$ and at a cutoff energy $E_c = 3600$ MeV (Verma, 1966).

2. The electron equilibrium spectrum. We must now calculate the equilibrium spectrum since the range of low-energy electrons is very small compared with the atmospheric depths considered. In a one-dimensional model one solves a transport equation

$$\frac{\partial J}{\partial z}(E, z) = Q(E, z) - J(E, z) \int_0^{E_{max}(E)} \frac{d\phi_{col}}{dE'}(E, E')\, dE' + \int_0^{\infty} J(E + E', Z) \frac{d\phi_{col}}{dE}(E + E', E')\, dE' , \tag{117}$$

and the solution leads to a straggling equation

$$J(E_e, d) = \int_{E_e}^{\infty} dE \int_0^{d} dz\ Q(E, z)\ G(E, z), \tag{118}$$

where the Green's function (Rossi, 1952) is

$$G(E, z) = \frac{1}{\sqrt{2\pi\rho^2 z}} \exp\left[-\frac{(E_e - E_a)^2}{2\rho^2 z}\right]$$

$$E_a = E - k(d - z) \tag{119}$$

$$k(E) = \int_0^E E' \frac{d\phi}{dE}_{col} (E, E')\, dE'$$

$$\rho^2(E) = \int_0^\infty E'^2 \frac{d\phi}{dE}_{col} (E + E', E')\, dE'$$

The resulting equilibrium spectra are shown in Figure 35 for a cutoff energy E_c = 20 MeV (curve 1) and for E_c = 3600 MeV (curve 2). We also give the data points of Cline and Brunstein (1966) and of Brunstein (1967). The straight line (curve 3), at energies between 0.05 MeV and 5 MeV, represents a fit to the measurements of Beedle (1966), in an experiment at Ft. Churchill. There appears to be a discrepancy of about one order of magnitude between the curves 1 and 3 and the measurements of Cline and Brunstein. In the following considerations we will use the latitude dependence as previously calculated and normalize to the measurements of Cline and Brunstein (1966).

3. Bremsstrahlung of electrons. The energy range considered here is between the energy intervals where the non-relativistic or the extreme relativistic limits of the bremsstrahlung cross-section are valid. We have used an approximation (Holt and Cline, 1967b) which assumes the appropriate values in the high- and low-energy limits.

4. The observable X-ray flux. The observable X-ray spectrum was calculated according to the equation

$$J(E_x, \Lambda, d) = 2\pi \int_0^d \int_0^{\Theta_{max}} Q_x(E_x, \Lambda, z) \exp\left[-\mu_{air}(E_x)\frac{(d-z)}{\cos\Theta}\right] F(\Theta) \sin\Theta \, d\Theta \, dz , \quad (120)$$

where $f(\theta)$ represents the detector angular response function. Figure 36 shows the resulting atmospheric photon spectra for $E_c = 400$ MeV and $E_c = 3600$ MeV, using the electron spectrum of Cline and Brunstein (1966) as the correct spectrum at a proton cutoff energy of 400 MeV. We have also shown the result of a measurement of the atmospheric photon spectrum by Peterson et al. (1967a), at $E_c = 3600$ MeV.

It is apparent that there is a difference of more than an order of magnitude between the observed and calculated values of the photon flux at energies above 30 keV. The difference in the slopes of the observed and predicted spectra may actually be more significant as an indication that bremsstrahlung from knock-on and Compton-accelerated electrons in the atmosphere does not account for the observed atmospheric X-radiation.

IV. The Photon Component of the Electromagnetic Cascade

Before considering the electromagnetic cascade itself we will briefly summarize the available information on the angular distribution of atmospheric X- and gamma radiation near the top of the atmosphere.

Above 70 MeV the downward photon flux is approximately twice as intense as the upward flux (Svensson, 1958; Cline, 1961). A "horizon brightening" was

observed (Svensson, 1958), where the horizontal photon flux is approximately 6 times stronger than the downward flux. X-ray observations (Frost et al., 1966; Frost, 1968, private communication) indicate that the upward flux is larger than the downward flux by about 50% at energies of approximately 300 keV. If the contribution of the cosmic diffuse background is subtracted, then the upward flux at approximately 30 keV is still larger than the downward flux by 20 - 30%. The same measurements indicate that a horizon brightening is not observed at X-ray energies; the photon flux at 90° zenith angle is close to that of the upward going photons.

Measurements by Kniffen (1967) showed that the atmospheric gamma spectrum above approximately 60 MeV is comparable to the spectrum which is observed from the decay of neutral pions (Perola and Scarsi, 1966), but appears to be higher in intensity by a factor of 2.

Several authors (Anderson, 1961; Peterson, 1963; Brini et al., 1967) have suggested that the large flux of low-energy photons is in equilibrium with high-energy photons in the electromagnetic cascade. The great abundance of soft photons is explained by the fact that a photon, once it has dropped below the pair threshold, will interact by the Compton process, which scatters photons many times before their energy is significantly reduced.

Figure 37 shows the transition curve for photons of energy E = 1 MeV. This curve was adapted from 1 - 3 MeV measurements (Peterson et al., 1967a; Peterson, 1967b) with an omnidirectional detector and normalized to the 1 MeV-photon flux at d = 3.5 g/cm^2.

The second curve in Figure 37 represents a numerical solution to a one-dimensional transport equation for the photon component of the electromagnetic cascade:

$$\frac{dJ}{dz}(E_x, z) = Q^{\pi} + \int_{E_x}^{\infty} \frac{d\phi}{dE}^{br}(E', E_x)\, J_{el}(E', z)\, dE'$$

$$+ \int_{E_x}^{E_{max}(E_x)} \frac{d\phi}{dE}^{com}(E', E_x)\, J_x(E', z)\, dE' \qquad (121)$$

$$- J(E_x, z) \int_{E_{min}(E_x)}^{E_x} \frac{d\phi}{dE}^{com}(E_x, E')\, dE'$$

The source function for photons from pion decay, Q^{π}, was adapted from the calculations of Perola and Scarsi (1966). The altitude dependence of this function was scaled according to the integral flux of particles with $\beta \geq 0.83$, corresponding to proton kinetic energies above 750 MeV (McDonald and Webber, 1959). In the calculation we have assumed the spectrum of atmospheric electrons to be known as a function of depth z (Beedle and Webber, 1968). The limits $E_{min}(E_x)$ and $E_{max}(E_x)$ are defined by the kinematics of Compton interactions.

Figure 37 shows that a one-dimensional photon transport equation does not reproduce the observed transition curve for 1 MeV photons. The observed anisotropy of X-radiation near the top of the atmosphere indicates that the contribution from cascades at all zenith angles must be considered. Also, a one-dimensional model clearly breaks down at energies of the order of a few MeV and lower.

It is evident that a three-dimensional calculation of the electron and photon components of the electromagnetic cascade will be required.

Alsmiller (1968) has followed electromagnetic cascades due to an isotropic flux of 100 MeV gamma radiation incident at the top of the atmosphere. The shape of the resulting photon spectrum at d = 5 g/cm^2 between 0.01 MeV and a few MeV showed qualitative agreement with the observed spectrum (Chapman et al., 1968). However, a discrepancy was found between the relative intensities of the 511 keV annihilation line in the observed and the predicted photon spectra.

REFERENCES

Abell, G. O., Ann. Rev. Astron. Astrophys., 3, 1 (1965).

Abraham, P. B., Brunstein, K. A., and Cline, T. L., Phys. Rev. 150, 1088 (1966).

Abramowitz, M. and Stegun, I. E., Handbook of Mathematical Functions (National Bureau of Standards, 1964).

Aitken, D. W., IEEE Trans. Nucl. Science NS15, 10 (1968).

Alexander, H. W., Elements of Mathematical Statistics (Wiley, New York, 1961).

Allen, C. W., Astrophysical Quantities (Athlone Press, London, 1963).

Aller, L. H., Handbuch der Physik, S. Flügge, Ed. (Springer Verlag, Berlin, 1958), Vol. 51, p. 324.

Aller, L. H., The Abundance of the Elements (Interscience Publishers, New York, 1961).

Alsmiller, R. G., Working Conference on Upper Atmosphere Radiation and Shielding, Oak Ridge (1968).

Anderson, K. A., Phys. Rev. 123, 1435 (1961).

Balasubrahmanyan, V. K., Boldt, E., and Palmeira, R. A. R., J. Geophys. Res. 72, 27 (1967).

Beacon, R. H., Am. J. Phys. 21, 428 (1953).

Beedle, R. E., A Balloon Measurement of the Intensity of Low Energy Electrons as a Function of Altitude at Fort Churchill, Canada, M. S. Thesis, Univ. of Minnesota (1966).

Beedle, R. E. and Webber, W. R., Can. J. Phys. 46, 1014 (1968).

Bergstrom, I. and Nordling, C., Alpha-, Beta- and Gamma-Ray Spectroscopy, K. Siegbahn, Ed. (North-Holland Publishing Co., Amsterdam, 1965), p. 1523.

Bethe, H. A. and Ashkin, J., Experimental Nuclear Physics, E. Segre, Ed. (John Wiley & Sons, Inc., New York, 1953), Vol. I, p. 166.

Blanco, V., Kunkel, W., Hiltner, W. A., Lyngå, G., Bradt, H., Clark, G., Naranan, S., Rappaport, S., and Spada, G., Ap. J. 152, 1015 (1968a).

Blanco, V., Kunkel, W., and Hiltner, W. A., Ap. J. 152, L137 (1968b).

Bleeker, J. A. M., Burger, J. J., Deerenberg, A. J. M., Scheepmaker, A., Swanenburg, B. N., and Tanaka, Y., Ap. J. 147, 391 (1967).

Bleeker, J. A. M., Burger, J. J., Deerenberg, A. J. M., Scheepmaker, A., Swanenburg, B. N., Tanaka, Y., Hayakawa, S., Makino, F., and Ogawa, H., Can. J. Phys. 46, 461 (1968).

Bless, R. C., Fischel, D., and Stecher, T. P., Ap. J. 151, L117 (1968).

Blokhin, M. A., The Physics of X-rays (State Publishing house of Technical-Theoretical Literature, Moscow, 1957).

Boldt, E., McDonald, F. B., Riegler, G., and Serlemitsos, P., Phys. Rev. Letters 17, 447 (1966).

Boldt, E. and Serlemitsos, P., Suprathermal Proton X-Ray Bremsstrahlung, NASA document X-611-68-385 (1968a).

Boldt, E. A., Desai, U. D., and Holt, S. S., 2-20 keV Spectrum of X-Rays from the Crab Nebula and the Diffuse Background near Galactic Anticenter, NASA document X-611-68-353 (1968b).

Bowyer, S., Byram, E. T., Chubb, T. A., and Friedman, H., Nature 201, 1307 (1964a).

Bowyer, S., Byram, E. T., Chubb, T. A., and Friedman, H., Science 146, 912 (1964b).

Bowyer, S., Byram, E. T., Chubb, T. A., and Friedman, H., Science 147, 394 (1965).

Bozyan, E. P., Ap. J. 152, L155 (1968).

Bradt, H., Mayer, W., Naranan, S., Rappaport, S., and Spada, G., Ap. J. 150, L199 (1967).

Bradt, H., Naranan, S., Rappaport, S., and Spada, G., Ap. J. 152, 1005 (1968a).

Bradt, H. Naranan, S., Rappaport, S., Zwicky, F., Ogelman, H., and Boldt, E., Nature 218, 856 (1968b).

Brini, D., Ciriegi, U., Fuligni, F., Gandolfi, A., and Moretti, E., J. Geophys. Res. 70, 5460 (1965a).

Brini, D., Ciriegi, U., Fuligni, F., Gandolfi, A., and Moretti, E., Nuovo Cimento 38, 130 (1965b).

Brini, D., Ciriegi, U., Fuligni, F., and Moretti, E., J. Geophys. Res. 72, 903 (1967).

Brunstein, K. A., J. Geophys. Res. 72, 5510 (1967).

Burbidge, E. M., Burbidge, G. R., Fowler, W. A., and Hoyle, F., Rev. Mod. Phys. 29, 547 (1957).

Buselli, G., Clancy, M. C., Davison, P. J. N., Edwards, P. J., McCracken, K. G., and Thomas, R. M., Nature 219, 1124 (1968).

Cameron, A. G. W. and Mock, M., Nature 215, 464 (1967).

Chapman, G. T., Macklin, J. H., Gibbons, J. H., and Nutt, R., Bull. Am. Phys. Soc. 13, 695 (1968).

Chodil, G., Jopson, R. C., Mark, H., Seward, F. D., and Swift, C. D., Phys. Rev. Letters 15, 605 (1965).

Chodil, G., Mark, H., Rodrigues, R., Seward, F., Swift, C. D., Hiltner, W. A., Wallerstein, G., and Mannery, E. J., Phys. Rev. Letters 19, 681 (1967).

Chodil, G., Mark, H., Rodrigues, R., Seward, F. D., Swift, C. D., Turiel, I., Hiltner, W. A., Wallerstein, G., and Mannery, E. J., Ap. J. (to be published) (1968).

Cladis, J. B. and Dessler, A. J., J. Geophys. Res. 66, 343 (1961).

Clark, G. W., Phys. Rev. Letters 14, 91 (1965).

Clark, G. W., Lewin, W. H. G., and Smith, W. B., Ap. J. 151, 21 (1968).

Cline, T. L., Phys. Rev. Letters 7, 109 (1961).

Cline, T. L. and Brunstein, K. A., Proposal to Study the Energy Spectra, Time Variations and Anisotropies of Cosmic-Ray, Solar, and Distant Magnetospheric Electrons of Energy 50 keV to 2 MeV with the IMP-H and -J and the IMP-I Satellites, NASA document X-611-66-466 (1966).

Colgate, S. A., Can. J. Phys. 46, 476 (1968).

Cooke, B. A., Pounds, K. A., Stewardson, E. A., and Adams, D. J., Ap. J. 150, L189 (1967).

Curran, S. C. and Wilson, H. W., Alpha-, Beta- and Gamma-Ray Spectroscopy, K. Siegbahn, Ed., p. 303 (North-Holland Publishing Co., Amsterdam, 1965).

Dicke, R. H., Peebles, P. J. E., Roll, P. G., and Wilkinson, D. T., Ap. J. 142, 414 (1965).

Doong, H. and Noordzy, M., The Electronics Brain on Board the X-Ray Telescope Spectrometer Experiment, NASA document X-611-66-70 (1966).

ESSA Institute for Environmental Research. Reports of Solar-Geophysical Data (U. S. Dept. of Commerce, 1966, 1967).

Evans, R. D., The Atomic Nucleus (McGraw-Hill Book Company, Inc., New York, 1955).

Fano, U., Phys. Rev. 72, 26 (1947).

Felten, J. E. and Morrison, P., Phys. Rev. Letters 10, 453 (1963).

Felten, J. E. and Morrison, P., Ap. J. 146, 686 (1966a).

Felten, J. E., Gould, R. J., Stein, W. A., and Woolf, N. J., Ap. J. 146, 955 (1966b).

Fink, R. W., Jopson, R. C., Mark, H., and Swift, C. D., Rev. Mod. Phys. 38, 513 (1966).

Fischel, D. and Stecher, T. P., Ap. J. (to be published) (1968).

Fisher, P. C., Jordan, W. C., Meyerott, A. J., Acton, L. W., and Roethig, D. T., Ap. J. 151, 1 (1968).

Freeman, K. C., Rodgers, A. W., and Lyngå, G., Nature 219, 251 (1968).

Friedman, H. and Byram, E. T., Ap. J. 147, 399 (1967a).

Friedman, H., Byram, E. T., and Chubb, T. A., Science 156, 374 (1967b).

Frost, K. J., Rothe, E. D., and Peterson, L. E., J. Geophys. Res. 71, 4079 (1966).

Garmire, G. and Kraushaar, W. L., Space Sci. Rev. 4, 123 (1965).

Ghielmetti, H. S., Becerra, N., Godel, A. M., Heredia, H., and Roederer, G., Phys. Rev. Letters 12, 388 (1964a).

Ghielmetti, H. S., Becerra, N., Godel, A. M., Heredia, H., Marzulli, L. C. and Roederer, J. G., J. Geophys. Res. 69, 3959 (1964b).

Giacconi, R., Gursky, H., Paolini, F. R., and Rossi, B. R., Phys. Rev. Letters 9, 439 (1962).

Giacconi, R., Gorenstein, P., Gursky, H., and Waters, J. R., Ap. J. 148, L126 (1967a).

Giacconi, R., Gorenstein, P., Gursky, H., Usher, P. D., Waters, J. R., Sandage, A., Osmer, P., and Peach, J. V., Ap. J. 148, L129 (1967b).

Ginzburg, V. L. and Syrovatskii, S. I., The Origin of Cosmic Rays (The Macmillan Company, New York, 1964).

Ginzburg, V. L. and Syrovatskii, S. I., Soviet Phys.-Usp. 7, 696 (1965).

Gloeckler, G. and Jokipii, J. R., Ap. J. 148, L41 (1967).

Gorenstein, P., Giacconi, R., and Gursky, H., Ap. J. 150, L85 (1967).

Gorenstein, P., Gursky, H., and Garmire, G., Ap. J. 153, 885 (1968).

Gould, R. J., Phys. Rev. Letters 15, 511 (1965a).

Gould, R. J., Phys. Rev. Letters 15, 577 (1965b).

Gould, R. J., Am. J. Phys. 35, 376 (1967a).

Gould, R. J. and Burbidge, G. R., Handbuch der Physik, S. Flügge, Ed. (Springer Verlag, Berlin, 1967) Vol. 46-II, p. 265.

Grader, R. J., Hill, R. W., Seward, F. D., and Toor, A., Science 152, 1499 (1966).

Grader, R. J., Hill, R. W., and Seward, F. D., presented at the 127th Meeting of the American Astronomical Society (1968).

Grodstein, G. W., X-Ray Attenuation Coefficients from 10 keV to 100 MeV (National Bureau of Standards, 1957).

Gursky, H., Giacconi, R., Paolini, F. R., and Rossi, B. B., Phys. Rev. Letters 11, 530 (1963).

Gursky, H., Giacconi, R., Gorenstein, P., Waters, J. R., Oda, M., Bradt, H., Garmire, G., and Sreekantan, B. V., Ap. J. 146, 310 (1966).

Gursky, H., Gorenstein, P., and Giacconi, R., Ap. J. 150, L75 (1967).

Haro, G., Nebulae and Interstellar Matter, B. M. Middlehurst and L. H. Aller, Ed., (Univ. of Chicago Press, Chicago, 1968), p. 141.

Hayakawa, S., Okuda, H., Tanaka, Y., and Yamamoto, Y., Suppl. Prog. Theoret. Phys. (Kyoto) 30, 154 (1964a).

Hayakawa, S. and Matsuoka, M., Suppl. Prog. Theoret. Phys. (Kyoto) 30, 204 (1964b).

Hayakawa, S., Matsuoka, M., and Sugimoto, D., Space Sci. Rev. 5, 109 (1966).

Haymes, R. C., Ellis, D. V., Fishman, G. J., Glenn, S. W., and Kurfess, J. D., Ap. J. 151, L125 (1968).

Hill, R. W., Grader, R. J., and Seward, F. W., Ap. J. (to be published). (1968).

Hiltner, W. A., Mook, D. E., Ludden, D. J., and Graham, D., Ap. J. 148, L47 (1967).

Holt, S. S., Calibration Standards for Photon Spectroscopy between 20-200 keV, NASA document X-611-67-433 (1967a).

Holt, S. S., and Cline, T. L., On the Generation of Synchrotron and X-Ray Emission from Electrons with Energy below mc^2 in Solar Flares, NASA document X-611-67-525 (1967b).

Holt, S. S., Boldt, E. A., and Serlemitsos, P., Line Emission from X-Ray Sources, NASA document X-611-68-343 (1968).

Hoyle, F., Phys. Rev. Letters 15, 131 (1965).

Hudson, H. S., Primbsch, J. H., and Anderson, K. A., J. Geophys. Res. 71, 5665 (1966).

Jacobson, A. S., A Search for Gamma-Ray Line Emission from the Crab Nebula, Ph. D. Thesis, Univ. of California (1968).

Johnson, H. M. and Golson, J. G., Ap. J. 153, 307 (1968).

Klarmann, J., Nuovo Cimento 24, 540 (1962).

Kniffen, D. A., A Search for Gamma-Rays from the Crab Nebula Using a Digitized Spark Chamber, Ph. D. Thesis, Cath. Univ. of America (1967).

Köhn, D., Pinkay, K., and Wibberenz, G., Ein Gammaquantenspektrometer für Messungen in der Atmosphäre (Christian-Albrechts-Universität Kiel, 1966).

Kraft, R. P. and Demoulin, M. H., Ap. J. 150, L183 (1967).

Lay, H., Z. Physik 91, 533 (1934).

Lewin, W. H. G., Clark, G. W., and Smith, W. B., Ap. J. 150, L153 (1967).

Lewin, W. H. G., Clark, G. W., and Smith, W. B., Can. J. Phys. 46, 409 (1968a).

Lewin, W. H. G., Clark, G. W., and Smith, W. B., Ap. J. 152, L49 (1968b).

Lewin, W. H. G., Clark, G. W., and Smith, W. B., Ap. J. 152, L55 (1968c).

Manley, O. P., Ap. J. 144, 1253 (1966).

Matthews, T. A. and Sandage, A. R., Ap. J. 138, 30 (1963).

Maxon, M. S. and Corman, E. G., Phys. Rev. 163, 156 (1967).

McDonald, F. B. and Webber, W. R., Phys. Rev. 115, 194 (1959).

Metzger, A. E., Anderson, E. C., Van Dilla, M. A., and Arnold, J. R., Nature 204, 766 (1964).

Morrison, P., Nuovo Cimento 7, 858 (1958).

Nagoya University, Research Institute of Atmospherics, Month. Rept. Solar Radio Emission, Nagoya University, Toyokawa (1967).

Oda, M., Proc. Int. Conf. Cosmic Rays (The Institute of Physics and The Physical Society, London, 1965), p. 68.

O'Dell, C. R., Ap. J. 147, 855 (1967).

Ormes, J., Proton- and Helium-Nuclei Cosmic-Ray Spectra and Modulation between 100 and 2000 MeV/Nucleon, Ph. D. Thesis, Univ. of Minnesota (1967).

Overbeck, J. W. and Tananbaum, H. D., Ap. J. 153, 899 (1968).

Pearson, K., Phil. Mag. 50, 157 (1900).

Penzias, A. A. and Wilson, R. W., Ap. J. 146, 666 (1966).

Perola, G. C. and Scarsi, L., Nuovo Cimento 46, 718 (1966).

Peterson, L. E., J. Geophys. Res. 68, 979 (1963).

Peterson, L. E., Jacobson, A. S., and Pelling, R. M., Phys. Rev. Letters 16, 142 (1966a).

Peterson, L. E. and Jacobson, A. S., Ap. J. 145, 962 (1966b).

Peterson, L. E., Jerde, R. L., and Jacobson, A. S., AIAA Journal 5, 1921 (1967a).

Peterson, L. E., Gamma-Ray Production By Cosmic Rays Observed on OSO-1 (Univ. of California, San Diego, 1967b).

Peterson, L. E., Jacobson, A. S., Pelling, R. M. and Schwartz, D. A., Can. J. Phys. 46, 437 (1968).

Prendergast, K. H. and Burbidge, G. R., Ap. J. 151, L83 (1968).

Rossi, B., High-Energy Particles (Prentice-Hall, Inc., Englewood Cliffs, N. J., 1952).

Rothenflug, R., Rocchia, R., and Koch, L., Proc. Int. Conf. Cosmic Rays (The Institute of Physics and The Physical Society, London, 1965), p. 446.

Sandage, A. R., Osmer, P., Giacconi, R., Gorenstein, P., Gursky, H., Waters, J., Bradt, H., Garmire, G., Sreekantan, B. V., Oda, M., Osawa, K., and Jugaku, J., Ap. J. 146, 316 (1966).

Sartori, L. and Morrison, P., Ap. J. 150, 385 (1967a).

Sartori, L. and Morrison, P., presented at the Conference on Supernovas, held at NASA/Goddard Institute of Space Studies, New York (1967b).

Schmidt, M., Ap. J. 141, 1 (1965).

Seward, F., Chodil, G., Mark, H., Swift, C., and Toor, A., Ap. J. 150, 845 (1967).

Shea, M. A., Smart, D. F., and McCall, J. R., Can. J. Phys. 46, 1098 (1968).

Shklovsky, I. S., Doklady Akad. Nauk USSR 94, 1020 (1954).

Shklovsky, I. S., Ap. J. 148, L1 (1967).

Stein, J. A. and Lewin, W. H. G., J. Geophys. Res. 72, 383 (1967).

Svensson, G., Arkiv f. Fysik 13, 347 (1958).

Teegarden, B. L., A Study of Low Energy Galactic Cosmic Rays from 1961 to 1965, Ph. D. Thesis, Univ. of Maryland (1967).

Tucker, W., Ap. J. 148, 745 (1967).

Verma, S. D., A Calculation of the Flux and Energy Spectrum of Secondary Electrons at High Altitudes in the Atmosphere (University of Chicago, EFINS 66-44, 1966).

Wallerstein, C. R., Ap. J. 151, L121 (1968).

Walt, M., J. Geophys. Res. 69, 3947 (1964).

Webber, W. R., X-Ray Astronomy - 1968 Vintage (Univ. of Adelaide, 1968).

Westphal, J. A., Sandage, A., and Kristian, J., Ap. J. 154, 139 (1968).

Wharton, C. B., Plasma Physics, J. E. Drummond, Ed. (McGraw-Hill Co., New York, N. Y., 1961).

Williams, J. H., Phys. Rev. 44, 146 (1933).

Wyndham, J. D., Ap. J. 144, 459 (1966).

Zwicky, F., presented at the Conference on Supernovas, held at NASA/Goddard Institute for Space Studies, New York, 1967.

TABLE I. Line energies for radioactive sources. The line energies and relative intensities have been given by Holt (1967a).

Source	$T_{1/2}$	Energy (keV)	Relative line intensity	Effective energy Kr (keV)	Effective energy CsI (keV)	Resolution spreading Kr (keV)	Resolution spreading CsI (keV)
Co-57	267d.	14.4					
Cd-109	470d.	22.2	1.0	22.41	22.38	0.26	
		25.0	0.1				
		87.5	0.048				
Sn-119	250d.	24.0	1.0	24.66	24.61	0.3	0.3
		25.3	0.82				
		28.5	0.1				
Ba-133	7.2y.	30.6	0.12	31.45	31.44	0.8	0.6
		31.0	0.70				
		35.0	0.17				
		35.8	0.05				
		81.0	0.55				
Eu-155	1.81y.	39.5	0.08	43.0	42.85		1.2
		42.3	0.12				
		43.9	0.26				
		45.0	0.026				
		48.7	0.074				
		50.0	0.017				
		86.5	1.0				
Au-195	192d.	65.1	0.20	66.5	67.7		1.7
		66.8	0.55				
		75.7	0.20				
		77.9	0.05				
Bi-207	304d.	72.8	0.38	74.5	75.85		1.9
		75.0	1.0				
		84.9	0.35				
		87.3	0.09				

TABLE II. Pulse-height analysis, logical requirements and data recording scheme.

Mode	Function	Criteria	Recorded information
0	CsI analysis	B (20 keV ≤ E ≤ 100 keV) $\bar{A}$ (no E > 10 keV)	PHA of B in 64 channels indication of C threshold fired (4 levels)
1	Kr analysis	A (10 keV ≤ E ≤ 30 keV) $\bar{B}$ (no E > 20 keV) $\bar{C}$ (no E > 10 keV)	PHA of A in 64 channels
2	A and B bitrate		scaled number of A events in preceding 5 sec interval in 64 channels scaled number of B events in preceding 5 sec interval in 64 channels
3	B and C overload	B (E > 100 keV) $\bar{C}$ (no E > 10 keV)	number of these events during 100 msec in 64 channels
		C (E > 100 keV)	number of these events during 100 msec in 64 channels
4	CsI analysis	same as mode 0, but with magnetometer indication	
5	Kr analysis	same as mode 1, but with magnetometer indication	
6	A and B bitrate	same as mode 2, but with magnetometer indication	
7	Timekeeping		number of occurrences of mode 7 (every 12 min) in 64 channels

TABLE III. Geometric factor and full-width angle at half-maximum of the effective exposure area.

	Scintill. crystal		Proportional counter	
	with mod.	without mod.	with mod.	without mod.
$E \approx 25$ keV GF (cm^2 ster)	2.1	2.9	3.0	4.0
FWHM		22°		27.6°
$E \approx 75$ keV GF (cm^2 ster)	(3.0)	3.8		
FWHM		27°		

TABLE IV. Extrapolated and observed counting rates at ceiling altitude for the proportional and scintillation counters in several experiments.

Experiment detector	Energy interval (keV)	Atm. depth (g/cm^2)	Cutoff rigidity R (GV)	Observed rate at ceiling altitude R_{obs} $\left(\frac{\text{counts}}{cm^2 \cdot sec \cdot ster}\right)$	Extrapolated rate at ceiling altitude R_{ext} $\left(\frac{\text{counts}}{cm^2 \cdot sec \cdot ster}\right)$	Computed diffuse bgd. contribution R_d $\left(\frac{\text{counts}}{cm^2 \cdot sec \cdot ster}\right)$	Expected rate at ceiling altitude $R_{ext} + R_d$ $\left(\frac{\text{counts}}{cm^2 \cdot sec \cdot ster}\right)$	Ratio of observed to expected rates at ceiling altitude $\frac{R_{obs}}{R_{ext} + R_d}$
4 A—CsI	22-60	2.7	4.0	1.043	0.651	0.284	0.935	1.12
9 E—CsI	22-60	3.3	4.3	1.257	0.899	0.240	1.139	1.10
10 E—CsI	22-60	3.0	4.3	1.243	0.905	0.263	1.168	1.06
10 G—CsI	22-60	3.2	4.3	1.149	0.815	0.247	1.062	1.08
11 G—CsI	22-60	3.45	4.8	0.931	0.668	0.228	0.896	1.04
10 E—Kr	12-28	3.0	4.3	0.410	0.238	0.105	0.343	1.19
10 G—Kr	12-28	3.2	4.3	0.268	0.152	0.092	0.244	1.10

TABLE V. Summary of flight information.

	Experiment							
	1	3	4	6	7	9	10	11
Flight Date	6 Dec. 65	13 Jan. 66	27 Apr. 66	2 Sept. 66	18 Nov. 66	15 Dec. 66	18 Dec. 66	15 Jul. 67
Launch place[1]	HAFB	HAFB	HAFB	HAFB	HAFB	MILDURA	MILDURA	PALEST.
Beginning of ceiling coverage (UT)	1200	1747	1220	1607	1300	0130	0050	1400
End of ceiling coverage (UT)	1910	2213	2230	2508	2230	0338	0413	2004
Residual atmospheric depth (g/cm^2)	2.6-2.8	2.4-2.6	2.7-3.3	2.9	3.0-3.4	3.5-3.1	3.1-3.5	3.2-3.4
Rigidity cutoff (GV)	4.9-4.5	4.8-3.2	4.7-3.4	4.9-5.1	4.8-3.4	4.2-4.4	4.3-4.16	4.7-5.5
Planetary magnetic index K_p	0+ to 1-	1o to 0+	0o to 1-	6 to 9-	3- to 4	5 to 3 +	1+ to 2-	2+ to 4-
Detector symbol	1	1	W	D[3]	D	E	E	E
Scanning method[2]	VERT+MOD	VERT+MOD	VERT+MOD	VERT+MOD	VERT	OR+MOD	VERT+MOD	VERT+MOD
Detector symbol			A	W			G	G
Scanning method[2]			VERT	ROTATING			ROTATING	ROTATING
Solar flares[4]	1840 (1-)	1925 (-B) 2200 (1N)	2116 (-F)	1549 (1-) 1758 (1-) 1825 (1-) 2137 (1-) 2235 (1-) 2335 (1-)	1306 (1-) 1310 (1-) 1905 (1-) 2054 (1-) 2130 (1-) 2201 (1-) 2233 (1-)	NONE	0135 (1-) 0352 (1-)	1531 (-N) 1612 (-N) 1801 (-F)
Celestial object or feature[5]	NGP	Cyg XR-1	Cyg XR-1	NGP	NGP	Sco X-1	Gal. cen.	Tau XR-1
UT of meridian transit	1418	1858	1230	2120	1537	0116	0231	1636
Celestial object			Tau XR-1		Cyg XR-1			
UT of meridian transit			2149		2156			

[1] HAFB = Holloman AFB, Alamogordo, N. M., l = -105.9°, b = +33.0°; MILDURA, Australia, l = +142.1°, b = -34.2°; PALEST. = Palestine, Texas, l = -95.7°, b = 31.7°.

[2] VERT = vertical detector, no modulation. VERT+MOD = vertical detector with modulation disk and ring. OR+MOD = oriented (aligned for due north, fixed zenith angle) with modulation disk and ring. ROTATING = rotating detector with varying zenith angle.

[3] Detector malfunction, not analyzed.

[4] Universal time of maximum phase is shown. The importance of the flare is shown in parenthesis.

[5] NGP = North galactic pole; Gal. cen. = Galactic center.

TABLE VI. Spectral parameters for the Crab Nebula. Results of Experiment 11.

	Detector G, CsI		Sum of all 3 detectors	
	Procedure 1	Procedure 2	Procedure 1	Procedure 2
Powerlaw spectrum*	A = 8.0	A = 7.94	A = 5.5	A = 5.29
$J(E) = A\,E^{-n}$	$n = 1.93^{+0.13}_{-0.09}$	$n = 2.03 \pm 0.34$	$n = 1.88^{+0.17}_{-0.09}$	$n = 1.94 \pm 0.27$
	Q = 0.89		Q = 0.48	
Exponential spectrum*	A = 0.6	A = 0.47	A = 0.6	A = 0.44
$J(E) = A \exp(-E/n)/E$	$n = 50^{+29}_{-18}$	$n = 42.6^{+22.6}_{-10.9}$	$n = 45^{+23}_{-15}$	$n = 43.7^{+18.6}_{-10.0}$
	Q = 0.88		Q = 0.50	
Full thermal spectrum*	A = 0.006		A = 0.006	
$J(E) = \frac{A}{\sqrt{n}} \exp\left(-\frac{E}{2n}\right) K_o\left(\frac{E}{2n}\right) \left[1 + \left(2+0.64\frac{E}{n}\right)\frac{n}{511}\right]\frac{1}{E}$	$n = 73^{+23.5}_{-21}$		$n = 65^{+19}_{-18}$	
	Q = 0.89		Q = 0.58	

*J in units of photons/cm^2-sec-keV, energies in keV.

TABLE VII. Spectral parameters for the vicinity of the galactic center. Results of Experiment 10, detector G.

	Procedure 1	Procedure 2
Power-law spectrum*	A = 85.0	A = 87.0
$J(E) = A\,E^{-n}$	$n = 2.61\ ^{+0.19}_{-0.11}$	$n = 2.60 \pm 0.92$
	Q = 0.11	
Exponential spectrum*	A = 2.4	A = 2.32
$J(E) = A \exp(-E/n)/E$	$n = 15.0\ ^{+6.0}_{-4.0}$	$n = 16.0\ ^{+4.7}_{-3.0}$
	Q = 0.043	
Full thermal spectrum*	A = 0.012	
$J(E) = \frac{A}{\sqrt{n}} \exp\left(-\frac{E}{2n}\right) K_o\left(\frac{E}{2n}\right)$	$n = 40\ ^{+13}_{-11}$	
$\left[1 + \left(2 + 0.64\,\frac{E}{n}\right)\frac{n}{511}\right]\frac{1}{E}$	Q = 0.22	

*J in units of photons/cm^2-sec-keV, energies in keV.

TABLE VIII. X-ray sources in the vicinity of the galactic center.

Source	1	2	3	4	5	6	7	8
Experimenters								
MIT[1]				GX3+1	GX5-1	GX9+1	GX13+1	GX17+2
ASE[2]	GX-10.7	GX-5.6	GX-2.5	GX+2.6	GX+5.2	GX+9.1	GX+13.5	GX+16.7
Lockheed[3]	L6	L9	L12	L14	L17	L18, L19	L20	L21
NRL[4]	ScoXR-2		ScoXR-6	SgrXR-1		SgrXR-3	SgrXR-2	SerXR-2
Adelaide[5]		GX354-5		GX3+1				
Right ascension α	17^h08^m	17^h47^m	17^h44^m	$17^h42.7^m$	$17^h58.6^m$	$17^h59.7^m$	$18^h10.0^m$	$18^h12.7^m$
Declination δ	-37.°	-36.°	-32.°	-26.17°[6]	-25.00°	-20.53°	-17.13°	-13.60°
Estimated photon flux J_s^0 at 4 keV (photons/cm^2-sec-keV)	0.30	0.05	0.11	0.18	0.30	0.25	0.10	0.30
Expected source contribution J_s (photons/cm^2-sec-keV) (Section VI D)	0.108	0.024	0.06	0.108	0.183	0.138	0.047	0.109

[1] Bradt et al. (1968a).
[2] Gursky et al. (1967).
[3] Fisher et al. (1968).
[4] Friedman et al. (1967b).
[5] Buselli et al. (1968).
[6] Position of optical counterpart (Blanco et al., 1968).

TABLE IX. Photon flux from the Coma cluster of galaxies. Balloon-borne measurements at 25 keV, extrapolated to the top of the atmosphere.

Observation date	Photon flux photons/cm^2-sec-keV	Reference
25 Nov. 1964	$<9.4 \cdot 10^{-4}$*	Friedman and Byram (1967a)
6 Dec. 1965	$(140 \pm 42) \cdot 10^{-4}$	Experiment 1 (Boldt et al., 1966)
2 Sept. 1966	$<72 \cdot 10^{-4}$	Experiment 6
18 Nov. 1966	$<50 \cdot 10^{-4}$	Experiment 7
13 Feb. 1967	$<15 \cdot 10^{-4}$	Lewin et al. (1968a)

*extrapolation from lower-energy rocket measurements assuming a power-law of index -2.

TABLE X. Characteristic line energies and relative intensities of Cs, I and Kr.

Material		K_{α_1}	K_{α_2}	K_{β_1}	K_{β_2}	Average
Cs	energy (keV)	30.970	30.623	34.984	35.819	31.72
	relative intensity	100	50	30	8	
I	energy (keV)	28.610	28.315	32.292	33.016	29.297
	relative intensity	100	50	30	7.5	
Kr	energy (keV)	12.648	12.597	14.112	14.313	12.867
	relative intensity	100	50	25	3	

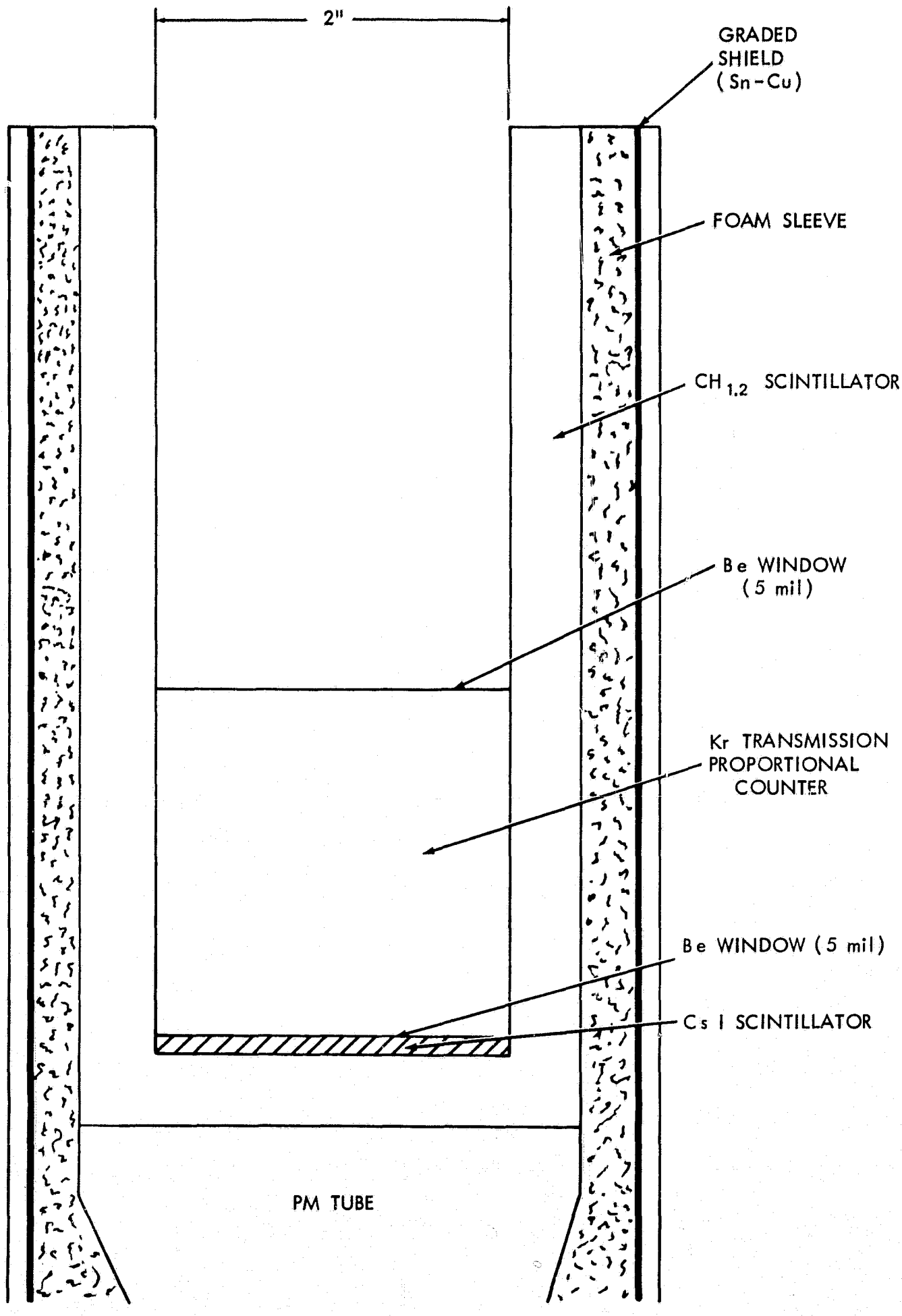

Figure 1— Essential features of the X-ray telescope

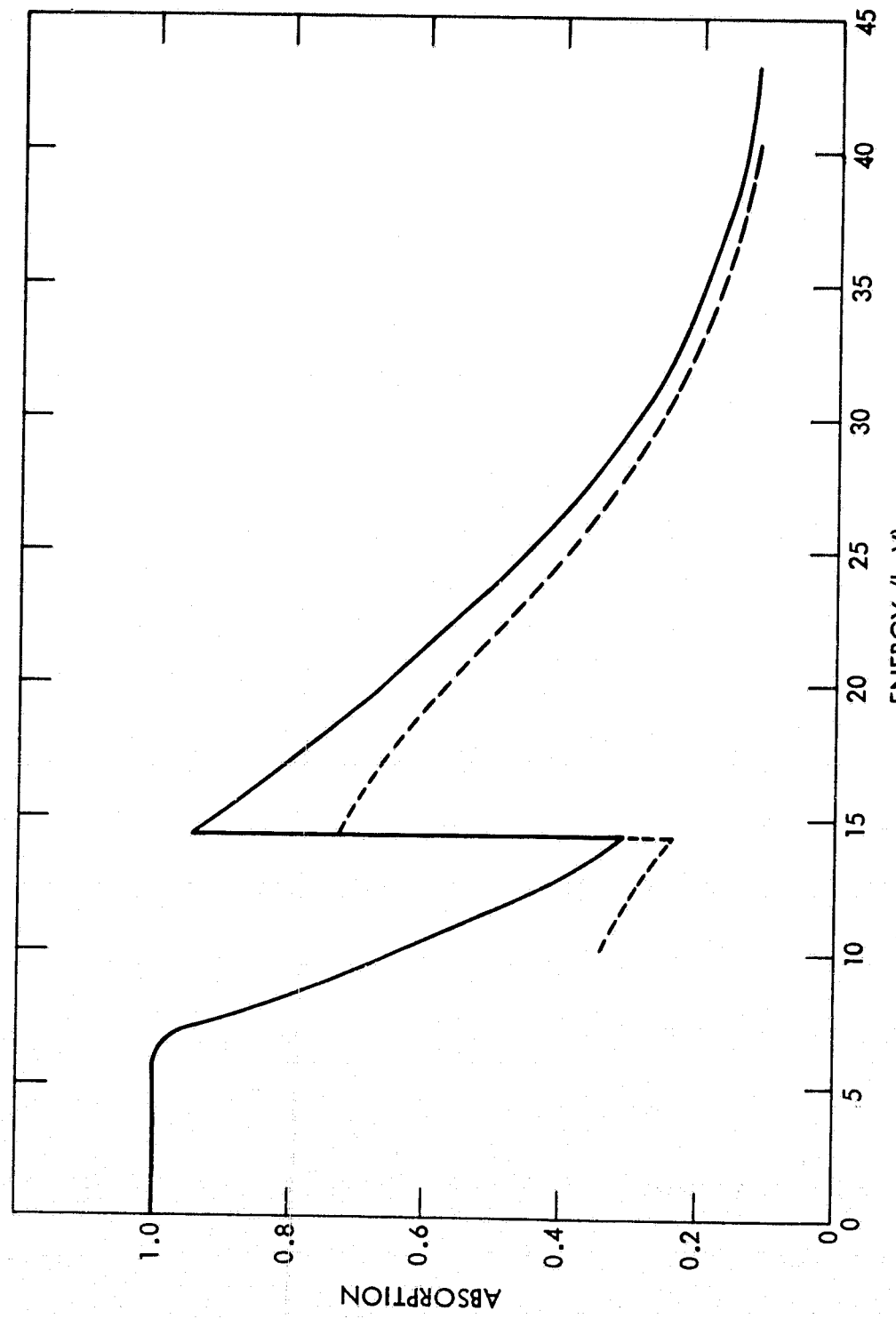

Figure 2—Absorption of the proportional counter and transmission of materials in front of it. Solid line: absorption of 0.0188 g/cm^2 Kr. Broken line: absorption of 0.0188 g/cm^2 Kr and transmission of 0.00254 cm polyester, 0.00381 cm Al, 0.3175 cm Be, and 0.0127 cm Be

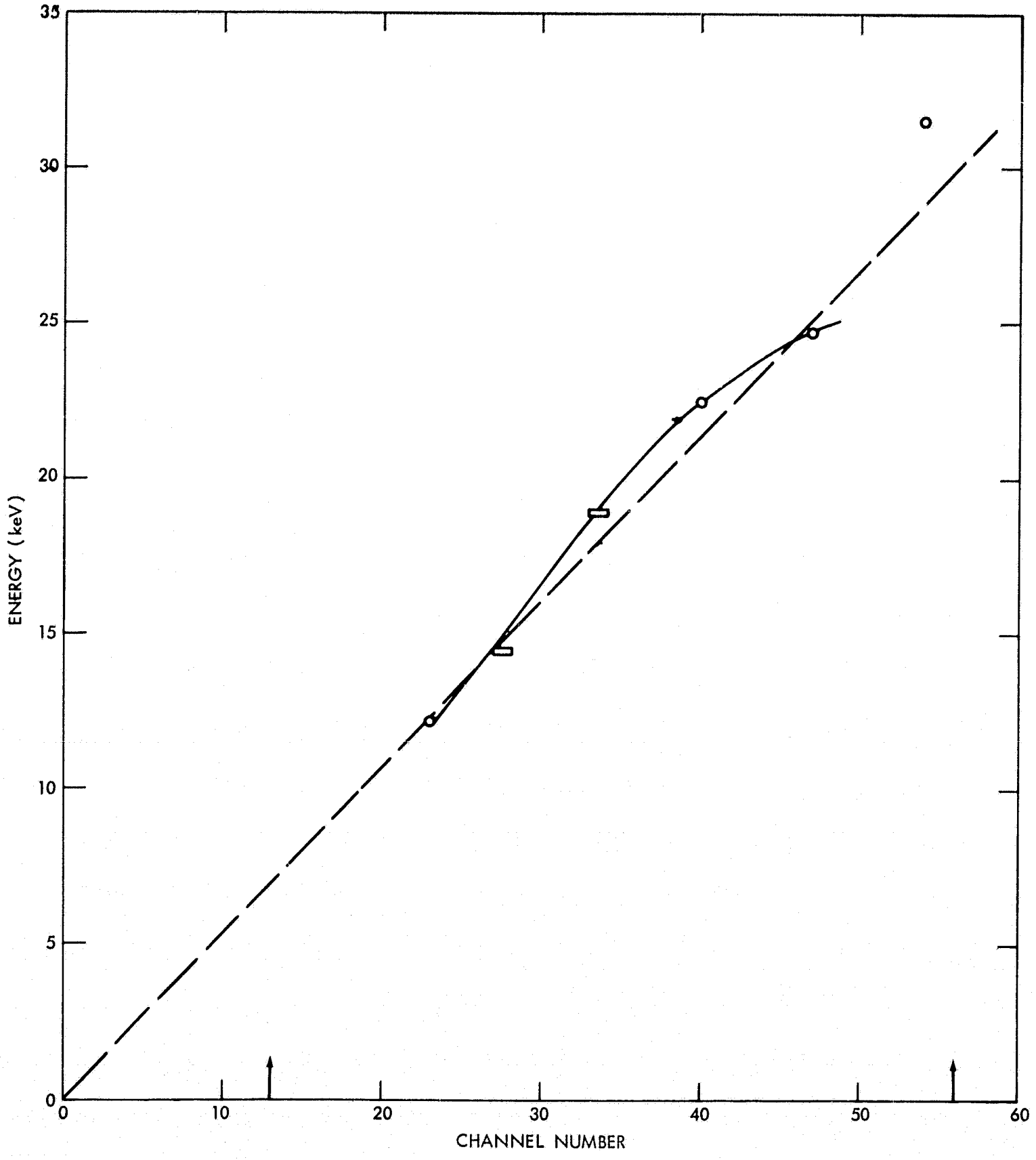

Figure 3— Energy calibration for the proportional counter of detector G. Arrows indicate the lower and upper cutoffs. The solid line connects the calibration points. The broken line represents a linear approximation to the curve.

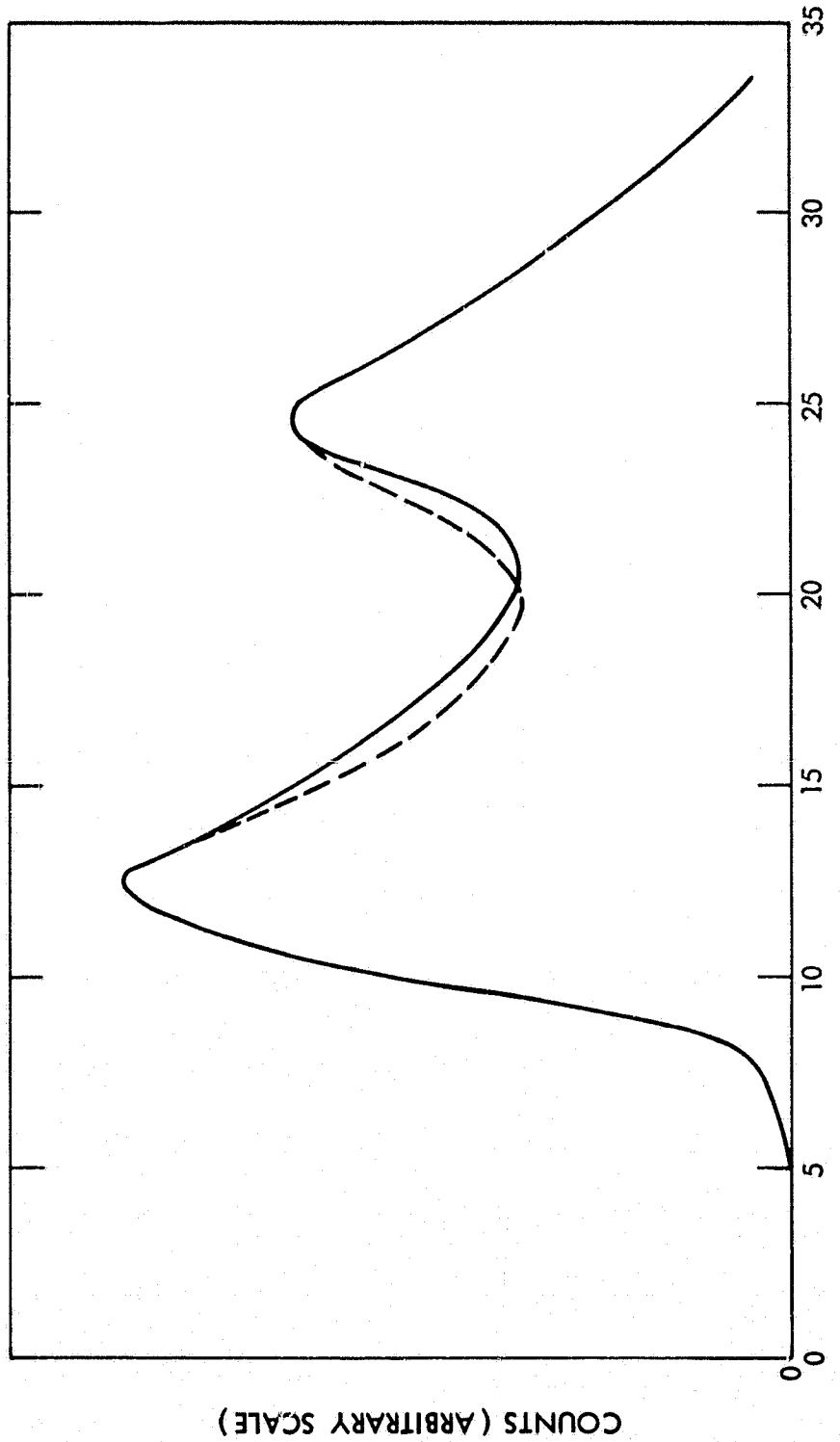

Figure 4— Proportional counter response to Sn-119 m. Solid line: with nonlinear energy calibration. Broken line: with linearized energy calibration

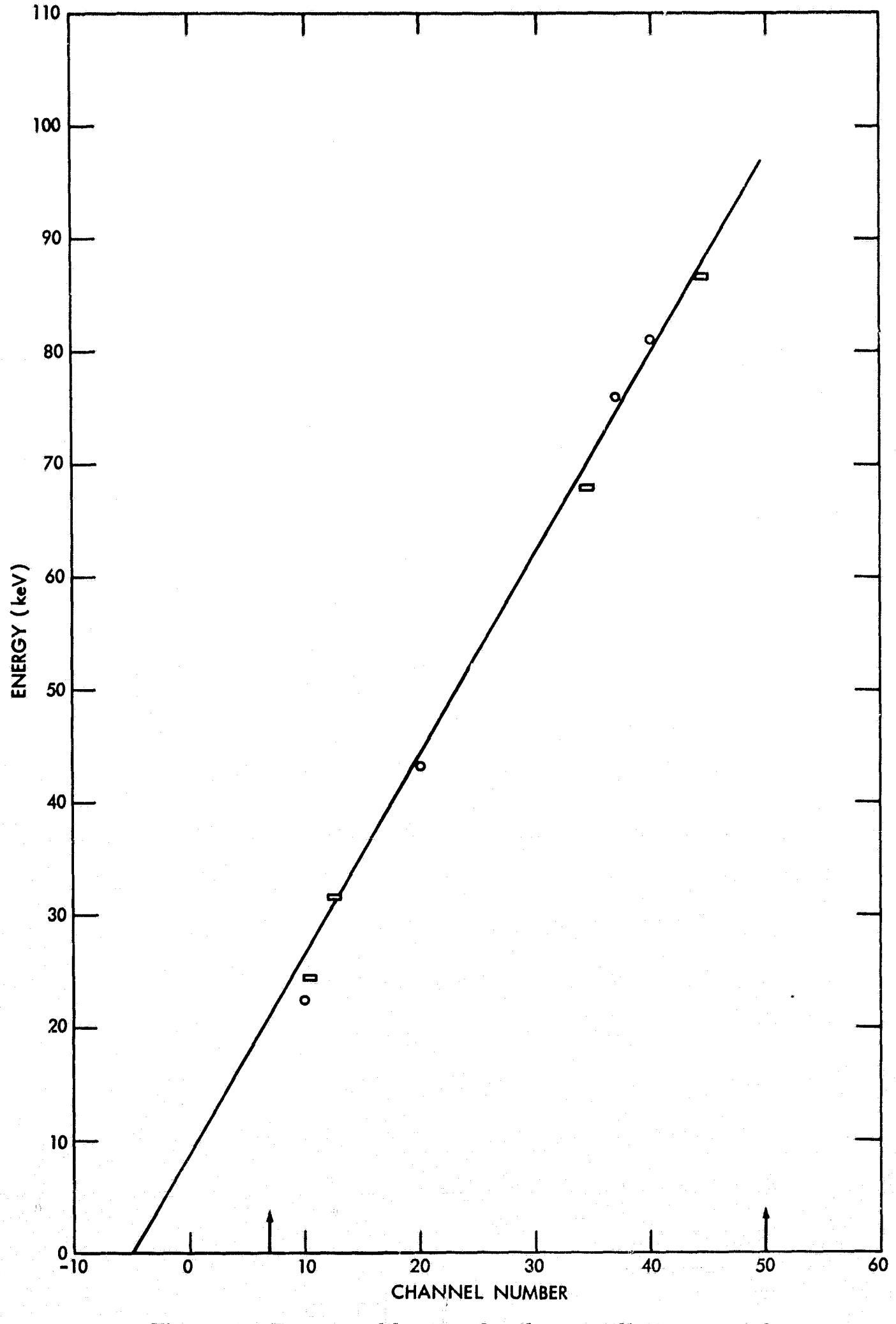

Figure 5— Energy calibration for the scintillation crystal of detector E. Arrows indicate the upper and lower cutoffs

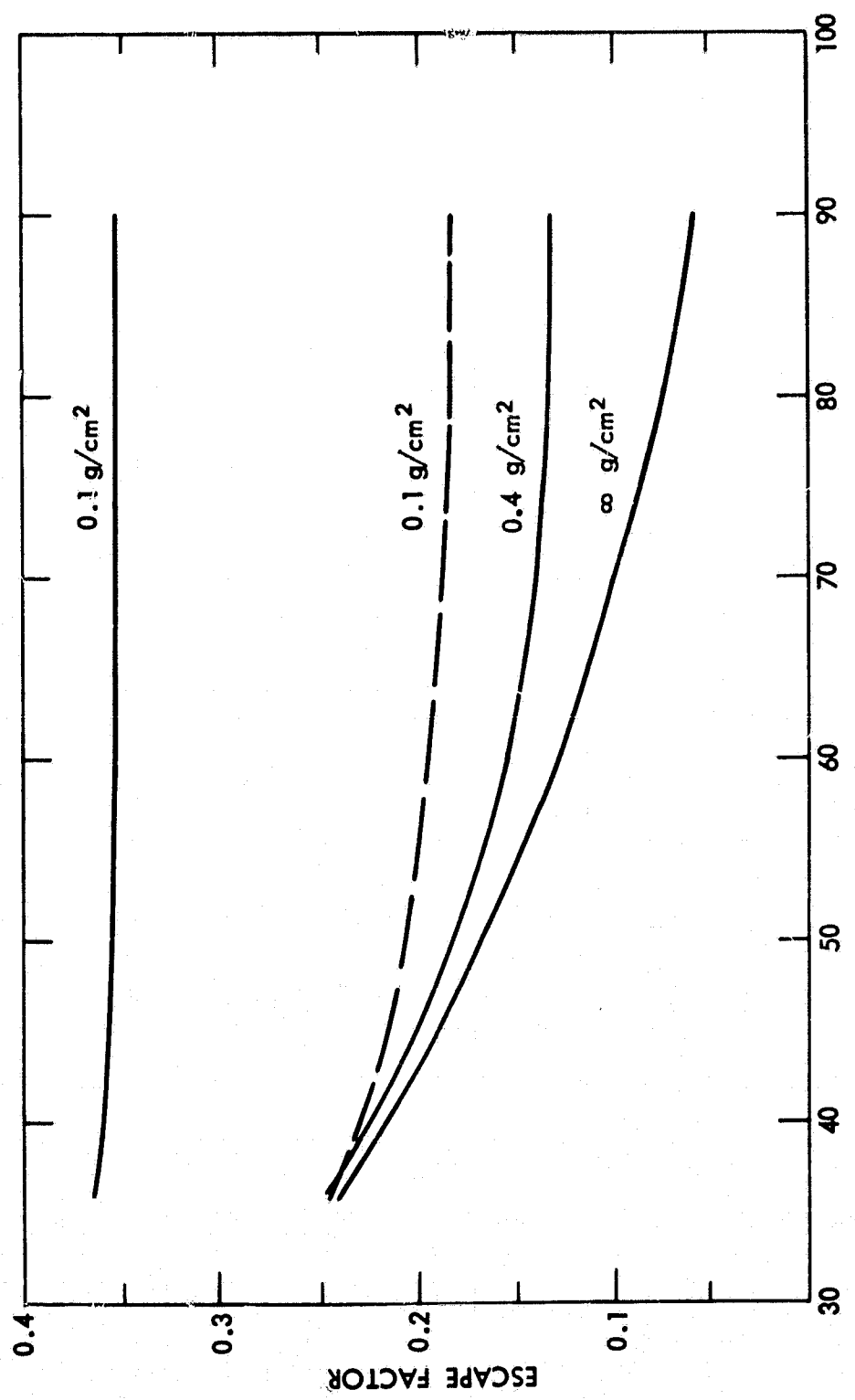

Figure 6— Escape factor η, for CsI. Solid lines: escape from both surfaces. Broken line: escape through only the entrance surface

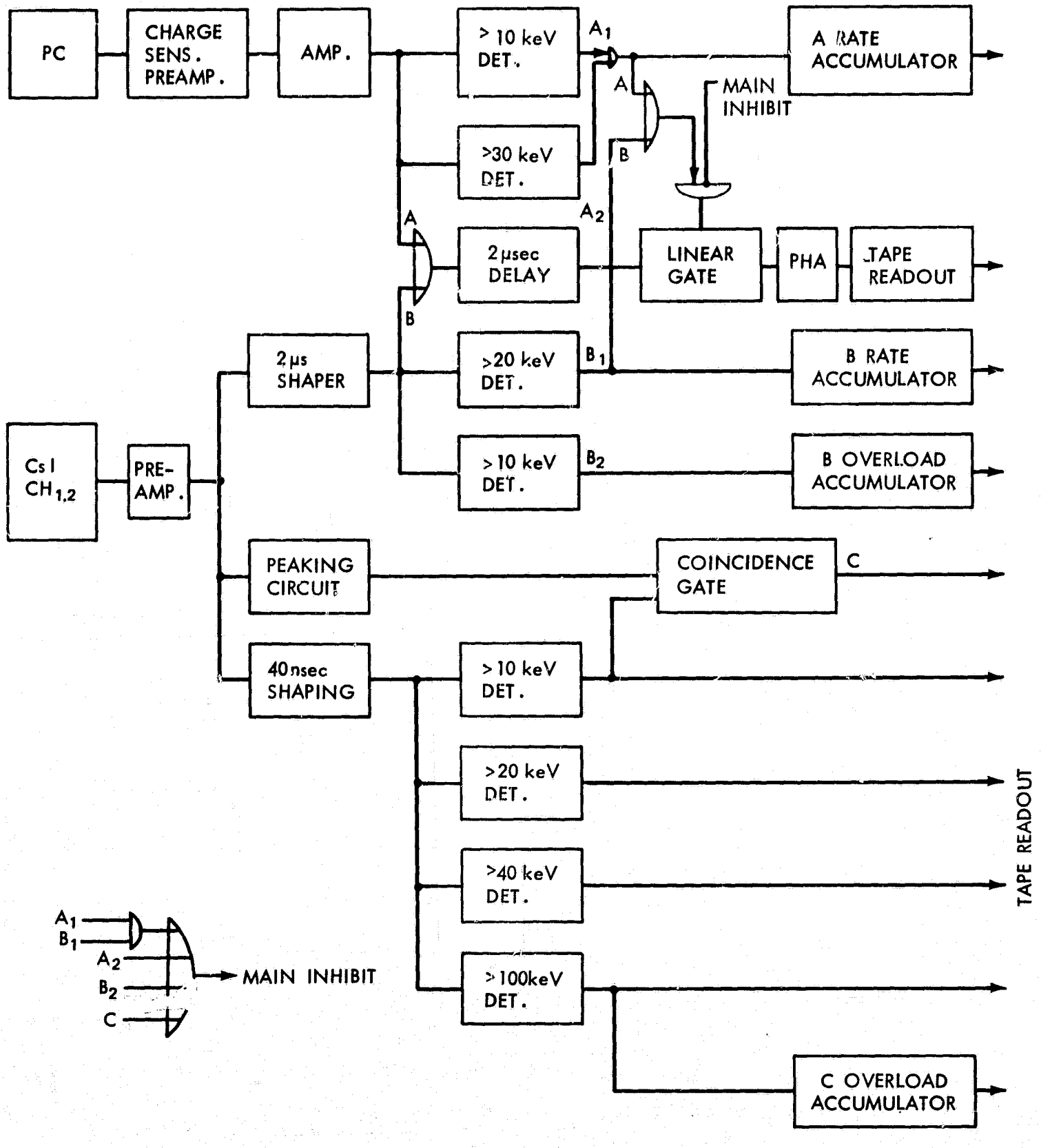

Figure 7— Block diagram for the X-ray telescope

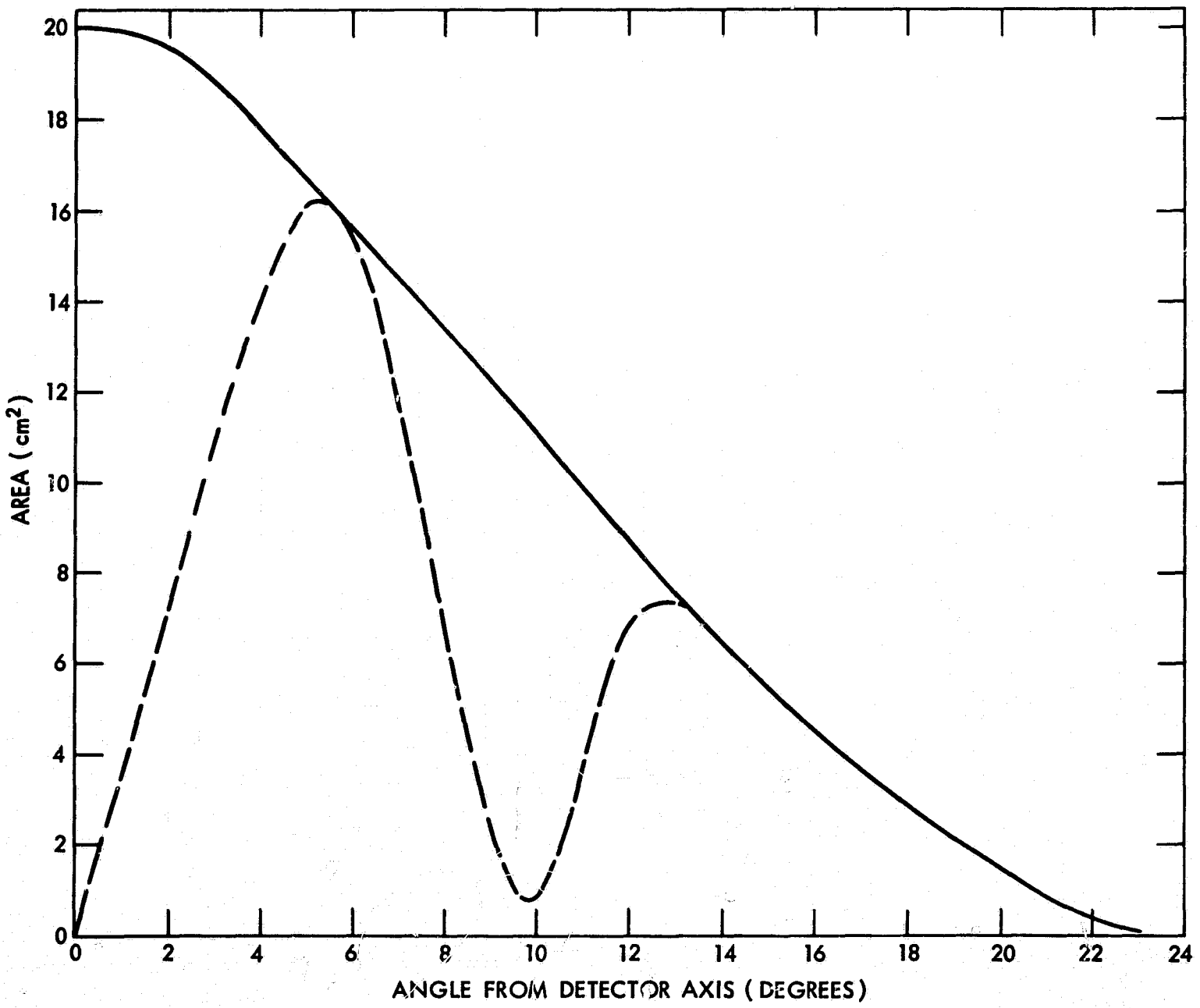

Figure 8— Effective exposure area of the scintillation crystal as a function of the angle from the detector axis. Solid line: unobstructed detector. Broken line: detector with modulation disk and ring

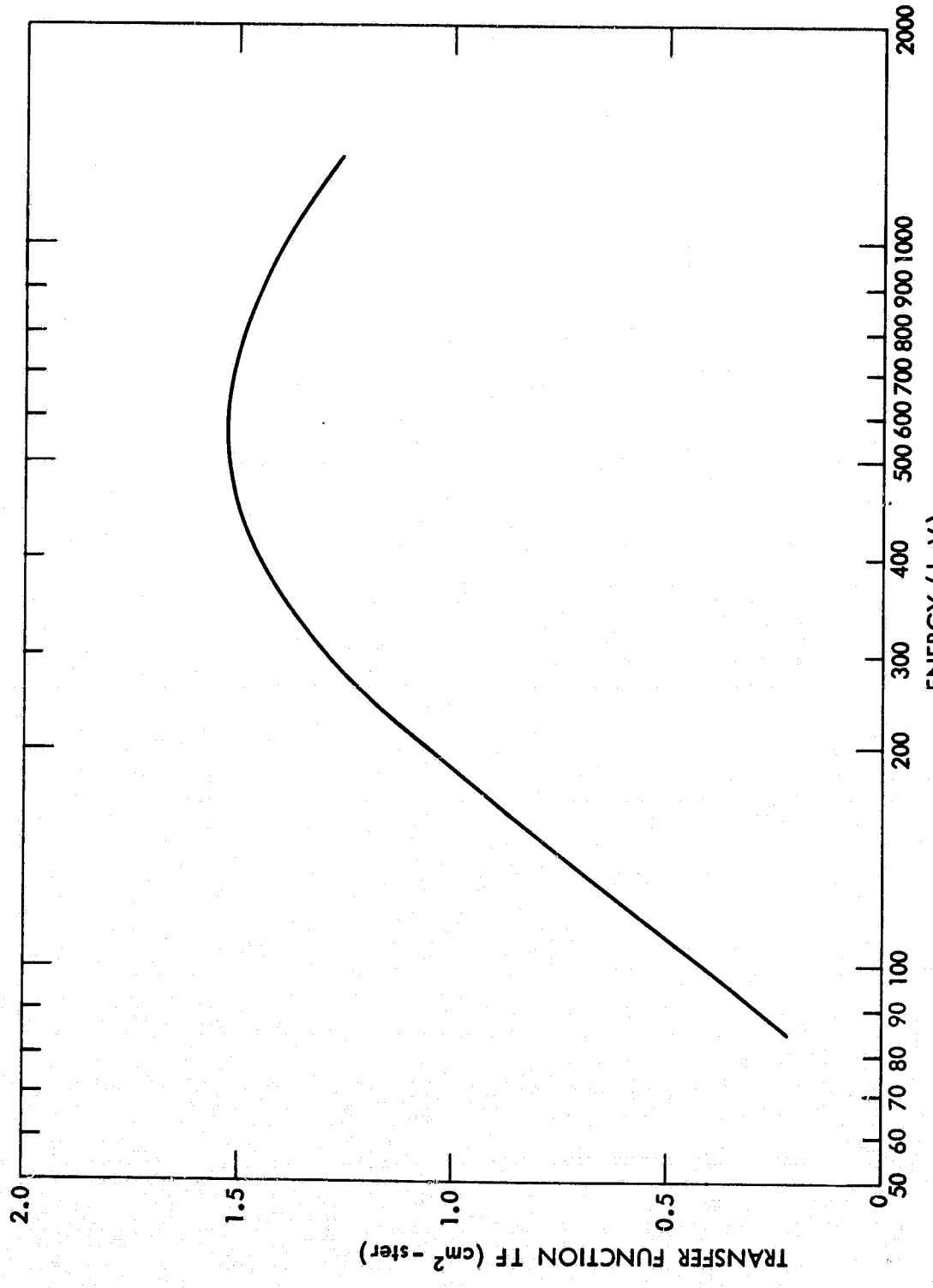

Figure 9— Energy dependence of the transfer function TF (E, 20, 60)

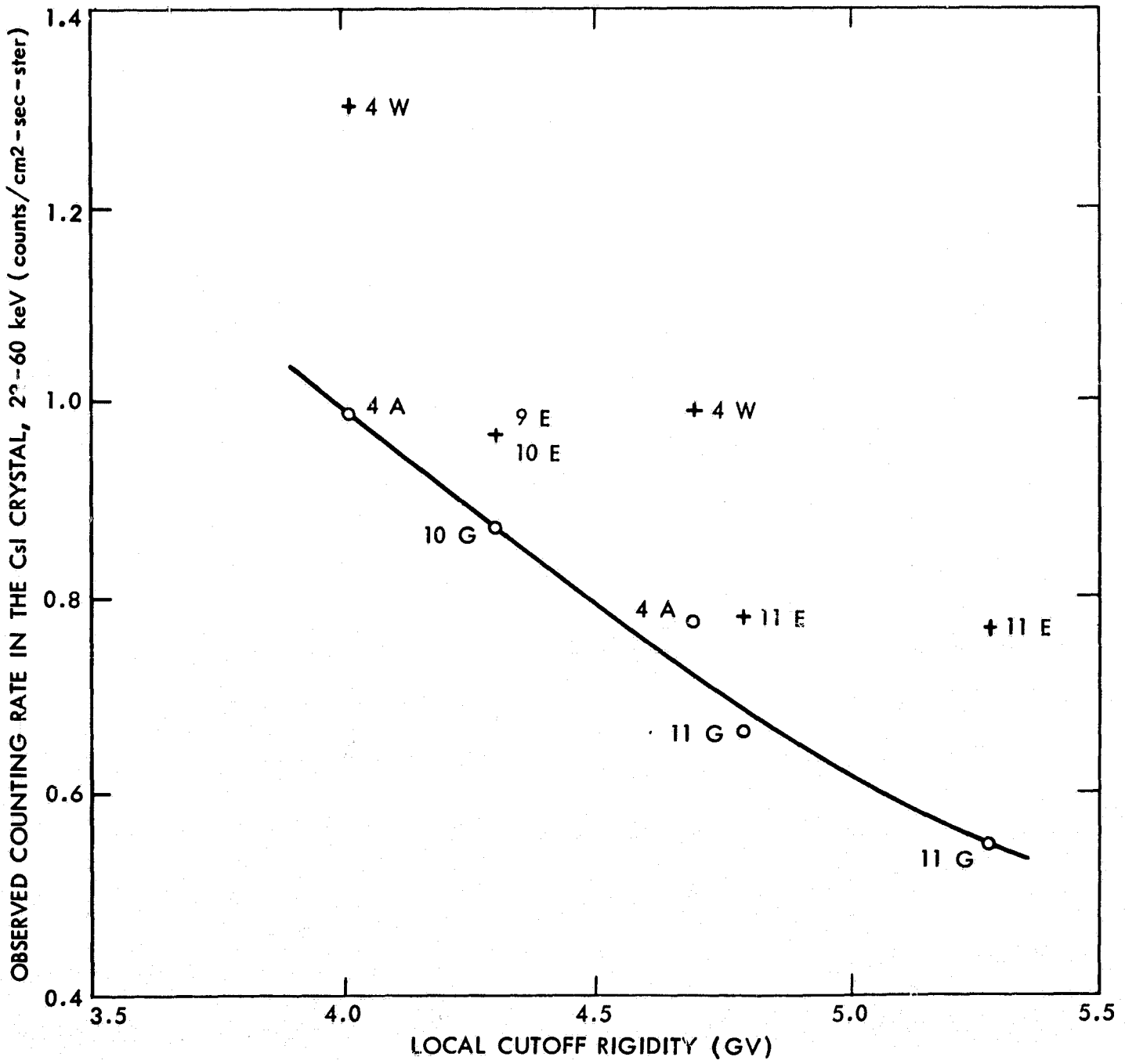

Figure 10— Rigidity dependence of the atmospheric and detector background for the scintillation crystal, 22 - 60 keV. Circles: unobstructed detectors. Crosses: detectors with occultation disk and ring. The line connects data points for unobstructed detectors

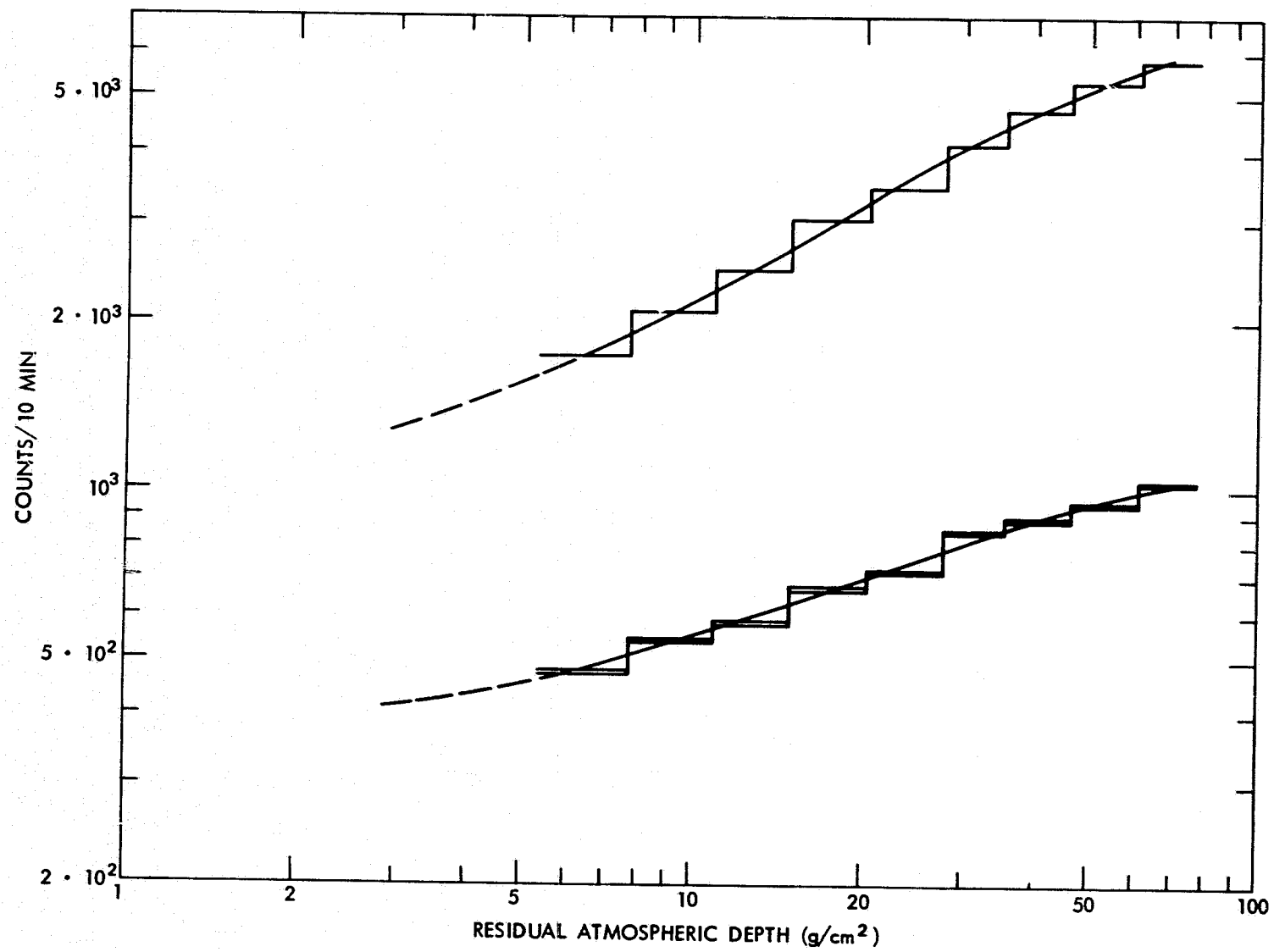

Figure 11— Atmospheric transition profiles for experiment 10. Single bars: scintillation crystal, 22 - 60 keV. Double bars: proportional counter, 12 - 28 keV. Smooth curves: best fits of the function $y(x) = a \exp(-x/b) - c \exp(-x/d)$

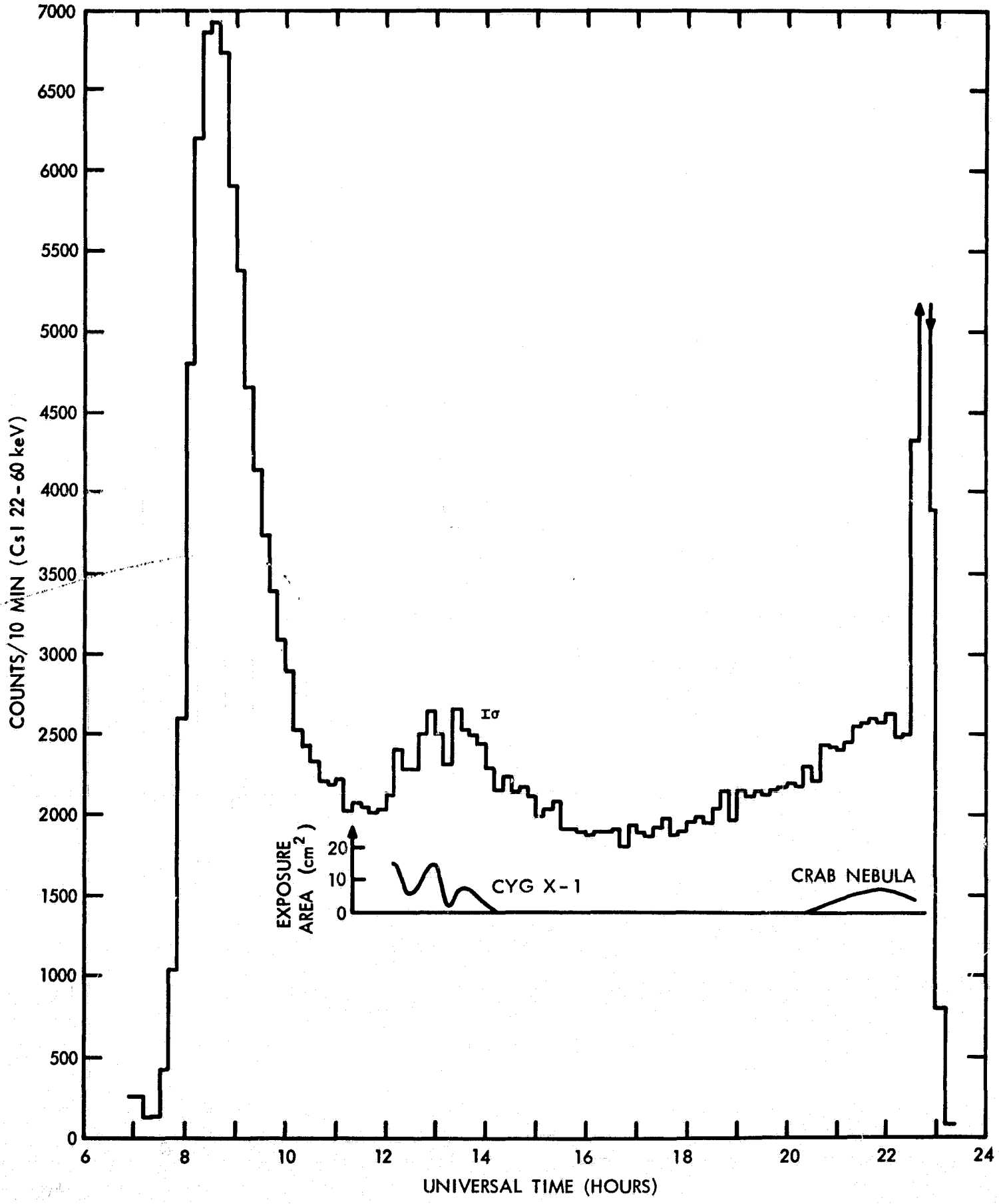

Figure 12— Observed counting rate in the scintillation crystal of detector W (22 - 60 keV) in experiment 4. The exposure to Cyg XR-1 and to the Crab Nebula is indicated

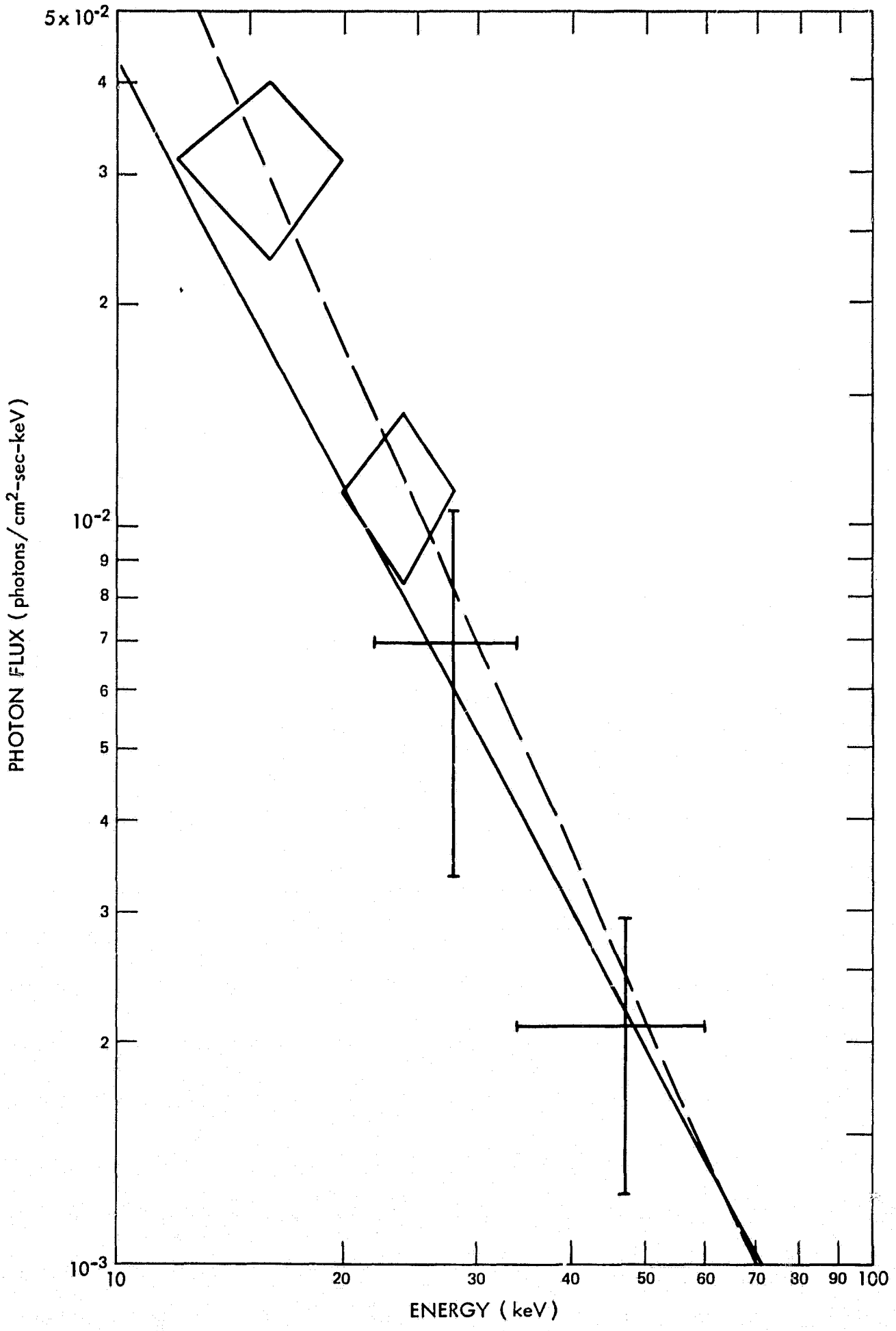

Figure 13— Net photon spectrum of the Crab Nebula (detector A, experiment 4). Diamonds: proportional counter. Crosses: scintillation crystal. Solid line: measurement by Peterson et al. (1968). Broken line: summary by Gould (1967)

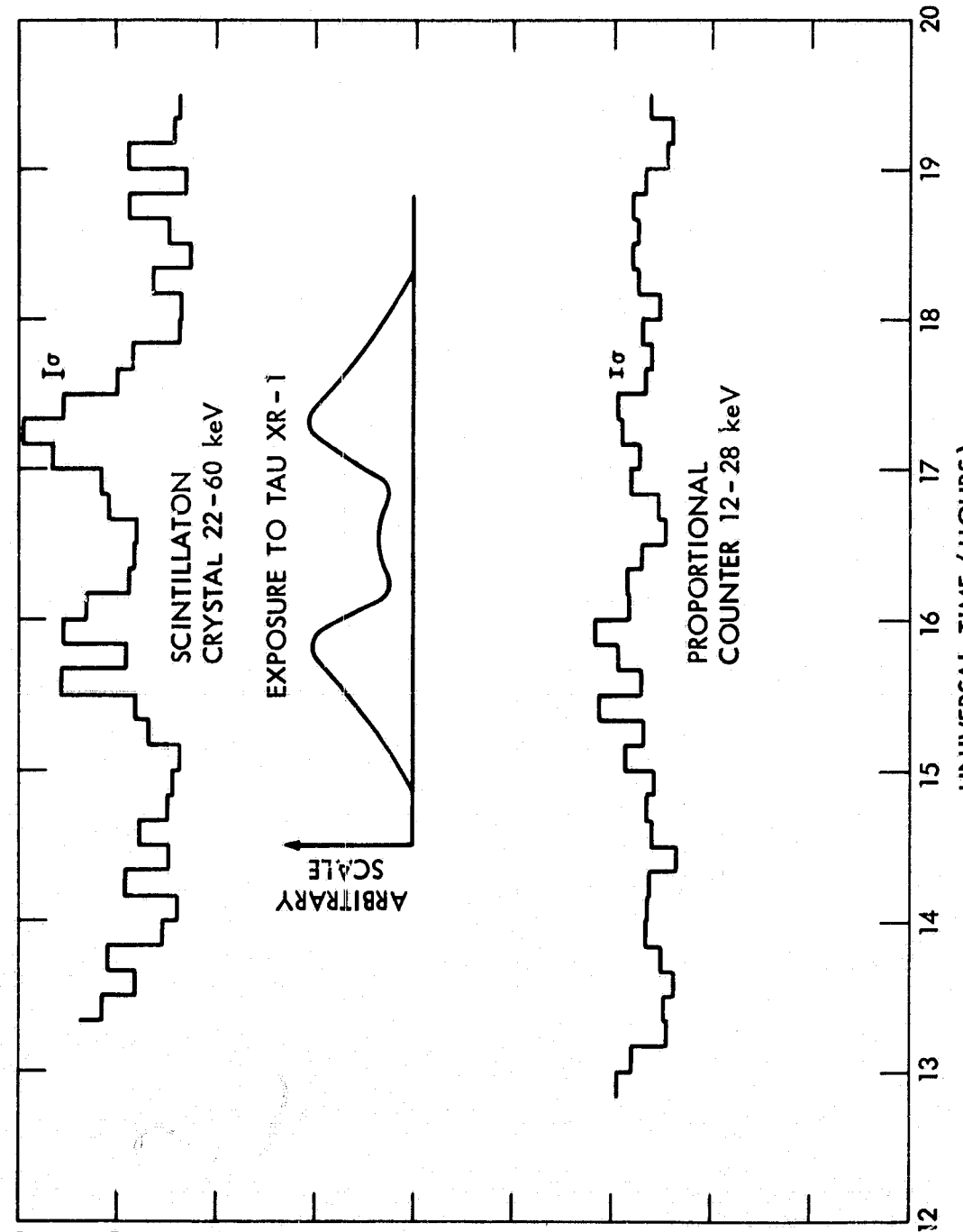

Figure 14— Counting rate observed by detector E in experiment 11.
Top curve: CsI crystal, 22 - 60 keV. Bottom curve:
proportional counter, 12 - 28 keV. Middle curve: ex-
posure to a source at the position of the Crab Nebula

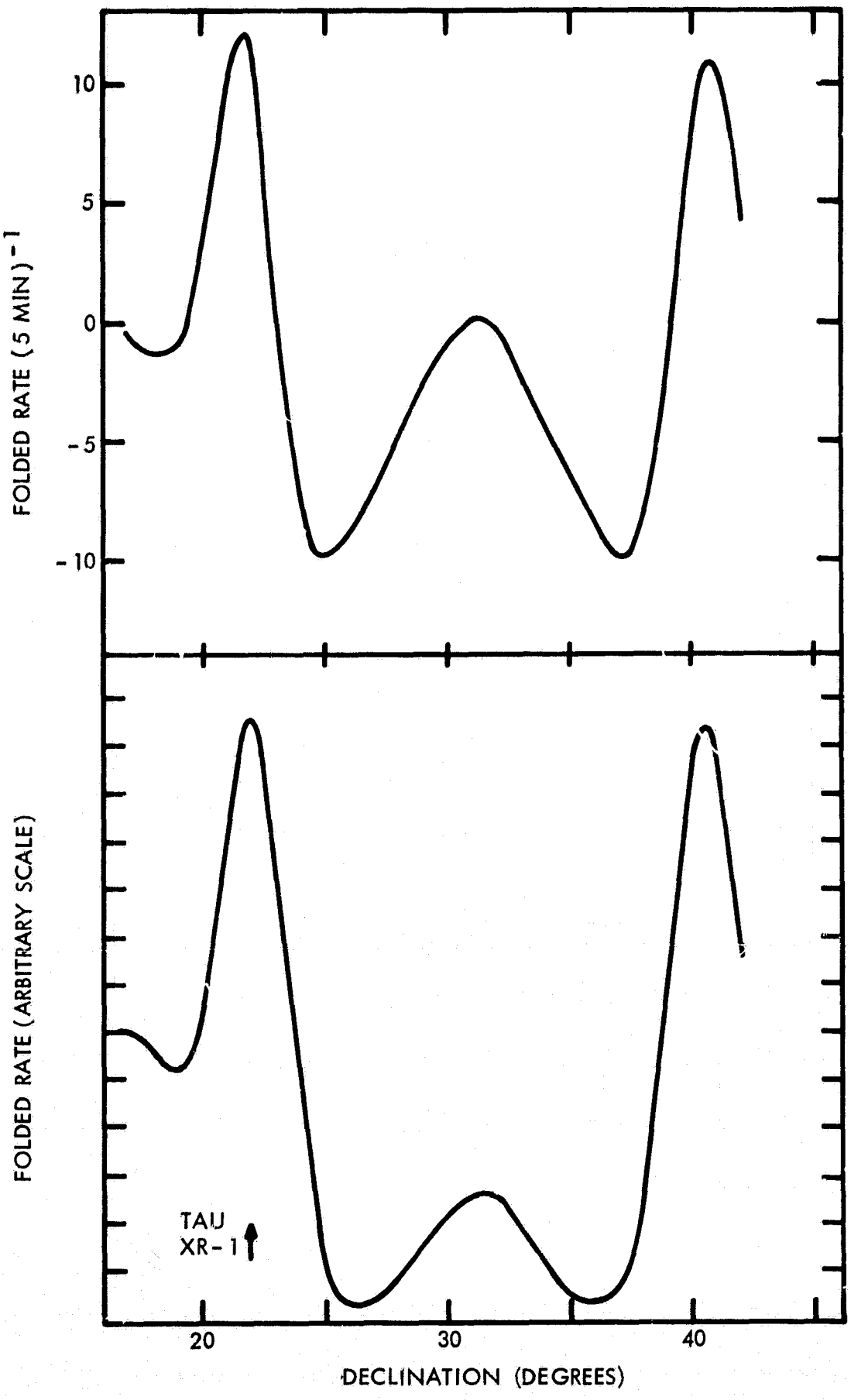

Figure 15— Determination of the dominant source declination based on the counting rate of detector E in experiment 11. Upper curve: CsI crystal data, 22 - 60 keV. Lower curve: with simulated data assuming a source at the position of Tau XR-1

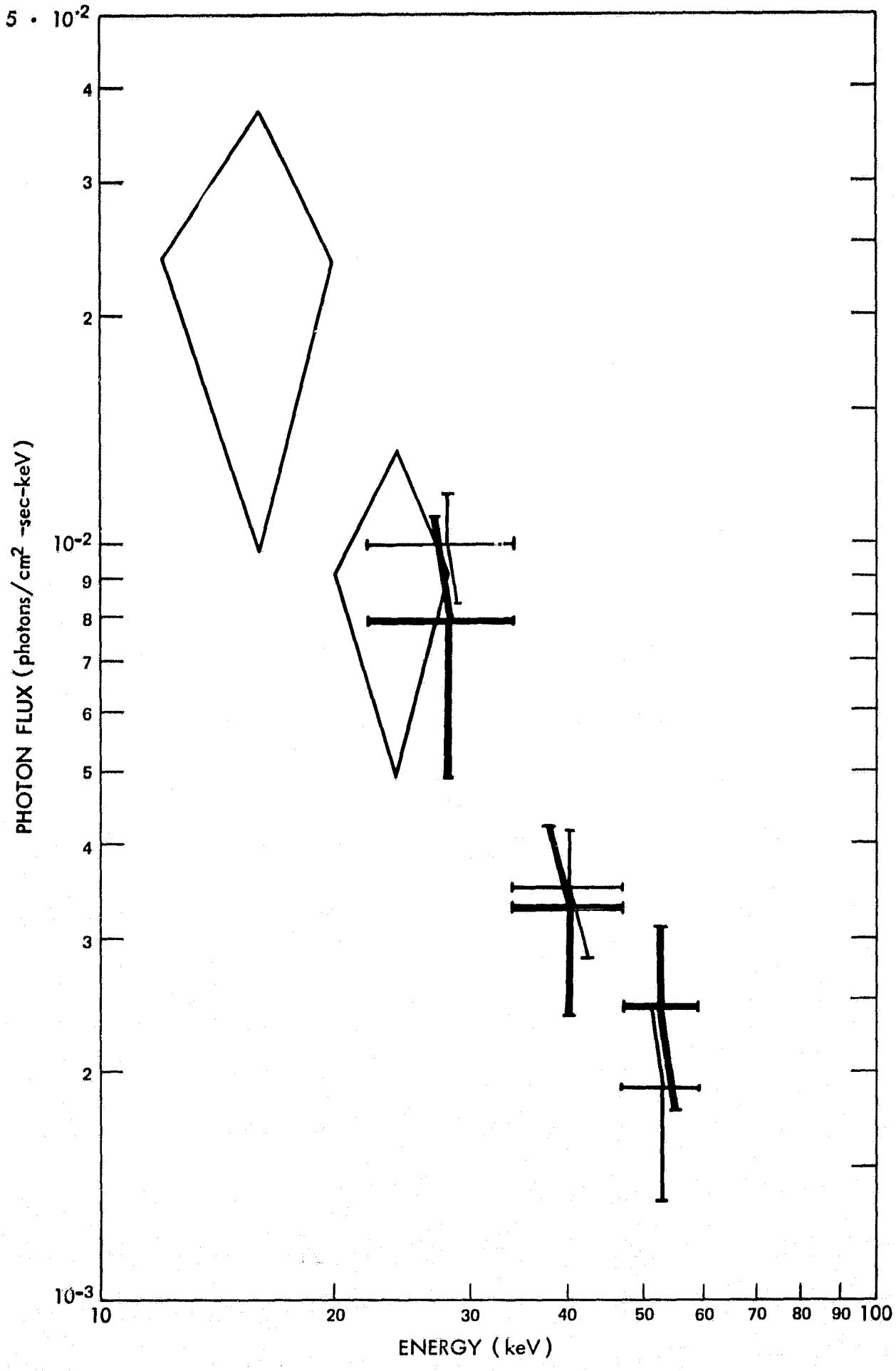

Figure 16— Net photon spectrum of the Crab Nebula (experiment 11). Diamonds: proportional counter of detector E. Double-bar crosses: scintillation crystal of detector E. Single-bar crosses: scintillation crystal of detector G

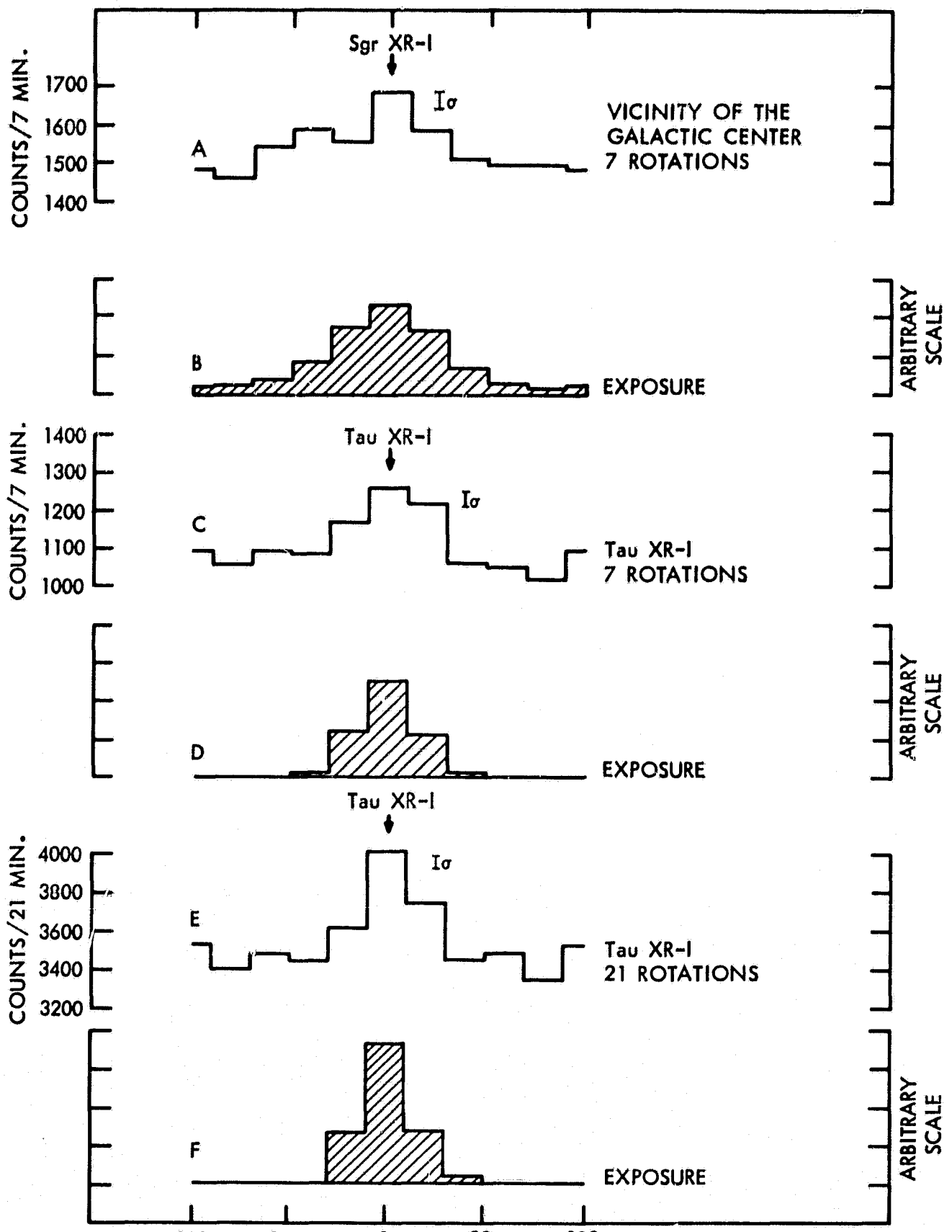

Figure 17— Superposition of epochs for the CsI crystal data (22 - 60 keV) for experiment 10 (A) and experiment 11 (C, E). The calculated exposures corresponding to A, C, and E are shown in B, D, and F, respectively. The brackets indicate 1σ-levels

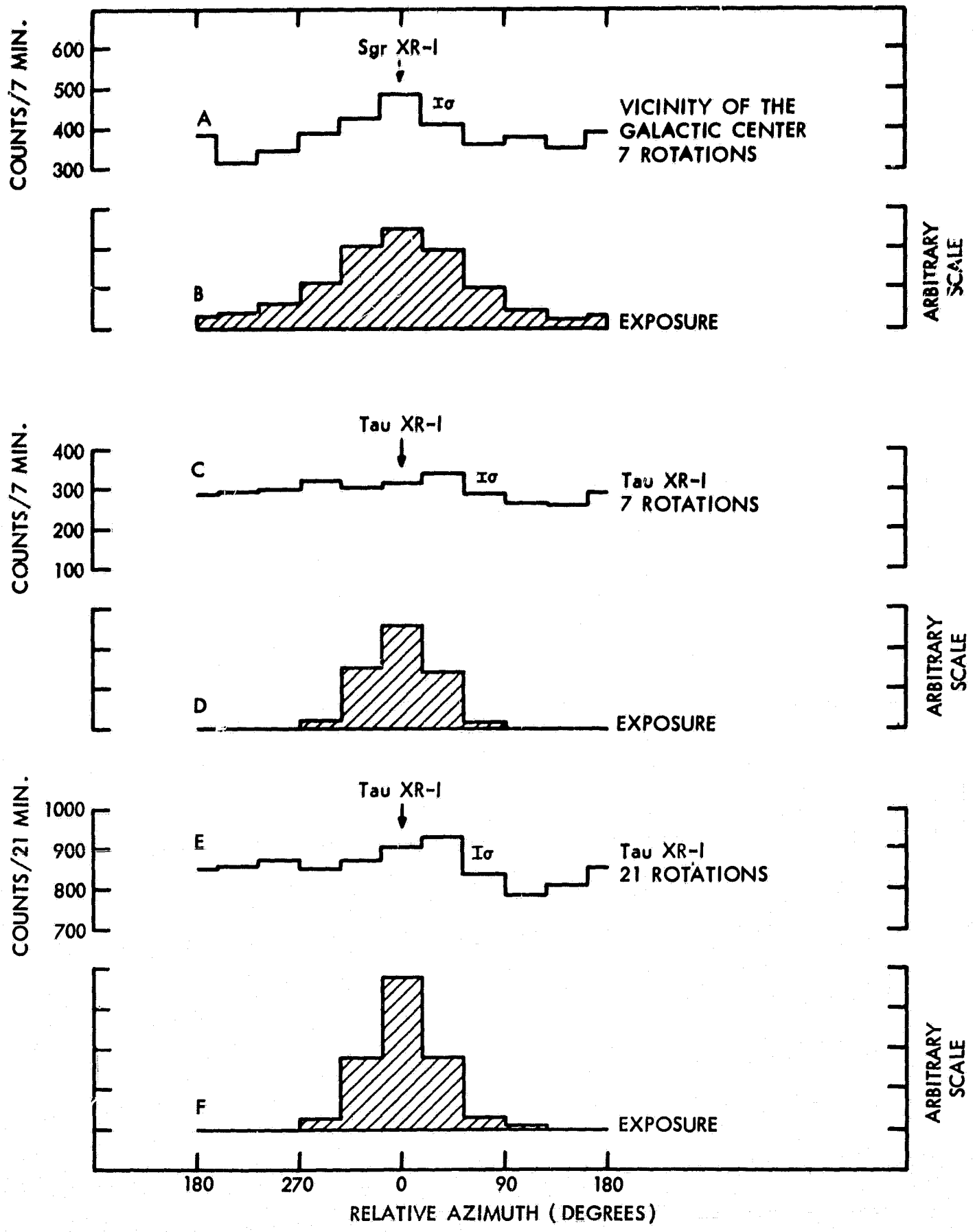

Figure 18— Superposition of epochs for the proportional counter data (12 - 28 keV) for experiment 10 (A) and experiment 11 (C, E). The calculated exposures corresponding to A, C, and E are shown in B, D, and F, respectively. The brackets indicate 1σ-levels

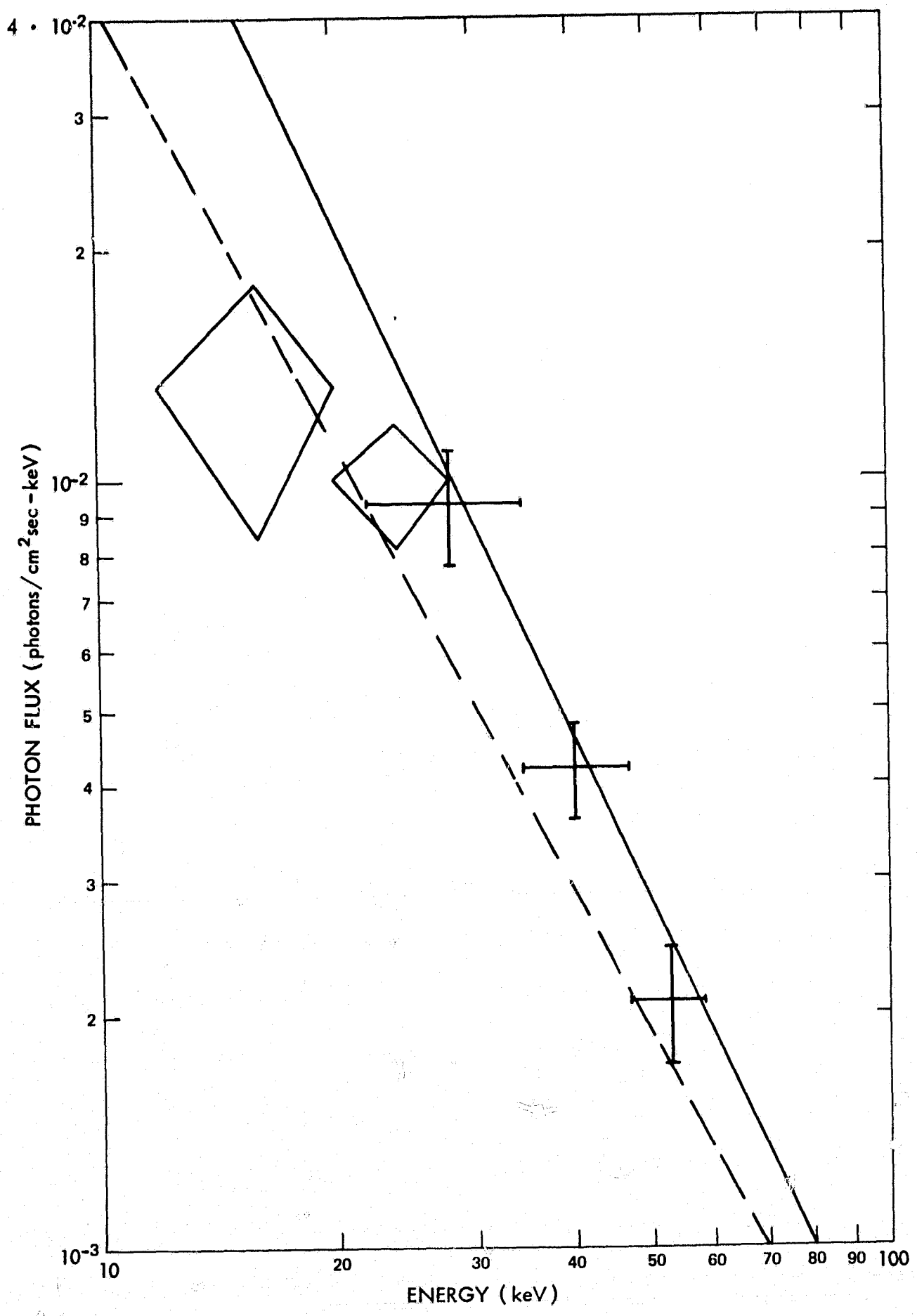

Figure 19— Net photon spectrum of Cyg XR-1 (detector A, experiment 4). Diamonds: proportional counter. Crosses: CsI crystal. Solid line: measurements by Bleeker et al. (1967). Broken line: measurements by Peterson et al. (1968)

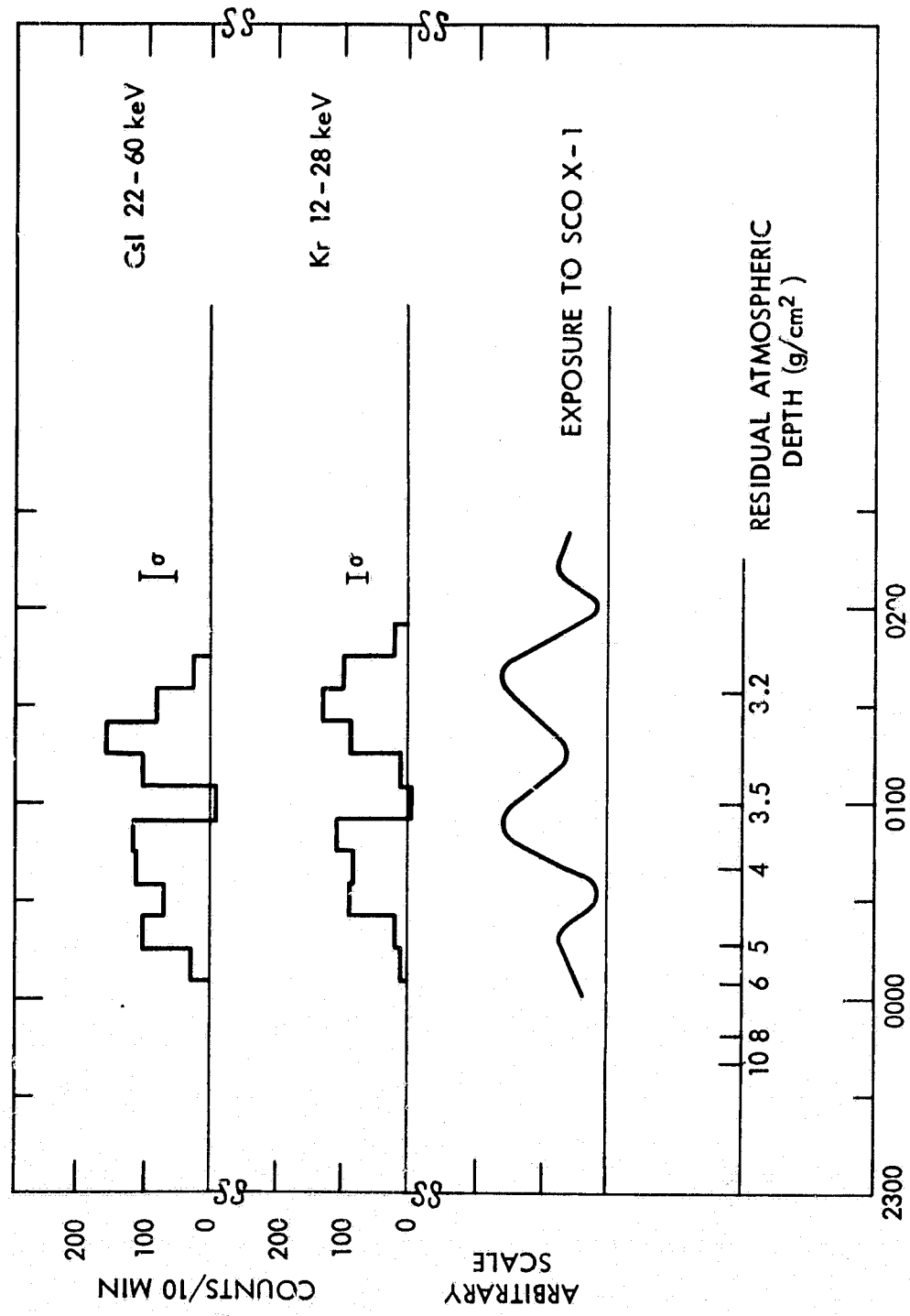

Figure 20— Net observed counting rate due to Sco X-1 in experiment 9. Top curve: CsI crystal, 22 - 60 keV. Middle curve: proportional counter, 12 - 28 keV. Bottom curve: exposure to Sco X-1. The relation between the residual atmospheric depth and universal time is indicated in the lower part of the figure

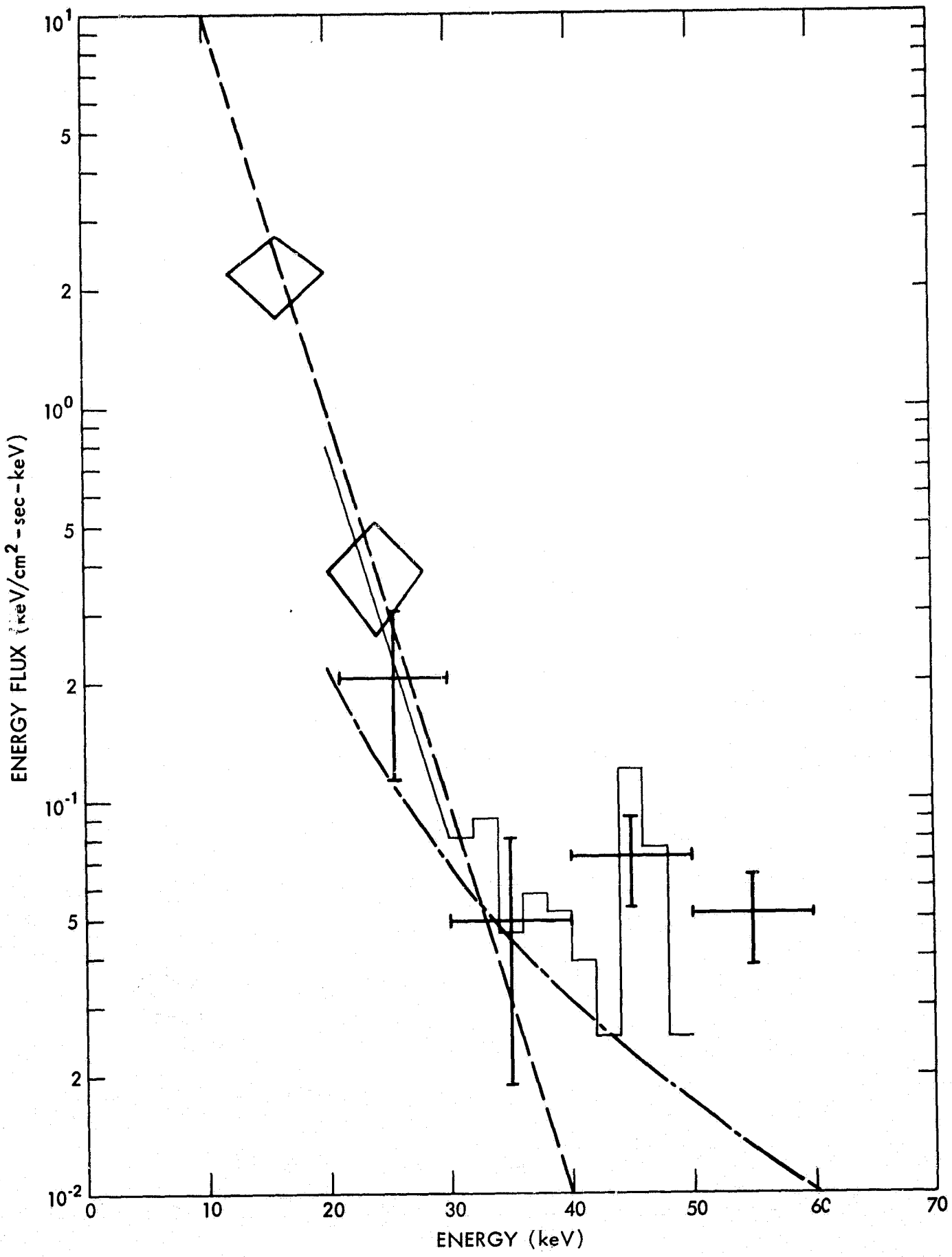

Figure 21— Net energy spectrum of Sco X-1. Diamonds: proportional counter results of experiment 9. Crosses: CsI crystal results of experiment 9. Solid line: schematic representation of the results of Peterson and Jacobson (1966b), 18 June 1965. Broken line: thermal spectrum for $T = 5 \cdot 10^7$ °K. Dash-dotted line: best-fit power-law to the data of Buselli et al. (1968), 29 February 1968

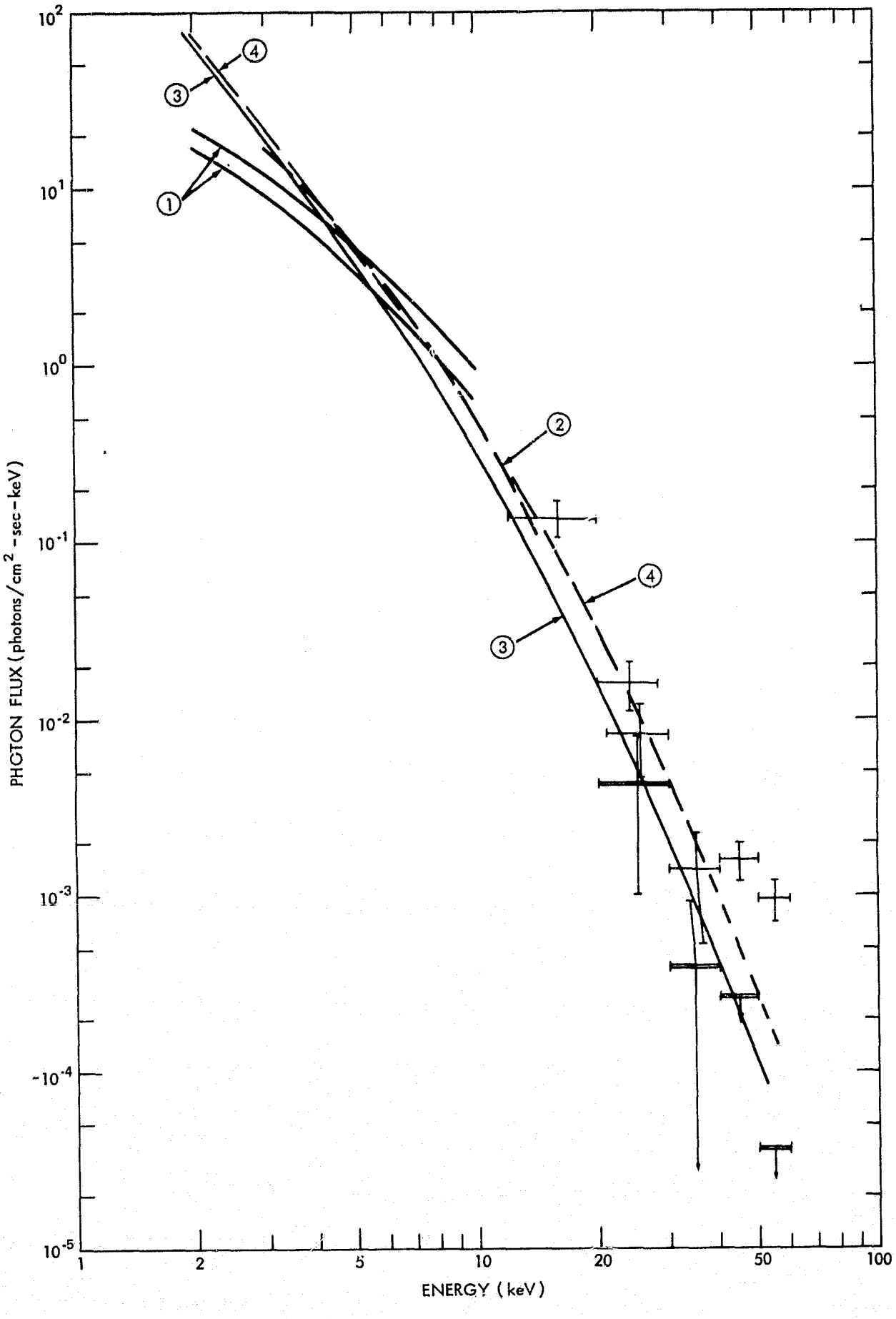

Figure 21a— The X-ray spectrum of Sco X-1. Crosses: this experiment (15 Dec. 1966). Double-bar crosses: Lewin et al. (1967) (13 Feb. 1967). Curve 1: Chodil et al. (1968) (2 Sept. 1967). Curve 2: Gorenstein et al. (1968) (11 Oct. 1966). Curve 3: bremsstrahlung from isovelocity plasma. Curve 4: bremsstrahlung from isovelocity plasma with higher level of ionization.

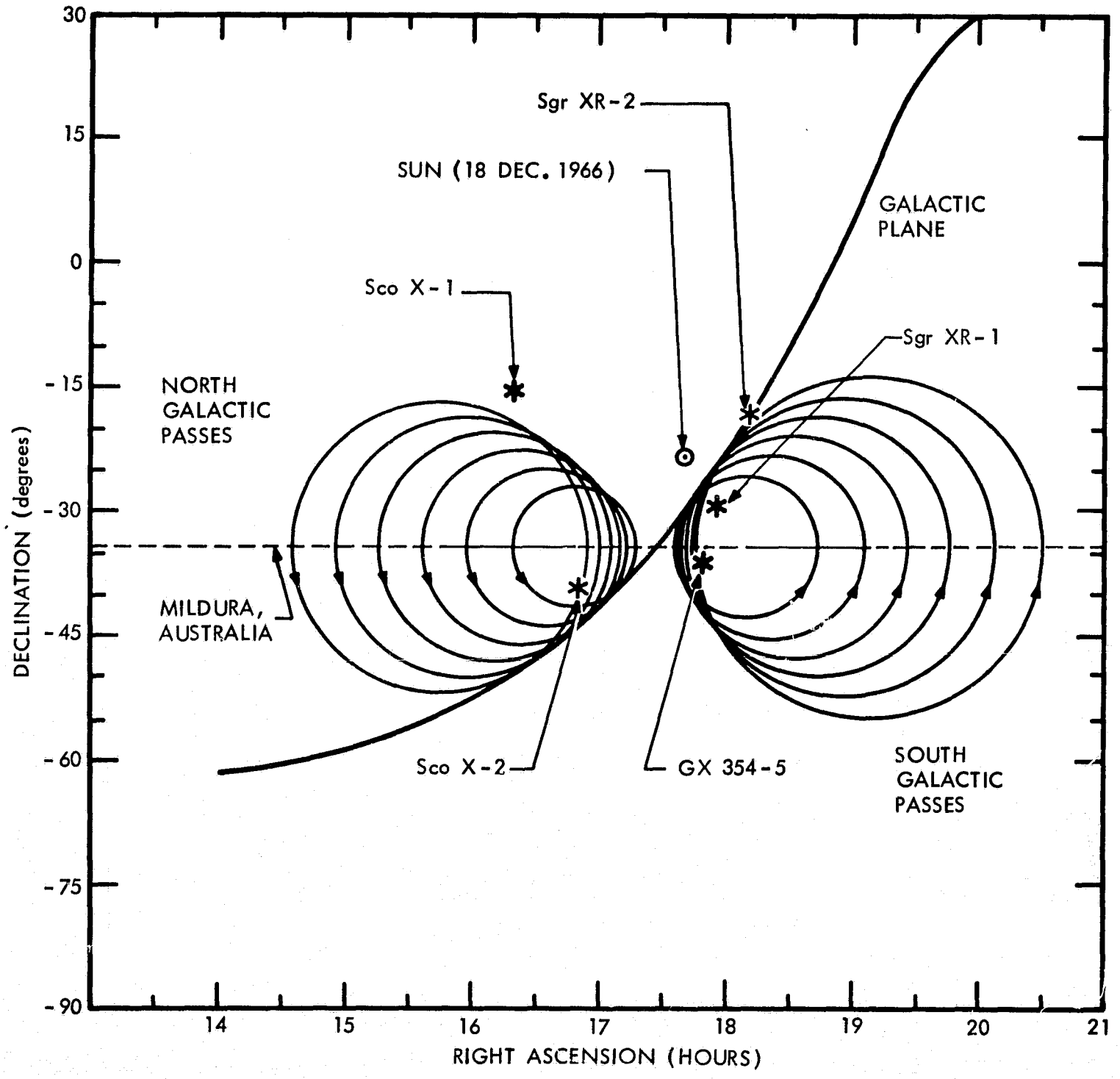

Figure 22— Trajectory of the axis of detector G on the celestial sphere during experiment 10. Six passes from galactic north and 6 passes from galactic south are drawn. Some relevant sources of low-energy X-radiation are shown

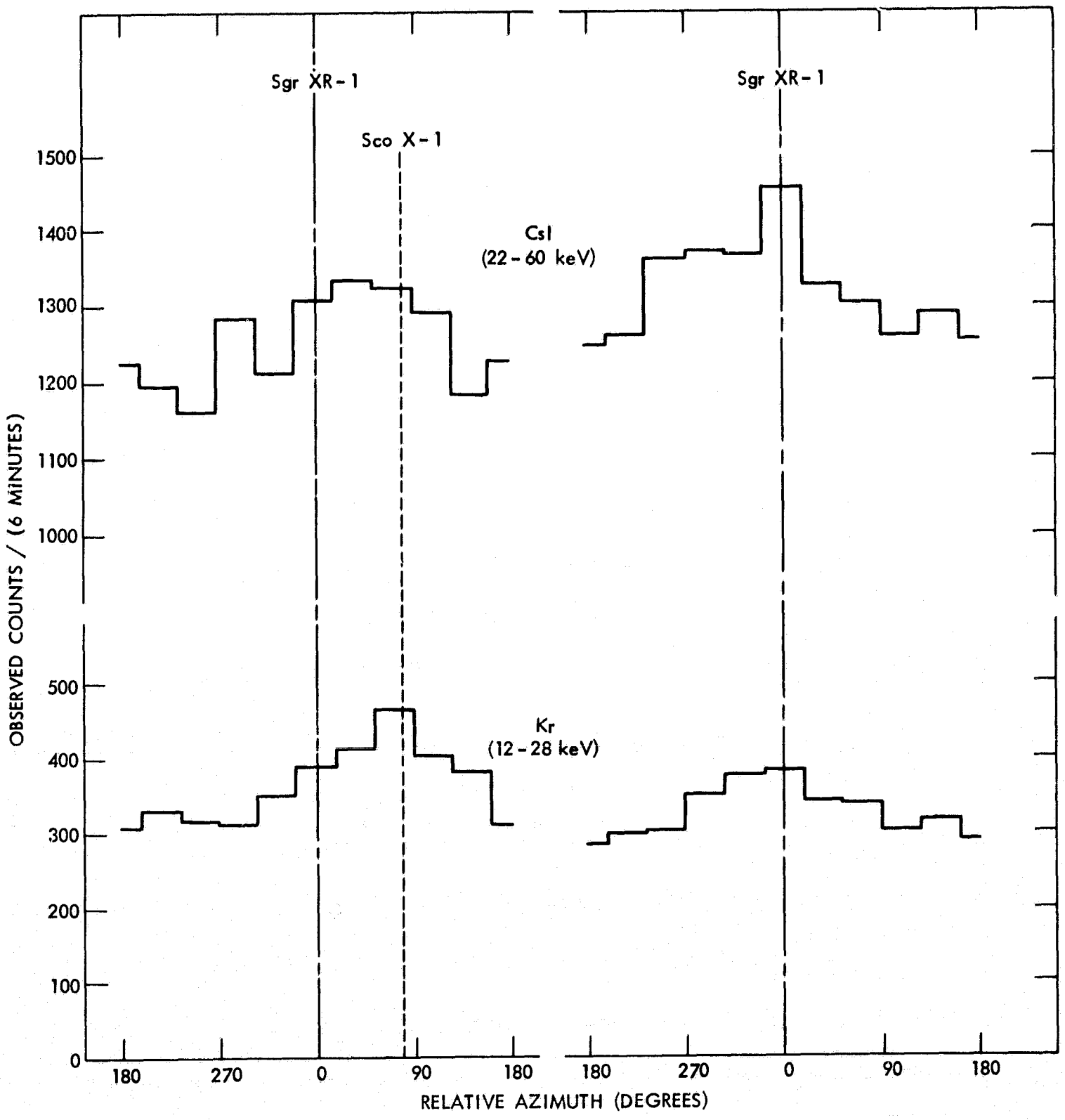

Figure 23— Superposition of epochs for 6 passes from galactic north (left side) and from galactic south (right side) during experiment 10. The azimuth angles of Sgr XR-1 and Sco X-1 are indicated. Upper curves: CsI crystal, 22 - 60 keV. Lower curves: proportional counter, 12 - 28 keV.

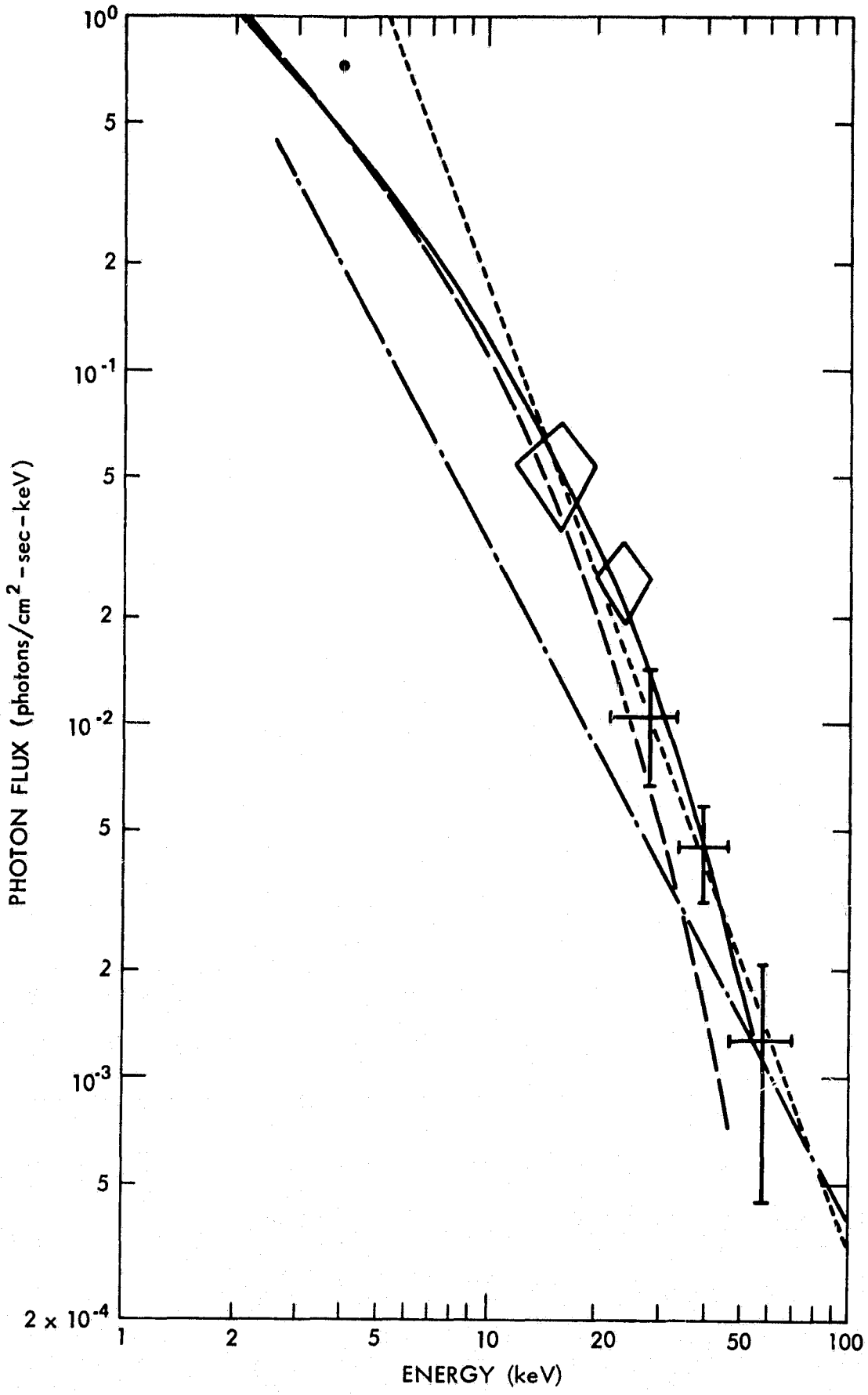

Figure 24— Net photon flux from the vicinity of the galactic center (experiment 10, detector G). Diamonds: proportional counter. Crosses: scintillation detector: Dotted line: best-fit power-law, n = 2.69. Solid line: best-fit exponential law, kT = 16 keV. Broken line: best-fit exponential spectrum with kT = 11 keV for the data of Lewin et al. (1968b). Dash-dotted line: best-fit power-law with n = 2.0 for the observation of GX 3+1 by Buselli et al. (1968). Circle: expected flux at 4 keV

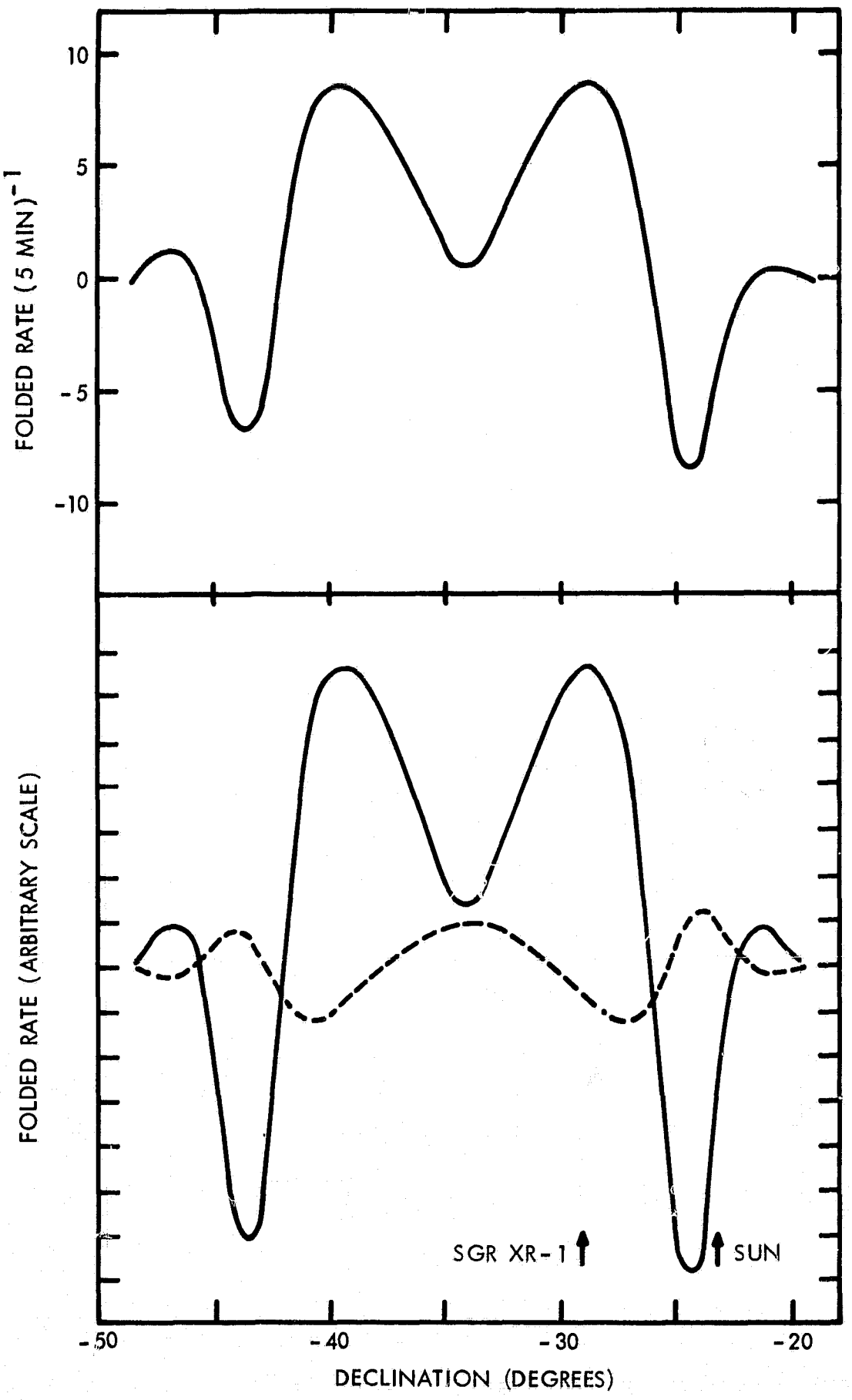

Figure 25— Determination of the dominant source declination based on the counting rate of detector E in experiment 10. Upper curve: CsI crystal data, 22 - 60 keV. Lower part: with simulated data assuming a source at the position of Sgr XR-1 (solid line and the sun) (broken line)

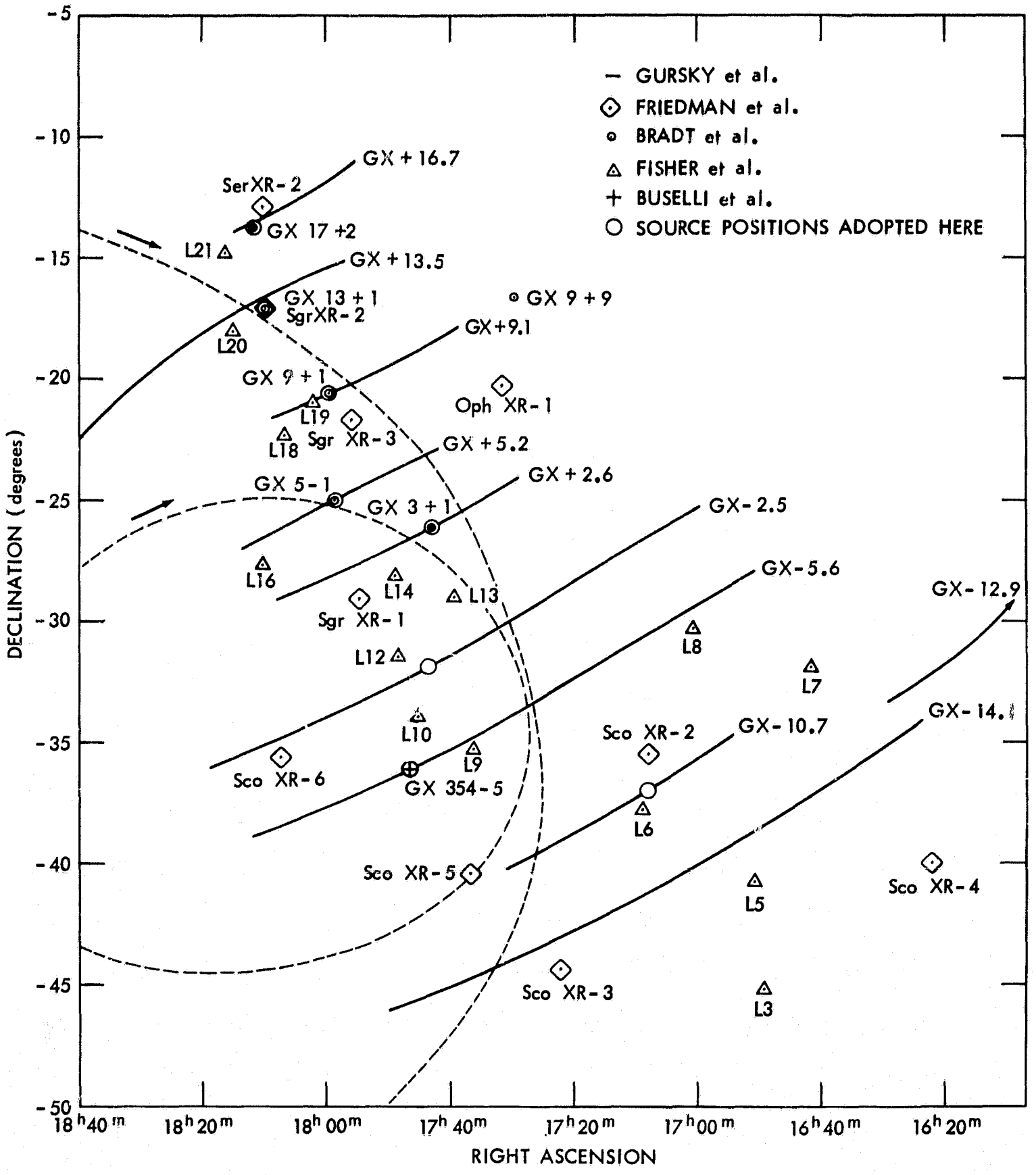

Figure 26— Map of the sky in the vicinity of the galactic center. Broken lines: trajectory of the detector axis of telescope G during the first and last rotation of data accumulation in experiment 10. Source positions: solid lines: Gursky et al. (1967), diamonds: Friedman et al. (1967b), small circles: Bradt et al. (1968a), triangles: Fisher et al. (1968), crosses: Buselli et al. (1968), large circles: source positions adopted here

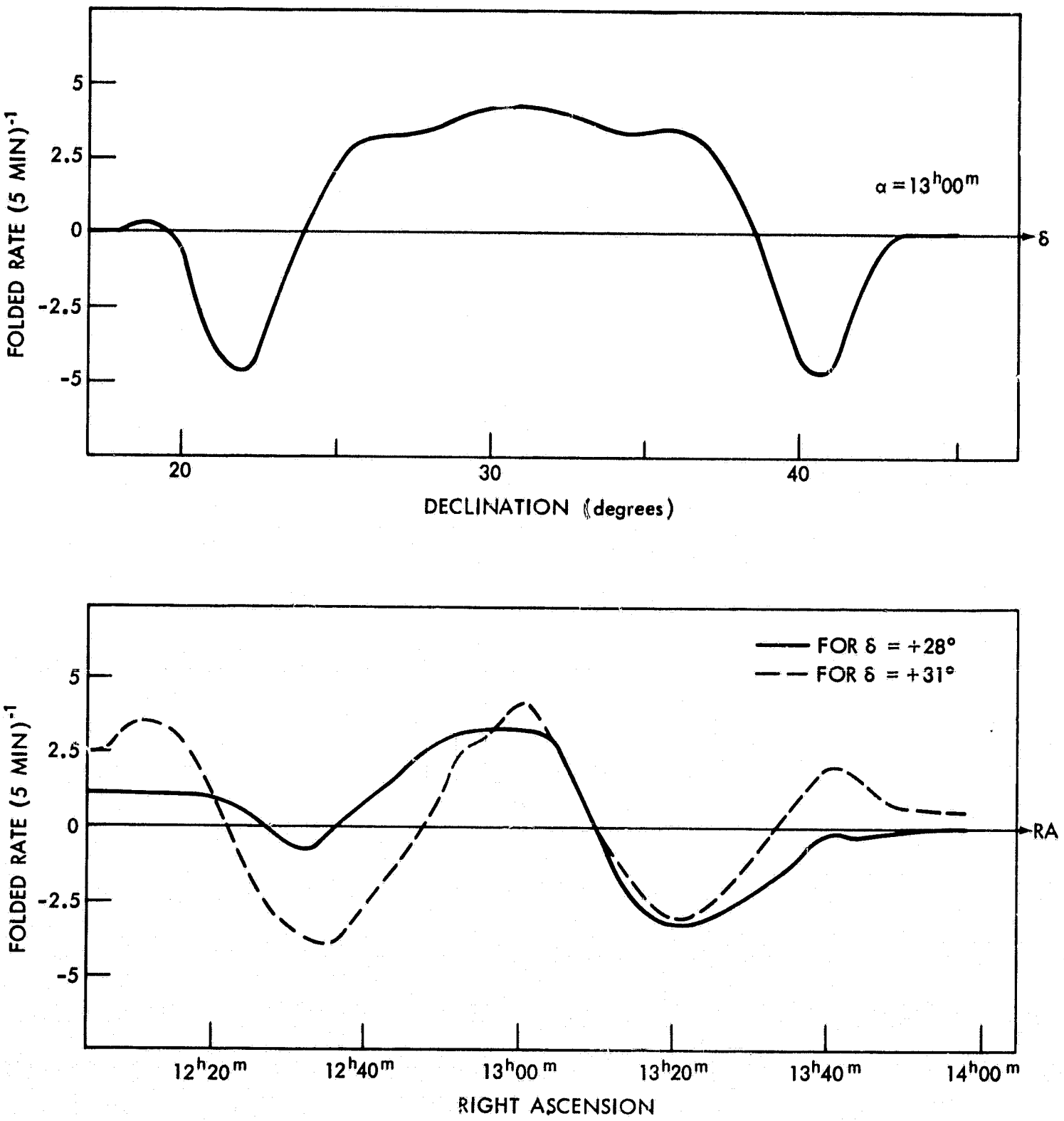

Figure 27— Folded counting rates $R(\alpha, \delta)$ for experiment 1. The upper graph shows $R(\alpha = 13^h00^m, \delta)$ versus declination. The lower graph shows $R(\alpha, \delta = +28)$ (solid line) and $R(\alpha, \delta = +31°)$ (broken line) versus right ascension

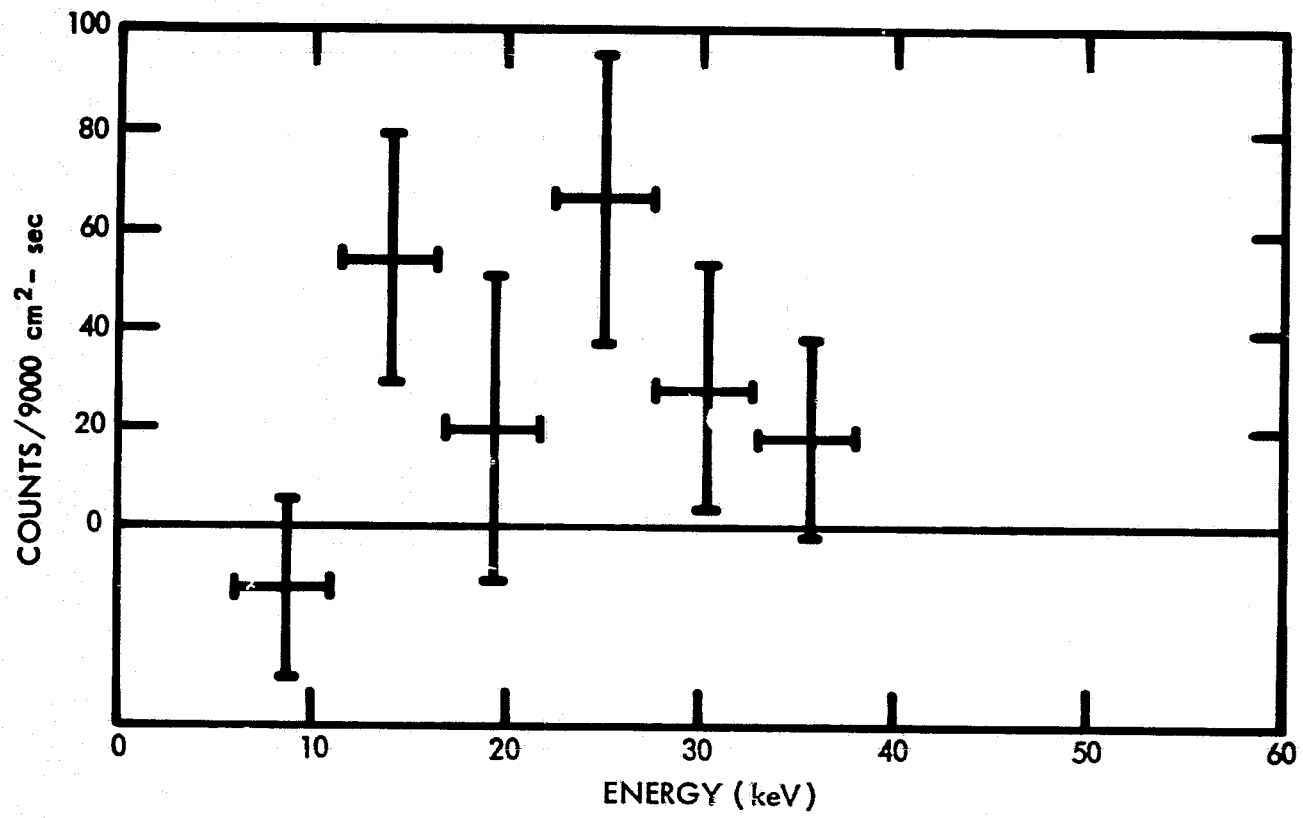

Figure 28— Counting rate spectrum observed by the proportional counter in experiment 1

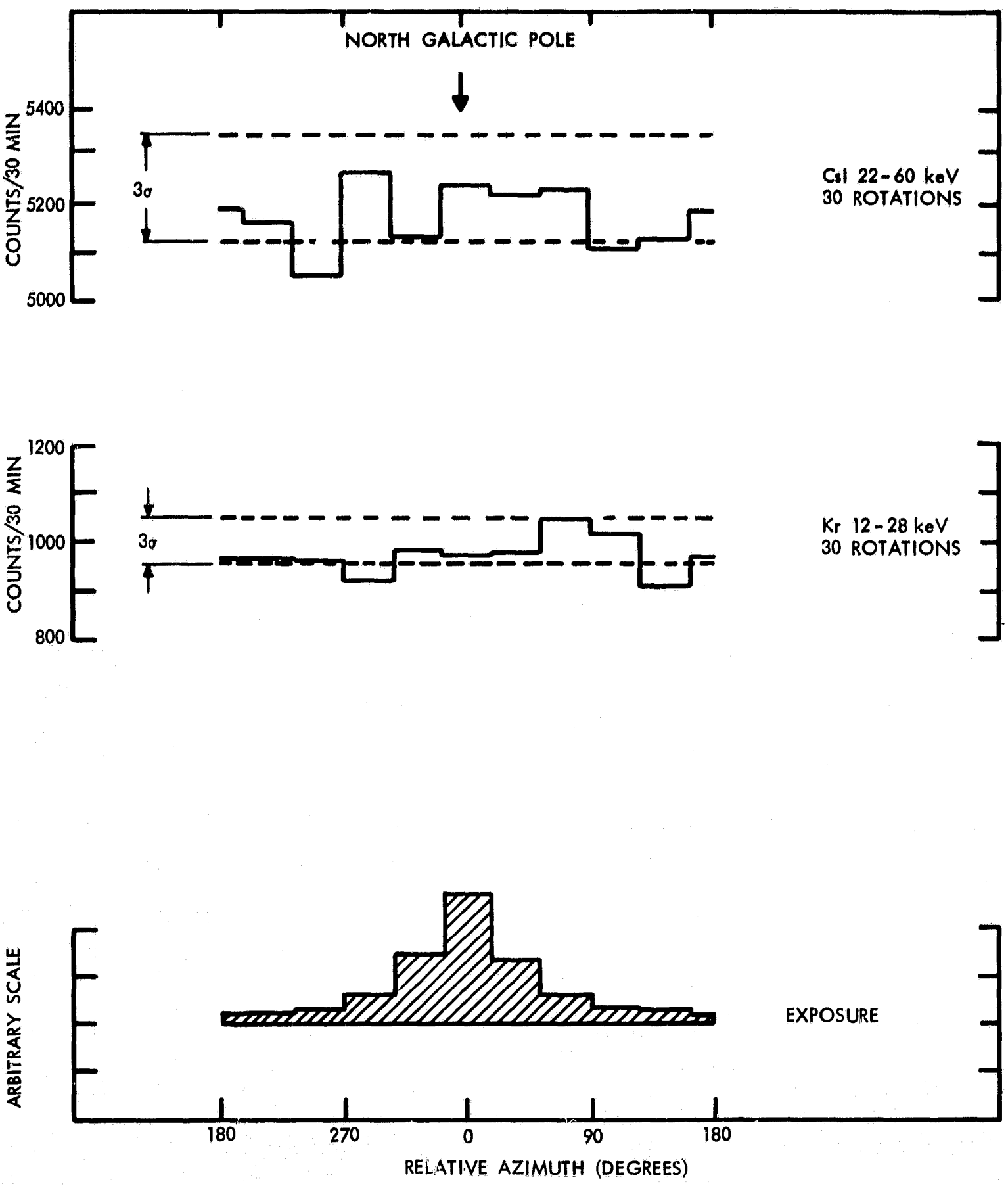

Figure 29— Superposition of epochs phased in azimuth angle relative to the direction of the north galactic pole (experiment 6). Top curve: CsI crystal, 22 - 60 keV. Middle curve: proportional counter, 12 - 28 keV. Bottom curve: exposure to a point source at the position of the north galactic pole

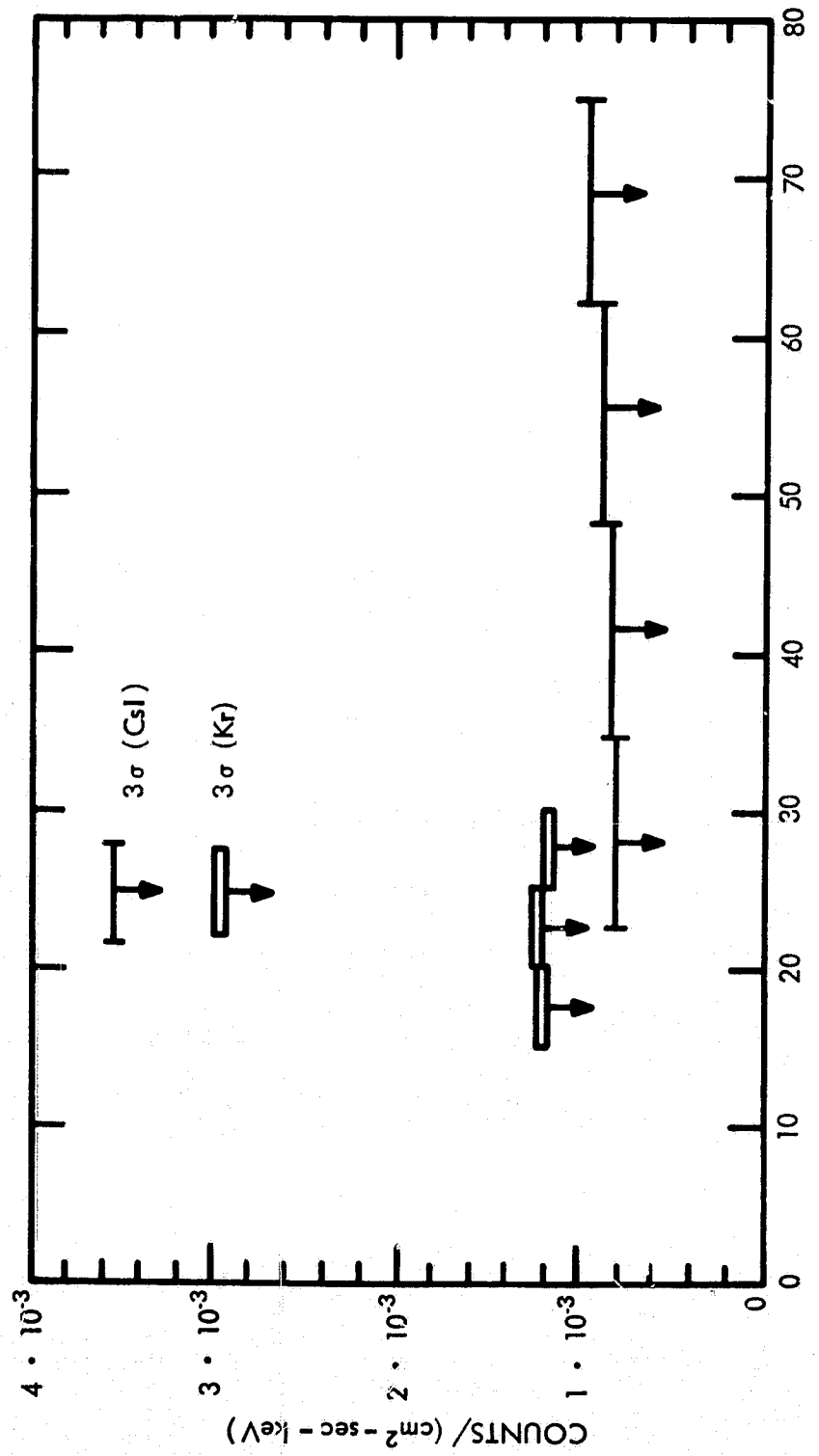

Figure 30— 3σ-limiting signals to the photon flux from the vicinity of the north galactic pole (experiment 6). Single bars: CsI crystal. Double bars: proportional counter

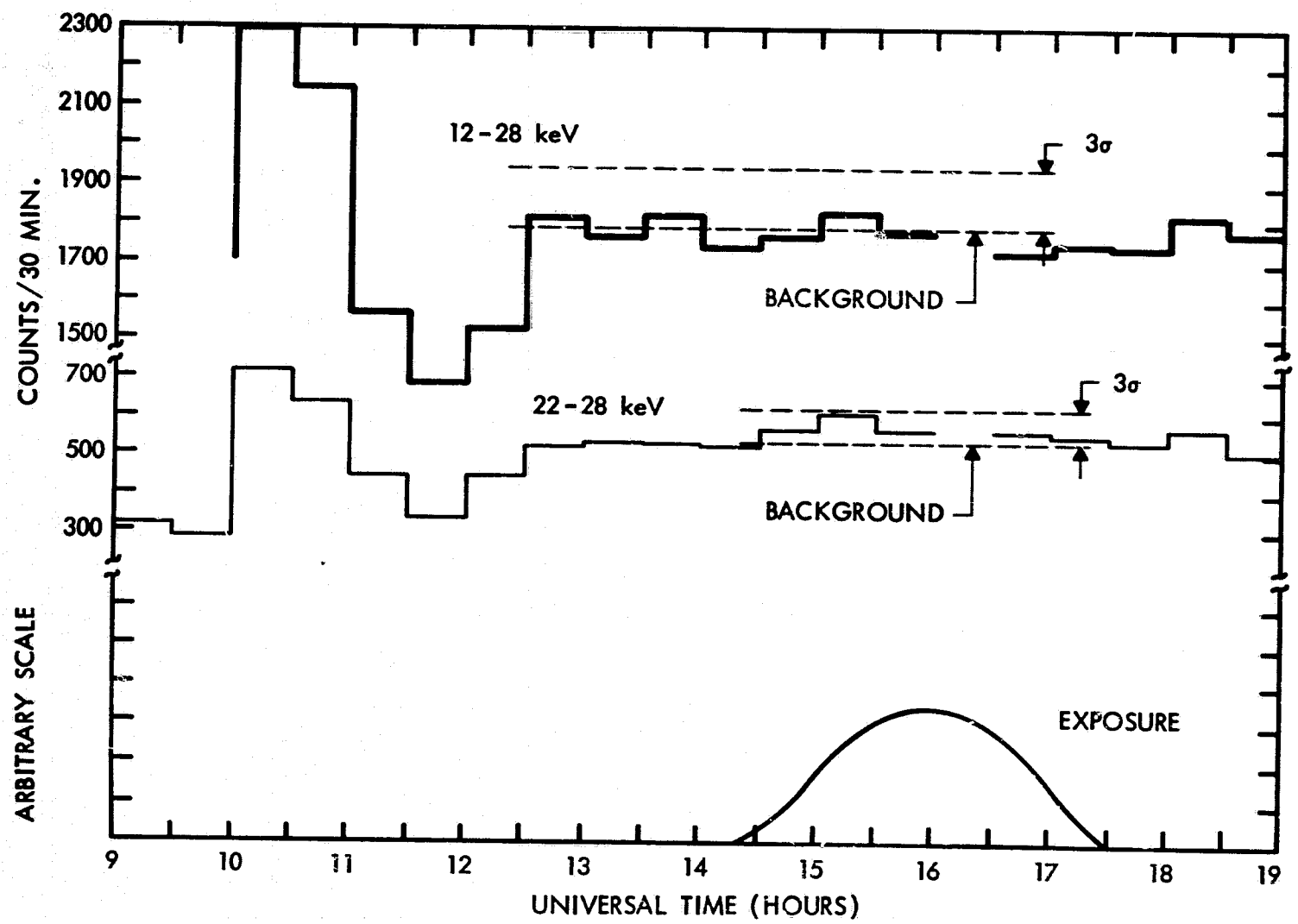

Figure 31— Dead-time corrected counting rate profile of the proportional counter in experiment 7. Top curve: 12 - 28 keV. Middle curve: 22 - 28 keV. Bottom curve: exposure to a point source at the direction of the north galactic pole. 3σ-limiting signals are indicated by broken lines

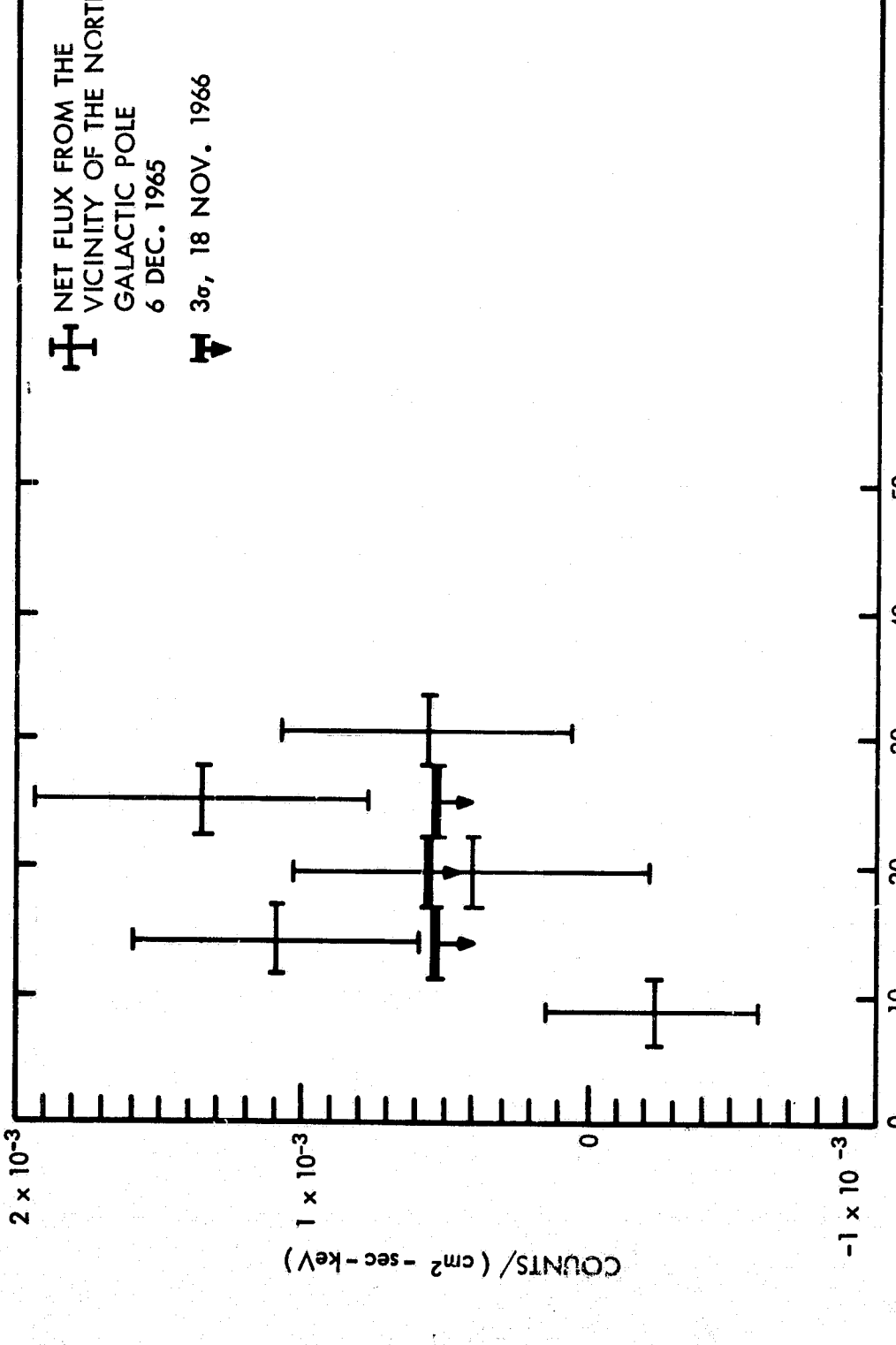

Figure 32—3σ-limiting signals to the photon flux from the vicinity of the north galactic pole (experiment 7). The observed net counts of experiment 1 are also given

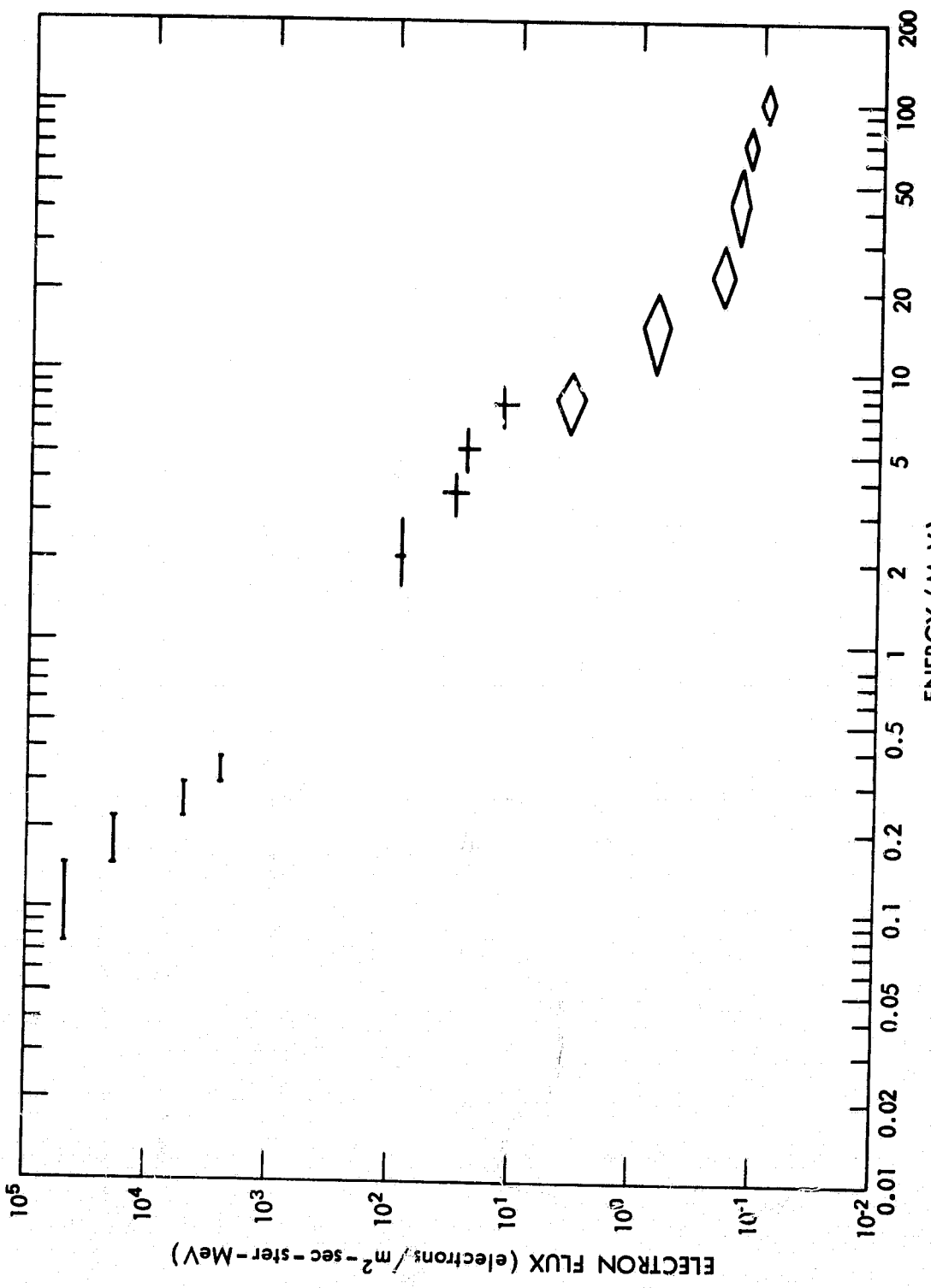

Figure 33— Measurements of the low-energy electron spectrum near the top of the atmosphere. Bars: Cline and Brunstein (1966), 4 g/cm^2, International Falls, Minn. Crosses: Brunstein (1967), 5.5 g/cm^2, Sioux Falls, S. D, Diamonds: Beedle and Webber (1968), extrapolated to 1 g/cm^2, Ft.. Churchill, Manitoba

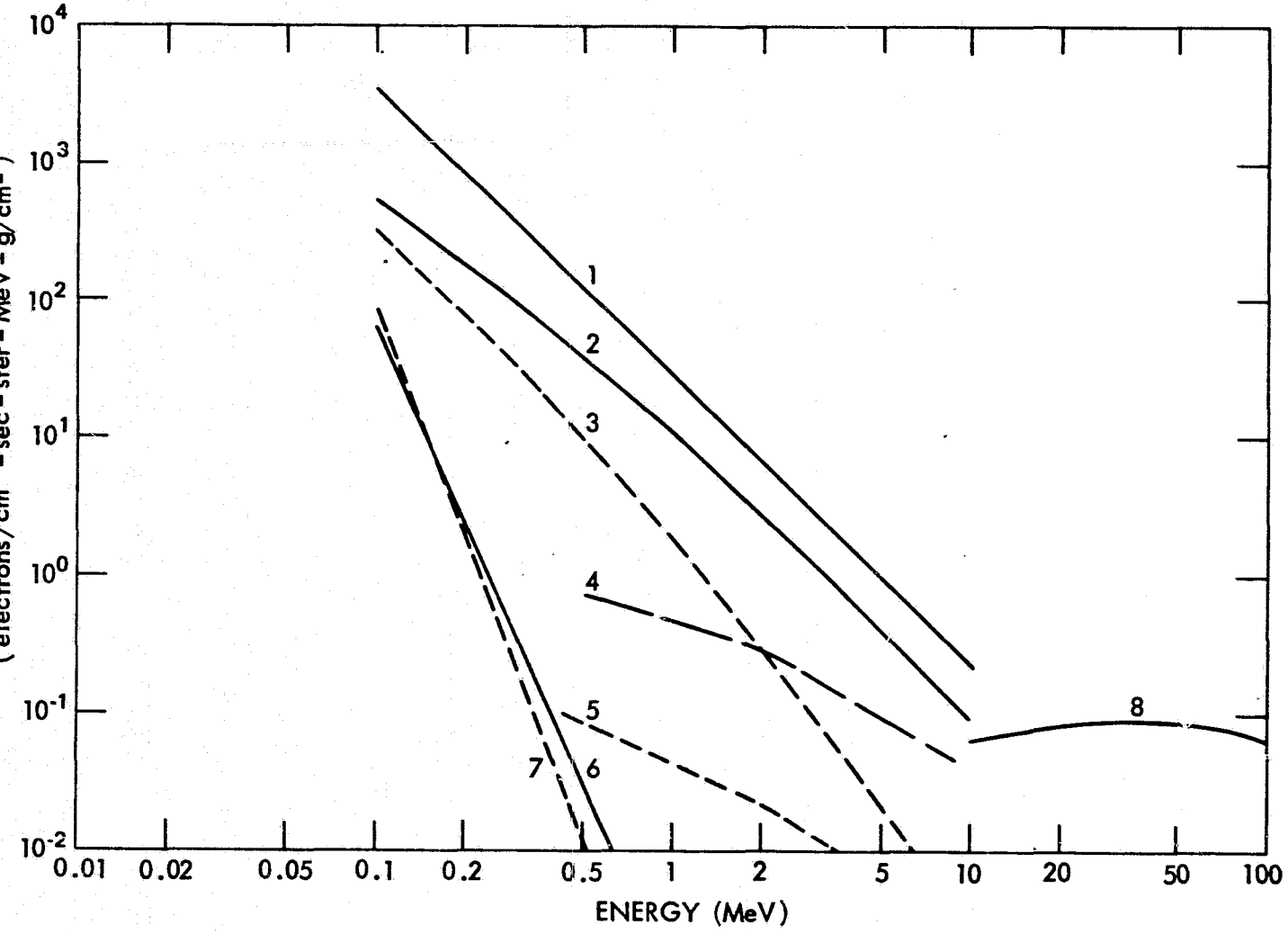

Figure 34— Production of electrons per g/cm^2 at E_c = 3600 MeV.

1. Knock-on electrons at 1 g/cm^2
2. Compton electrons due to the atmospheric photon flux
3. Compton electrons due to the primary photon flux
4. Pair electrons due to the atmospheric photon flux
5. Pair electrons due to the primary photon flux
6. Photoelectrons due to the atmospheric photon flux
7. Photoelectrons due to the primary photon flux
8. Electrons from pion decay (Verma, 1966)

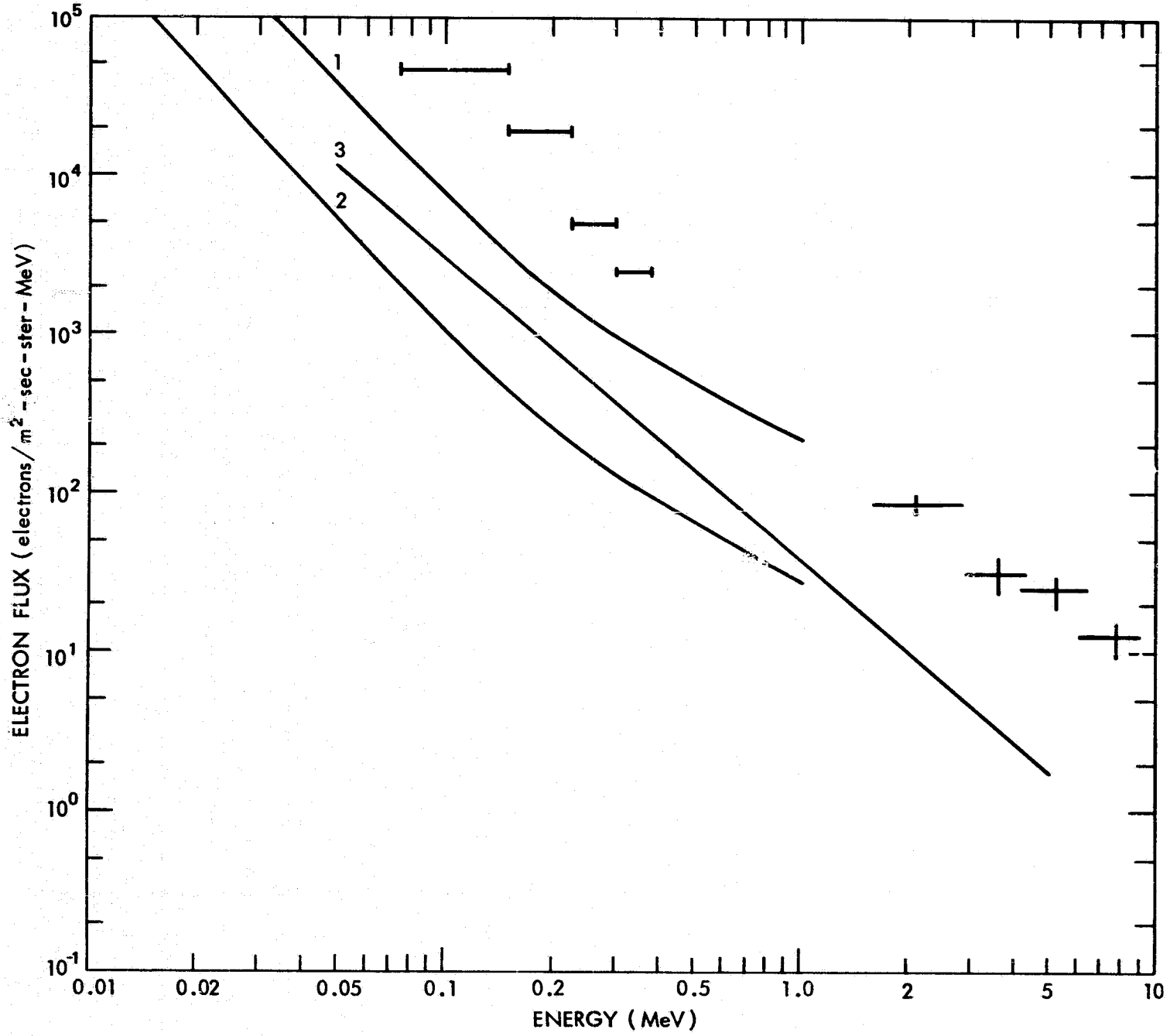

Figure 35— Electron equilibrium spectrum near the top of the atmosphere. Bars: Cline and Brunstein (1966, $d = 4$ g/cm^2, $E_c = 400$ MeV). Crosses: Brunstein (1967, $d = 5.5$ g/cm^2, $E_c = 400$ MeV). Curve 1: calculation for $d = 4$ g/cm^2, $E_c = 20$ MeV. Curve 2: calculation for $d = 4$ g/cm^2, $E_c = 3600$ MeV. Curve 3: fit to the measurement of Beedle (1966) at $d = 4$ g/cm^2, $E_c = 20$ MeV

ATMOSPHERIC X-RAY SPECTRUM

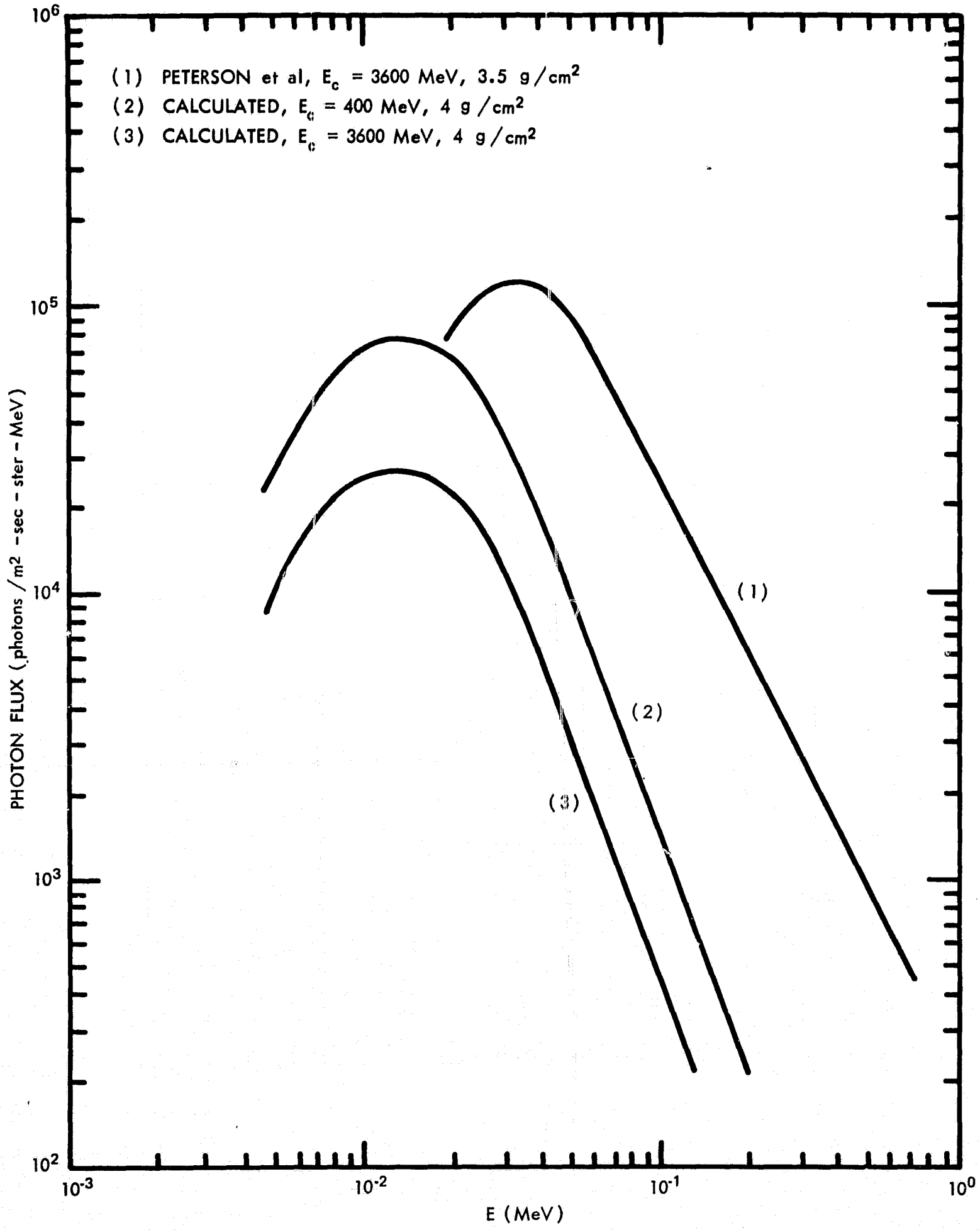

Figure 36— The atmospheric X-ray spectrum. Curve 1: Peterson et al. (1967a), E_c = 3600 MeV, d = 3.5 g/cm^2. Curve 2: calculated for E_c = 400 MeV, d = 4 g/cm^2. Curve 3: calculated for E_c = 3600 MeV, d = 4 g/cm^2

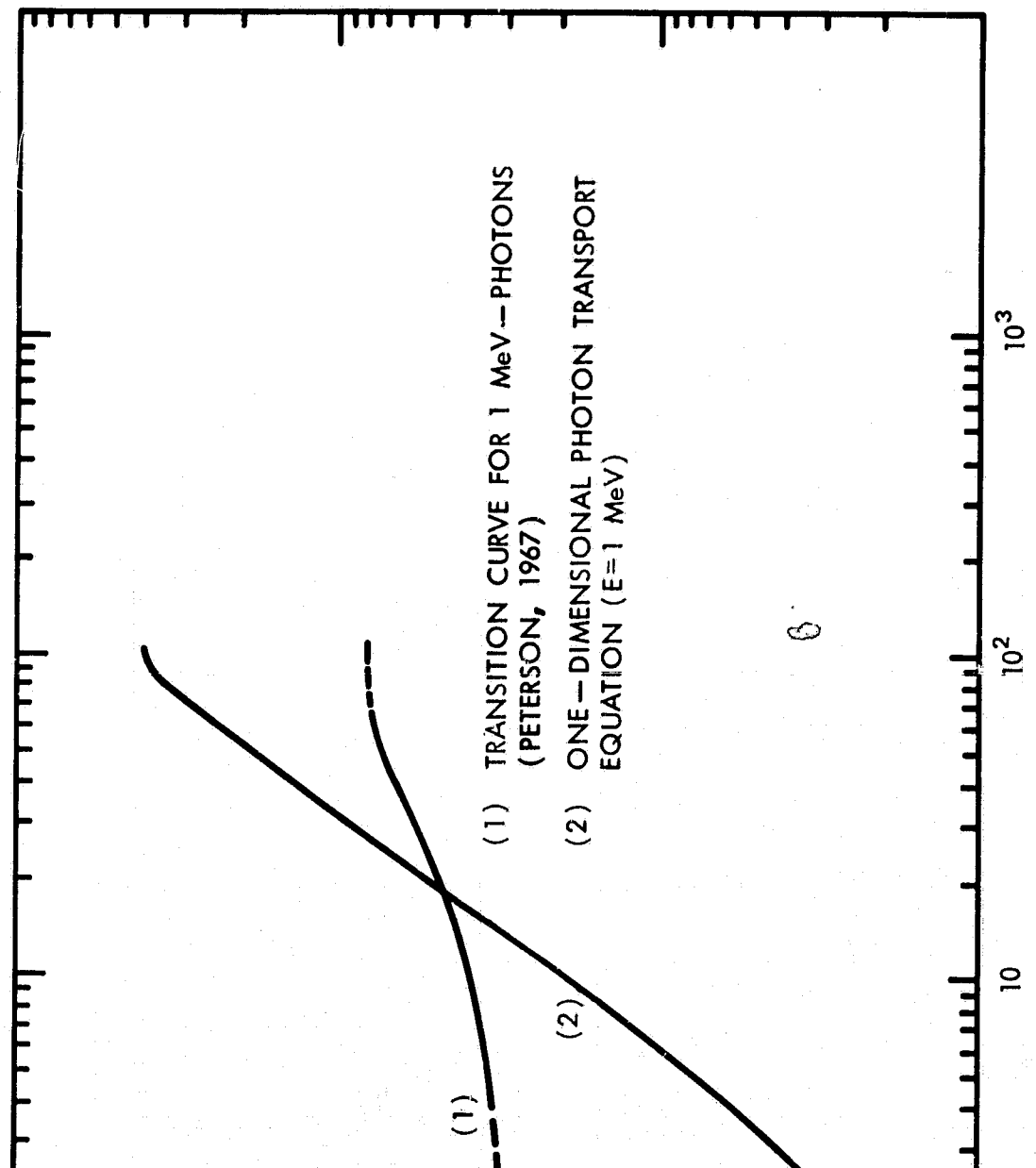

Figure 37— The atmospheric transition profile for 1 MeV-photons.
Curve 1: Peterson (1967b). Curve 2: solution of a one-dimensional photon transport equation (E = 1 MeV)